UQÀM | Université du Québec à Montréal

IMPACTS À DISTANCE DU SAHARA VERT DU MILIEU DE L'HOLOCÈNE SUR LE CLIMAT MONDIAL

THÈSE

PRÉSENTÉE

COMME EXIGENCE PARTIELLE

DU DOCTORAT EN SCIENCES DE LA TERRE ET DE L'ATMOSPHÈRE

PAR

SHIVANGI TIWARI

JANVIER 2025

REMOTE IMPACTS OF THE MID-HOLOCENE GREEN SAHARA ON GLOBAL CLIMATE

THESIS

PRESENTED

IN PARTIAL REQUIREMENT FOR

DOCTORATE IN EARTH AND ATMOSPHERIC SCIENCES

BY

SHIVANGI TIWARI

JANUARY 2025

ACKNOWLEDGEMENTS

Every thesis is a journey. I have several people to thank who helped me complete mine.

I'm grateful to Francesco, Anne and Hugo for their boundless trust, patience and efforts for me. I have miles to go before I sleep, but I am also happy with the progress I have made, and it's thanks to you.

I also received invaluable help from Allegra N. LeGrande, Michael Griffiths and Ilana Wainer, who went out of their way to mentor me. I hope that one day I can help someone else in the same way.

This was a 'pandemic PhD', and it was a rough start. Three people come to mind whose kindness meant a lot: Katja Winger, Michel Valin and Michel Lamothe. Thank you.

Few people get second chances as generous as mine. I am indebted to my parents who gave me the support necessary to pursue my dream. And finally, my friends and family, both in India and Canada, who kept me going. Thank you.

DÉDICACE

I dedicate this thesis to my parents, Rajni and Sanjay Tiwari, whom I met when I was born; and also Vandana and Vivek Prasad, whom I met when the stars aligned.

PREFACE

The Sahara is the largest tropical desert in the world. It's nearly the size of Canada and nearly three times the size of India. It is therefore not a small matter if it tends to transform from a desert state to a vegetated state and back. What are the reasons behind such large-scale changes? What are their implications? How well do we understand this phenomenon of regular climatic transitions over northern Africa? Known as the Green Sahara, this instance of non-linear climate change has been of interest to the paleoclimate community for several decades. It has been reconstructed extensively using various paleoclimatic archives and proxies, and has been the subject of numerous modelling studies. While its impacts on the regional climate dynamics are relatively well understood, recent studies have opened a new direction of research: the teleconnections of the Green Sahara with various other regions around the world. The goal of this work was to extend our understanding of these teleconnections.

This work involved the use of five global climate models, the results from which were further evaluated by proxy-model comparisons. While this work represents a significant improvement over previous studies due to the focus on multi-model comparisons, it is necessarily limited by the limitations of these climate models. To make matters more interesting and challenging, the Green Sahara involved several non-linear climate feedbacks. Despite all the efforts made, there is still much to be perfected to integrate them in climate studies. Notwithstanding these limitations, I hope this work answers some relevant questions and raises some others.

TABLE DES MATIÈRES

LISTE DES FIGURES

LISTE DES ABRÉVIATIONS, DES SIGLES ET DES ACRONYMES

AEJ   African Easterly Jet

AMOC   Atlantic Meridional Overturning Circulation

AWJ   African Westerly Jet

BP   Before Present

ENSO   El Niño Southern Oscillation

GHG   Green House Gases

GMST   Global Mean Surface Temperature

GSP   Green Sahara Period

ITCZ   Inter Tropical Convergence Zone

MH   Mid-Holocene

NH   Northern Hemisphere

PI   Pre-Industrial

PMIP   Paleoclimate Modelling Intercomparison Project

RMSE   Root Mean Square Error

SAMS   South American Monsoon System

SIC   Sea Ice Concentration

SPCZ   South Pacific Convergence Zone

SSS   Sea Surface Salinity

SST   Sea Surface Temperature

TEJ   Tropical Easterly Jet

WAM   West African Monsoon

RÉSUMÉ

Le Sahara est le plus grand désert tropical du monde. S'étendant d'environ 20 à 33 °N et de 15 °O à 35 °E, la région saharienne reçoit moins de 100 mm de précipitations par an et se caractérise par une végétation de steppe et de désert très clairsemée. Il s'agit actuellement de la plus grande source de poussière minérale sur Terre, les principales sources se trouvant dans la dépression de Bodélé au Niger et au Tchad et une autre source en Mauritanie et au Mali. Les grandes quantités de poussières terrigènes (de l'ordre de 250 Tg par an) ont un impact sur l'insolation et les propriétés des nuages en Afrique du Nord ainsi que sur les températures de surface de la mer et la productivité dans la région de l'Atlantique tropical nord. La dépression thermique saharienne (une dépression thermique de bas niveau en pression de surface, régie par l'albédo du désert) est un facteur important de la circulation atmosphérique et des précipitations de mousson dans la région.

Les reconstructions paléoclimatiques ont montré que la région actuelle du désert saharien était recouverte de végétation au début et au milieu de l'Holocène (~ 11000 à 5500 ans avant le présent ou BP). Un changement dans les paramètres orbitaux a conduit à une augmentation de l'insolation estivale dans l'hémisphère nord avec un maximum d'insolation maximale se produisant entre 10000 et 7000 ans avant notre ère, conduisant à une intensification de la mousson ouest-africaine qui amène des précipitations en Afrique du Nord. De nos jours, l'extension vers le nord de la mousson ouest-africaine s'étend jusqu'au Sahel (la région au sud du Sahara qui reçoit 100 à 400 mm de précipitations par an, environ entre 12-20 °N). Au début et au milieu de l'Holocène, les reconstructions paléoclimatiques indiquent un déplacement des isohyètes vers le nord, conduisant au développement d'une végétation herbacée et arbustive à travers le Sahara et à une expansion vers le nord de toute la végétation d'Afrique du Nord. C'est ce qu'on appelle le Sahara vert, avec la période correspondante appelée période du Sahara vert ou période humide africaine. Le Sahara vert s'est accompagné d'une réduction des flux de poussières terrigènes et d'une expansion des lacs, des zones humides et des rivières à travers l'Afrique du Nord.

Bien que les changements dus au Sahara vert dans le climat régional de l'Afrique du Nord aient été étudiés de manière approfondie et soient relativement bien compris, les impacts lointains sur d'autres régions du monde méritent une étude plus approfondie. Des études récentes ont indiqué la possibilité de téléconnexions entre le Sahara vert et différentes régions du monde telles que les océans tropicaux Atlantique et Pacifique, la région arctique et les zones de moussons asiatiques. Dans ce contexte, l'objectif

de la présente thèse est d'approfondir notre compréhension des impacts à distance des changements de végétation en Afrique du Nord sur le climat de trois régions clés du monde : l'Amérique du Sud, le Pacifique équatorial et l'Arctique. À cette fin, quatre modèles climatiques globaux entièrement couplés et un modèle climatique global uniquement atmosphérique ont été utilisés pour simuler le milieu de l'Holocène (6000 ans BP) avec et sans intégration des changements du Sahara vert. L'identification et l'évaluation de l'impact du Sahara vert sur le climat des trois régions, qui sont d'ampleur similaires et vont dans le même sens que les impacts des changements orbitaux. Le Sahara vert a entraîné une réduction importante et tout au long de l'année des précipitations sur l'Amérique du Sud, une réduction de la variabilité de l'oscillation australe d'El Niño et contribuer à générer un mode de type La Niña dans le Pacifique équatorial, et un réchauffement dans l'Atlantique Nord et dans certaines régions de l'Arctique (en particulier la mer de Barents).

Les résultats présentés ici sont vérifiés par une comparaison des résultats du modèle avec des reconstructions paléoclimatiques basées sur des indicateurs climatiques indirects. Les comparaisons modèle-proxy effectuées dans ce travail suggèrent une plus grande cohérence des résultats du modèle avec les données proxy lors de l'inclusion des conditions du Sahara vert dans les simulations du modèle. Les principales implications de ce travail sont les suivantes :

1) L'inclusion du Sahara vert conduit à une amplification des changements climatiques induits par l'orbite (tels que les changements dans les précipitations, les températures et la variabilité de la température de la surface de la mer) dans diverses régions du monde.

2) Il est crucial d'intégrer les conditions du Sahara vert (en particulier les changements dans la couverture végétale) dans les études de modélisation de l'Holocène précoce et moyen. Une représentation inadéquate du Sahara vert peut conduire à une sous-estimation des anomalies climatiques au cours de l'Holocène précoce et moyen par rapport à la période actuelle ou préindustrielle.

Les biais du modèle jouent un rôle essentiel dans la limitation de la capacité des modèles climatiques à représenter les téléconnexions entre l'Afrique du Nord et d'autres régions du monde au cours de l'Holocène précoce et moyen.

Mots clés : Modélisation paléoclimatique, Holocène moyen, Sahara vert, rétroactions climatiques, Amérique du Sud, El Niño Oscillation australe, régions de l'Atlantique Nord et de l'Arctique

ABSTRACT

The Sahara is the largest tropical desert in the world. Extending from about 20-33 °N and 15 °W – 35 °E, the Saharan region receives less than 100 mm of precipitation per year, and is characterized by very sparse steppe and desert vegetation. Presently, it is the largest source of mineral dust on the Earth, with the main sources found to be in the Bodélé depression of Niger and Chad and another source in Mauritania and Mali. The large amounts of terrigenous dust (in the order of 250 Tg per year) impacts insolation and cloud properties over northern Africa as well as sea surface temperatures and productivity in the North Tropical Atlantic region. The Saharan Heat Low (a low-level thermal low in surface pressure, governed by the desert albedo) is an important driver of atmospheric circulation and monsoon precipitation in the region.

Paleoclimatic reconstructions have shown that the present-day Saharan desert region was vegetated in the early and middle Holocene (~11,000 - 5,500 years Before Present or BP). A change in the orbital parameters led to an increase in summer insolation in the Northern Hemisphere with a maximum with maximum insolation occurring between 10,000 – 7,000 years BP, leading to an intensification of the West African Monsoon which brings precipitation to northern Africa. In the present day, the northern extent of the West African Monsoon is upto the Sahel (the region southwards of the Sahara which receives 100-400 mm of rainfall annually, approximately between 12–20 °N). During the early and middle Holocene, paleoclimate reconstructions indicate a northward movement of the isohyets, leading to the development of grass and shrub vegetation across the Sahara and a northward expansion of all vegetation in northern Africa. This is referred to as the Green Sahara, with the corresponding time period referred to as the Green Sahara Period or the African Humid Period. The Green Sahara was accompanied by a reduction in terrigenous dust fluxes and an expansion of lakes, wetlands and rivers across northern Africa.

While the changes due to the Green Sahara in regional climate over northern Africa have been extensively studied and are relatively well understood, the remote impacts on other regions of the world warrant further study. Recent studies have indicated the possibility of teleconnections between the Green Sahara and different regions of the world such as the tropical Atlantic and Pacific oceans, the Arctic region and the domains of Asian monsoons. In that context, the aim of the present thesis is to deepen our understanding of the far-afield impacts of the northern African vegetation changes on the climate of three key regions of the world : South America, the equatorial Pacific and the Arctic. To this end, five fully coupled global climate models and one atmosphere-only global climate model have been used to simulate

the mid-Holocene (6,000 years BP) with and without incorporating Green Saharan changes. Isolating the impact of the Green Sahara has shown considerable impacts in all three regions, which are similar in direction and comparable in magnitude to the impacts of the orbital changes. The Green Sahara led to extensive and year-round reduction in precipitation over South America, a reduction in the variability of the El Niño Southern Oscillation and a nudge towards a La Niña-like mean state in the equatorial Pacific, and a warming in the North Atlantic and regions of the Arctic (particularly the Barents Sea).

The findings presented here are verified by a comparison of model results with paleoclimatic reconstructions based on climate proxies (indirect indicators). The model-proxy comparisons carried out in this work suggest greater coherence of model results with proxy data upon the inclusion of Green Saharan conditions in model simulations. Major implications of this work are:

1) The inclusion of the Green Sahara leads to an amplification of orbitally-driven climatic changes (such as changes to precipitation, temperatures and sea surface temperature variability) over various regions of the world.

2) It is crucial to incorporate Green Saharan conditions (especially changes to vegetation cover) in modelling studies of the Early and Middle Holocene. An inadequate representation of the Green Sahara may lead to an under-estimation of climate anomalies during the Early and Middle Holocene relative to the present-day or the pre-Industrial time period.

3) Model biases play a critical role in constraining the ability of climate models to represent teleconnections between northern Africa and other regions of the world during the Early and Middle Holocene.

Keywords : Paleoclimate modelling, mid-Holocene, Green Sahara, climate feedbacks, South America, El Niño Southern Oscillation, North Atlantic and Arctic regions

INTRODUCTION

1.1   The Green Sahara Period: an overview

The Sahara is the largest tropical desert in the present-day climate system, receiving less than 100 mm of precipitation each year. The West African Monsoon (WAM) brings precipitation to northern tropical Africa largely during boreal summer, delimiting broadly zonal hydroclimatic regions bound by east-west traversing isohyets (Figure 2-1). The different hydroclimatic zones lead to a broadly zonal distribution of vegetation. From south to north, the increasing precipitation leads to bands of equatorial Guinean-Congolian vegetation, Sudanian vegetation, Sahelian vegetation and lastly, the Saharan region which in the present day is almost devoid of vegetation (White, 1986). Paleoclimatic reconstructions with pollen proxies indicate that between ~11 thousand years before present (ka BP) and ~5.5 ka BP, the vegetational belts of northern Africa expanded northwards due to an intensification and expansion of the WAM (Hély et al., 2014). The increase in precipitation enabled the development of savannah vegetation over the Sahara, earning it the moniker "Green Sahara". The corresponding interval is referred to as the Green Sahara Period (GSP) or the African Humid Period. In addition to pollen, evidence for the GSP comes from dust, speleothem, organic biomarker and paleohydrological archives (discussed further in the next chapter). On the regional scale, the termination of the GSP occurred in a time-transgressive manner i.e. it occurred earlier at the more northerly sites and later at the southerly sites (Shanahan et al., 2015). However, on the local scale, the climate transitions occurred within centuries, in an abrupt manner that did not scale linearly with insolation changes (deMenocal et al., 2000). Hence, the GSP is a key interval for the study of non-linear feedbacks in the climate system. The GSP also evokes interest from the perspective of understanding WAM dynamics to improve weather forecasting in the drought-prone Sahel, and from paleoanthropological and archaeological viewpoints (Drake et al., 2013; Tierney, deMenocal, et al., 2017).

Numerous GSPs have occurred over the Neogene, forced by insolation changes. Paleoclimatic records have indicated at least 230 GSPs in the last 8 million years (Larrasoaña et al., 2013). A geochemical record off the northwestern coast of Africa further elicited three distinct stages of GSP conditions over the last 11 million years (Crocker et al., 2022a). GSPs are primarily forced by precession and its effect of enhancing Northern Hemisphere seasonality (Kutzbach et al., 2020), but appear to also be modulated by eccentricity in terms of their timing (Menviel et al., 2021) and amplitude (Armstrong et al., 2023). Some of the past GSPs (such as the Eemian GSP: ~ 122 − 128 ka BP) were characterized by greater strengthening of the WAM relative to the Holocene GSP. However, the focus of this thesis is on the Holocene GSP owing to the

1

substantially greater availability of proxy reconstructions for this period that allow for more extensive comparisons between proxy reconstructions and model results.

1.2   Present-day climate of the region

The regional atmospheric circulation and hydroclimate over northern tropical Africa is characterized by the dry northeasterly "Harmattan" winds during boreal winter and the West African Monsoon (WAM) during boreal summer (Figure 2-2). The WAM brings the majority of the annual precipitation to its domain between June and September. The progression of the WAM, which is governed by the seasonal movement of the Inter Tropical Convergence Zone (ITCZ), is best understood in terms of four phases: oceanic phase, coastal phase, transitional phase and Sahelian phase (Thorncroft et al., 2011b). During these phases, the rainfall peak shifts from around 1 °N during the oceanic phase (November-April) to around 10 °N during the Sahelian phase (July-September). The seasonal reversal of winds over the Sahel leads to a low-level convergence between southwesterly winds that carry moisture from the equatorial Atlantic Ocean and dry northerly winds (the Harmattan), bringing precipitation to the region during boreal summer (Sultan & Janicot, 2003). The strength of the WAM is modulated by the thermodynamic contrast between the African landmass and the tropical Atlantic Ocean, in particular the Atlantic Cold Tongue (Okumura & Xie, 2004).

The vegetation cover over the African landmass plays a key role in modulating the climate by influencing surface albedo and terrigenous dust emissions (Charney et al., 1975; Otterman, 1974). Dust concentrations in the atmosphere further affect incoming shortwave radiation through aerosol direct and indirect effects. Both these factors combine to modulate the surface radiative balance, surface temperatures and the Saharan Heat Low which further drives convection during the monsoon season (Lavaysse et al., 2009). Another (relatively minor) effect of land surface changes includes greater water vapour flux and latent heat in the atmosphere due to an enhanced vegetation cover.

Precipitation over northern Africa is further modulated by three jets:

i.   The African Westerly Jet (AWJ): A low-level jet which shows maximum wind speeds between 8°-11° N at around 850 hPa and modulates the north-south displacement of the WAM (Nicholson,

2009). A strengthened AWJ is associated with higher precipitation over the Sahel (Pu & Cook, 2012).

ii. The African Easterly Jet (AEJ): A mid-tropospheric jet which shows maximum wind speeds around $20°$ N and 600 hPa. A weakened AEJ is associated with a stronger WAM (Lafore et al., 2011; Nicholson, 2009; Sultan & Janicot, 2003).

iii. The Tropical Easterly Jet (TEJ): An upper tropospheric jet which shows maximum wind speeds around $10°$ N and 150 hPa. An intensified TEJ is associated with a stronger WAM (Nicholson, 2009, 2013; Sultan & Janicot, 2003).

The WAM also shows considerable intra-seasonal variability, such as arising from the Madden-Julian Oscillation or African Easterly Waves (D. E. Poan et al., 2015; E. D. Poan et al., 2016). However, the GSP was an event of multi-millenial duration. Hence, the focus of this thesis is on inter-annual to millennial scale climate changes.

1.3   Drivers of the Green Sahara

The increase in precipitation over northern Africa during the GSP was, in the first order, a result of changes to the orbital forcings. Specifically, precessional changes led to shifting of the perihelion from boreal winter in the present day to boreal fall during the MH (B. Otto-Bliesner et al., 2017). This led to enhanced seasonality and greater insolation during boreal summer in the Northern Hemisphere. Other orbital changes include obliquity being slightly higher during the MH relative to the pre-Industrial (PI) time period. This led to higher annual mean insolation at high latitudes, and lower annual mean insolation at the tropics, eventually resulting in a negligible insolation forcing on the global scale. Eccentricity during the MH was similar to that during the PI. GHG concentrations were lower during the MH relative to the PI, with CO_2, CH_4 and N_2O at about 264.4 ppm, 597 ppb and 262 ppb, respectively. However, climate model simulations which incorporate changes to orbital forcings and GHG concentrations do not adequately simulate the changes during the GSP, highlighting the important but under-represented role of climate feedbacks (C. M. Brierley et al., 2020a).

There are at least five climate feedbacks that played a role during the GSP:

1. Vegetation feedback: The insolation-driven increase in precipitation led to the expansion of shrub and savanna vegetation characteristic of the present-day Sahelian region into the present-day Saharan region, reducing the surface albedo from 0.3-0.4 (characteristic of desert surfaces) to 0.1-0.2 (characteristic of vegetated surfaces). The lower albedo led to higher absorption of shortwave radiation, higher land temperatures, greater land-sea contrast and hence, a strengthening of the WAM (Charney et al., 1975). Further, the presence of vegetation leads to greater evapo-transpiration, greater land-atmosphere water vapor flux and greater latent heating of the atmosphere (Pausata et al., 2020).

2. Dust feedback: Direct radiative effects of dust reduction include a reduction in the albedo, increasing shortwave radiation that reaches the surface, thus warming the land surface and enhancing the monsoonal circulation (Pausata et al., 2016). The positive feedback on precipitation is dampened by the indirect radiative effects of dust reduction, but the net result remains positive over the Saharan region (Thompson et al., 2019).

3. Soil feedback: A change in the soil texture from sandy soils to loamy soils led to darker soils with greater water retention capacity which further supported greater evapotranspiration. The presence of vegetation led to greater organic matter content in the soil, further darkening the soil albedo and hence, reinforcing the precipitation increase (Chandan & Peltier, 2020; Levis et al., 2004).

4. Lake and wetlands feedback: The presence of large waterbodies such as Megalakes Chad, Nubian and Fezzan as well as several wetlands provided more local moisture sources, enhanced moisture recycling and led to lower surface temperatures over water relative to surrounding land in northern Africa (Carrington et al., 2001; Chandan & Peltier, 2020).

5. Ocean feedback: A warming of North Atlantic SSTs north of 15° N and a cooling south of it led to the development of an oceanic dipole in the Northern Atlantic, leading to increased moisture advection from the ocean and a lengthening of the monsoon season (P Braconnot et al., 1999; Zhao et al., 2005).

An adequate representation of these climate feedbacks, particularly the vegetation feedback, is necessary to accurately simulate the northern African climate and obtain precipitation estimates commensurate with the Green Saharan vegetation changes. In theory, the use of interactive vegetation would ensure the simulation of the vegetation feedback. However, owing to the computational expense and difficulty of using dynamic vegetation (Pascale Braconnot et al., 2019; Dallmeyer et al., 2023), as well as the limitations of this approach in fully reconciling proxy-model precipitation estimates, several studies have instead

relied on prescribing changes to the vegetation cover over northern Africa to obtain a first-order representation of the vegetation feedback.

1.4   Implications of the Green Sahara for global climate

The vegetation and land surface conditions over northern Africa played a key role in modulating the regional climate. Additionally, these large-scale changes impacted the surface albedo, raising surface temperatures considerably over a large landmass with an impact on global mean surface temperatures. The enhanced vegetation cover led to a reduction in terrestrial dust fluxes, which impacted sea surface temperatures and productivity over the tropical Atlantic Ocean. Finally, by shifting centers of low-level convergence and divergence, the Green Sahara led to shifts in the global Walker Circulation, impacting conditions over the tropical Pacific as well as the Indian Ocean. Thus, the Green Sahara was not simply a regional phenomenon, but had far-afield impacts on global climate (discussed further in the next Chapter).
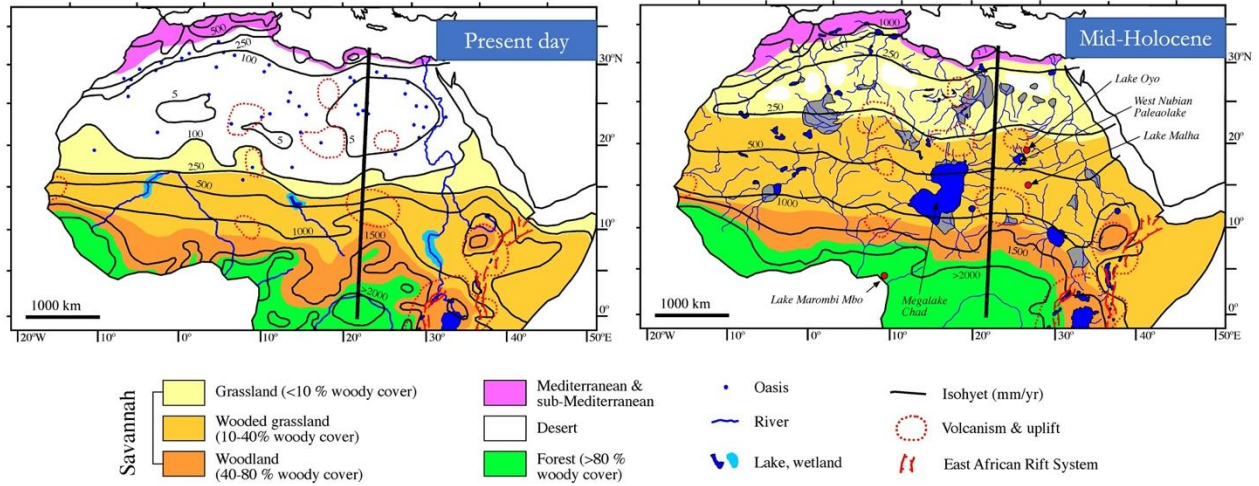
Figure 2-1 Mean annual precipitation (isohyets) and vegetation distribution over northern Africa. Adapted from Larrasoana et al. (2013).
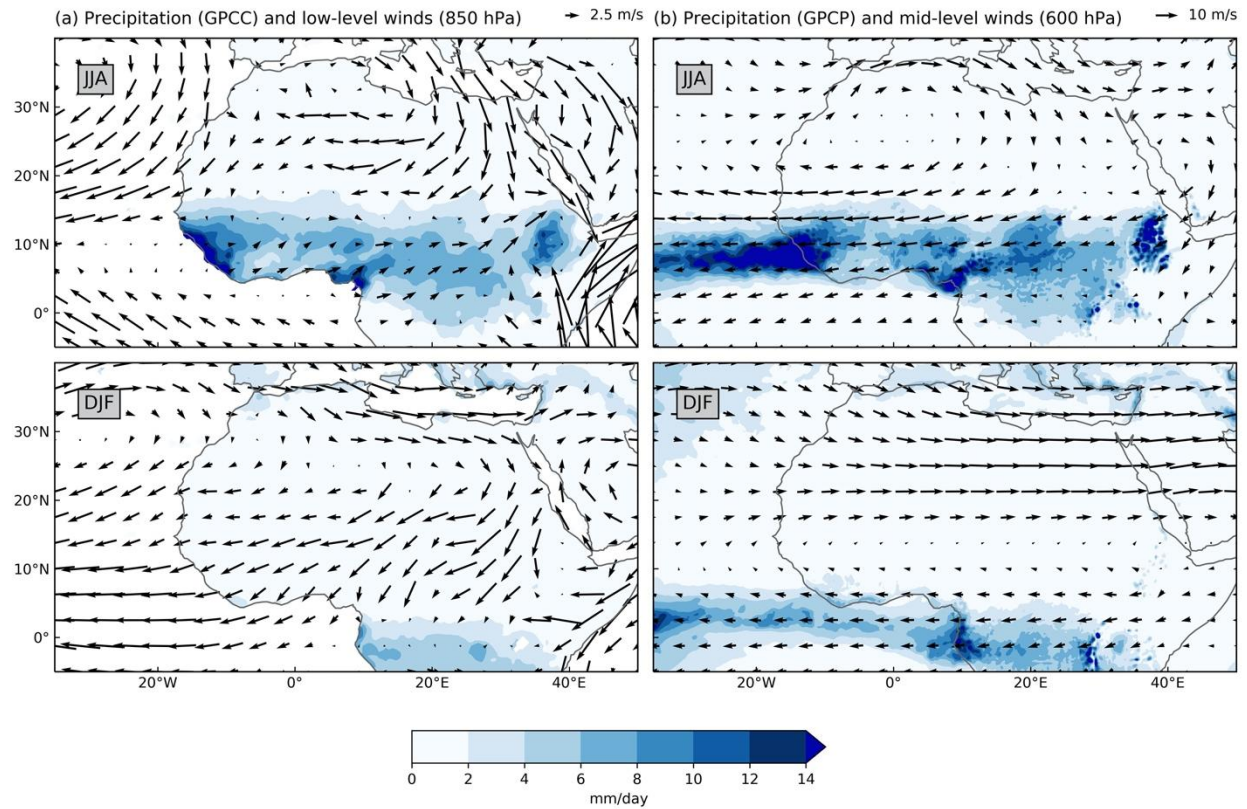
Figure 2-2 Seasonal precipitation and wind circulation. (a) Colors show precipitation from the Global Precipitation Climatology Centre dataset version 7 with land-only coverage (Schamm et al., 2014). Overlain vectors show low-level (850 hPa) winds from the ERA5 re analysis dataset (Hersbach et al., 2020). (b) Colors show precipitation and overlain vectors show mid-level (600 hPa) winds from the ERA5 reanalysis dataset (Hersbach et al., 2020). All data is for the period 1940-1980.

CHAPITRE 2

STATE OF THE ART AND OBJECTIVES

2.1   Proxy reconstructions for the Green Sahara

There is robust evidence for the strengthening of the WAM during the Holocene GSP, indicated by reconstructions based on various archives and proxies (Figure 2-1).

Pollen records

Several pollen records from both terrestrial and marine sites provide evidence for the Green Sahara. Early work on marine cores from equatorial West Africa and the Atlantic showed an expansion of the tropical rainforest (Dupont et al., 2000) and an enhancement in the Niger River discharge in response to the WAM intensification during the early and middle Holocene (Lézine et al., 2005). A sediment sequence from Lake Yoa, Chad, provided a record of the desertification with prominent changes to lake productivity and terrestrial ecosystem indicators occurring around 5.6 ka, 4.3 ka and 2.7 ka, suggesting changes in regional atmospheric circulation (Kröpelin et al., 2008). A compilation of records from the African Pollen Database showed that the northward expansion of tropical species started at 12 ka, reached its maximum extent (around 15 N) between 10 – 8 ka before declining around 5 ka (Watrin et al., 2009). The southward expansion of Saharan species started around 7 ka. Pollen and dinoflagellate analyses on a marine core from equatorial Africa showed an expansion of forest vegetation coinciding with lower salinity, reflecting humid conditions prevalent after the end of the Younger Dryas to the end of the GSP around 5.5 ka (Marret et al., 2013). While the vegetation changes that occurred southwards of the northern extent of the present day Sahara are relatively well understood, recent records from Morocco (Cheddadi et al., 2021; Tabel et al., 2016), Tunisia (Jaouadi et al., 2016) and southern Spain (Jimenez-Moreno et al., 2020) have shown that the signature of the AHP northwards of 25 °N is still unclear and requires further investigation in the context of the Mediterannean influence on regional climate.

Two compilations of pollen records provide regional-scale quantitative estimates for precipitation, and are especially relevant for comparison with climate model outputs. Bartlein et al. (2011) applied modern analogue, regression and model-inversion techniques to obtain a pollen-based gridded reconstruction of mean annual precipitation anomalies during the MH. Positive anomalies exceeding 200 mm were

reconstructed over northern Africa, with some regions showing increases of more than 500 mm. Negative anomalies of more than 100 mm were reconstructed over equatorial Africa, suggesting a northward shift in the rainbelt. Based on this reconstruction, Brierley et al. (2020) reported a median increase of about 400 mm over the Sahara and Sahel region (15-30 °N, 20 °W – 40 °E) during the MH. In another compilation study, Hely et al. (2014) applied probability density functions to records from the African Pollen Database to understand the latitudinal migration of the north African vegetation groups from 15 ka to the present. Their analysis of richness and abundance shows an onset of the WAM intensification between 13-11 ka, an optimum phase of the GSP between 10-6 ka with a maximum northward extension of plants around 8.5 ka, and a termination around 4.5 ka. The distribution of Guineo-Congolian taxa and Sudanian taxa (which presently occur in regions receiving more than 1500 mm and between 500-1500 mm of annual precipitation, respectively) showed a core area between 15-20 °N and a maximum potential extension of 20 °N and 25 °N, respectively. The paleo-vegetation distribution provided constraints on precipitation estimates for different latitudinal bands as well as indicated a northward migration of the core rainbelt to 15-20 °N, with seasonal and relatively drier conditions southwards.

Dust records

The reconstructions from the marine core site ODP658 off Mauritania showed clear temporal boundaries for the AHP at 14.8 ka and 5.5 ka with abrupt changes of nearly 50% to terrigenous dust fluxes (Adkins et al., 2006; DeMenocal et al., 2000) The climatic transitions were found to have occurred within decades to centuries, suggesting critical thresholds in the boreal summer insolation which led to non-linear behaviour in the regional climate. A similar increase in wind-blown dust at the end of the GSP was recorded much later at the eastward site of Lake Yoa, Chad, at around 4.3 ka, marking the time when the modern atmospheric circulation was established in that region (Kröpelin et al., 2008). A study of five marine cores off the northwestern coast of Africa refined age estimates of the transition in and out of the GSP to 11.8 ka and 4.9 ka (McGee et al., 2013). By accounting for fluvial and shelf-derived sediment fluxes, the study showed that the reductions in eolian dust fluxes at the GSP transitions were sharper and more abrupt than previously estimated from the study at ODP Site 658C. Notably, their work indicated that the dust fluxes between 8-6 ka were about a fifth of the present-day (2-0 ka) dust fluxes. Recently, another study focusing on dust records from the northwestern coast of Africa as well as the Red Sea and Gulf of Aden constrained northward extents of the GSP in the western and eastern parts of the Sahara at 28 °N and 22 °N, respectively (Palchan & Torfstein, 2019).

Lake records

A compilation of paleoenvironmental records for the purpose of generating a land surface map for the MP indicated that lake extent (reconstructed from shoreliens features and lake deposits) was around 2.8% of the total land surface between 10 – 30 °N (Hoelzmann et al., 1998). Another compilation of over 1500 paleohydrological records between 10 – 28 °N indicated that lakes, playas and rivers had their maximum extension between 19-21 °N at about 8.5 ka (Lézine et al., 2011). While small lakes and wetlands were present throughout northern Africa during the GSP, five notable "megalakes" have been reconstructed: Chad (Simon J. Armitage et al., 2015), Nubian / Darfur (Pachur & Rottinger, 1997), Fazzan (S J Armitage et al., 2007), Ahnet (Conrad & Lappartient, 1991) and Chots (Causse et al., 2003). Hydrologic modeling suggests that over 1200 mm of annual precipitation would be required to sustain such megalakes, however, this is not corroborated by other proxy reconstructions in the region or with climate model simulations; thus, their existence (or proposed extent) remains an area of active debate (Quade et al., 2018).

Other records

Other notable reconstructions for various aspects of the GSP include diatom records that provide estimates for lake salinities (Gasse, 2002; Roubeix & Chalié, 2019), paleo-drainage records based on satellite imagery (Skonieczny et al., 2015), organic biomarker records that provide precipitation estimates (Cheddadi et al., 2021; Collins et al., 2017; Shanahan et al., 2015; Tierney, Pausata, et al., 2017) and speleothem records that provide constraints on precipitation as well northern extent of the WAM (Ait Brahim et al., 2019; Sha et al., 2019). A recent compilation of records centered around the Saharan desertification provides references for 138 proxy records for further study (Dallmeyer et al., 2020).

2.2   Paleoclimate modelling of the Green Sahara

Modelling studies of the MH Green Sahara can be broadly classified into three groups: (a) Experiments without any vegetation forcings, (b) experiments with vegetation forcings using dynamic vegetation models, and (c) experiments with vegetation forcings using prescribed vegetation changes.

2.2.1 Experiments without vegetation forcings

The Paleoclimate Modelling Intercomparison Project (PMIP) coordinates climate model experiments for various time-slices of interest to the paleoclimate community, allowing for multi-model comparisons and analyses. The MH has been a time period of interest from the first phase of PMIP (PMIP1) in the early 1990s to its current phase (PMIP4). It is one of the two entry cards (mandatory experiments for participation) for PMIP4 (Kageyama et al., 2018). The PMIP experimental design recommends the same boundary conditions for vegetation for the PI and the MH, but specifies changes to the orbital parameters and GHG concentrations (B. Otto-Bliesner et al., 2017).

Successive phases of PMIP multi-model analyses have shown that climate models cannot reproduce the Green Saharan changes over northern Africa by considering only the changes to the orbital forcings or greenhouse gas concentrations. A comparison of proxy reconstructions with atmosphere-only models that participated in PMIP1 showed a large (~400 mm/year) difference in reconstructed and simulated median anomalies in precipitation (Pascale Braconnot et al., 2012). Coupled ocean-atmosphere models that participated in PMIP2 underestimated precipitation anomalies over northern Africa by over 300 mm/year compared to proxy reconstructions (Pascale Braconnot et al., 2012). The next generation of climate models that participated in PMIP3 also drastically underestimated precipitation over northern Africa when compared to proxy reconstructions, with most models simulating no increase in precipitation north of 18° N (Pascale Braconnot et al., 2012; Tierney, Pausata, et al., 2017). Finally, the multi-model ensemble from the latest PMIP phase (PMIP4), while showing an improvement over PMIP3, still under-estimates the precipitation changes during the MH (C. M. Brierley et al., 2020b), confirming again that accounting for orbital forcings and greenhouse gas changes is not sufficient to simulate the climate of northern Africa during the MH.

2.2.2 Experiments with vegetation forcings using dynamic vegetation models

Multi-model analyses from the various PMIP phases have shown that models with dynamic vegetation do not necessarily simulate the Green Sahara adequately. Ocean-atmosphere-vegetation models participating in PMIP2 underestimated precipitation anomalies over northern Africa by nearly 300 mm/year, representing a very modest improvement over ocean-atmosphere models (Pascale Braconnot et al., 2012; Hargreaves et al., 2013). A comparison of PMIP2 and PMIP3 models showed that while models with dynamic vegetation showed higher precipitation over northern Africa relative to models without

dynamic vegetation, the increase in precipitation was not comparable to that reconstructed from pollen and organic biomarker records (Tierney, Pausata, et al., 2017).

More recently, some studies with dynamic vegetation have begun to show a reasonable representation of the Green Sahara. These include transient simulations for the Holocene with the Max Planck Institute for Meteorology Earth System Model (MPI-ESM) (Dallmeyer et al., 2021), the Institut Pierre Simon Laplace (IPSL) ESM (Pascale Braconnot et al., 2019) and the HadCM3 model (Hopcroft & Valdes, 2021). However, dynamic model simulations are not a focus of this thesis.

2.2.3 Experiments with vegetation forcings using prescribed vegetation

In lieu of dynamic vegetation, several studies have prescribed vegetation changes to study the MH Green Sahara. Experiments with EC-Earth version 3.1 showed that prescribing shrub vegetation over the Sahara led to precipitation anomalies of 2 mm/day over large parts of the Sahara, with maximum anomalies of more than 6 mm/day around 15° N (Pausata et al., 2016). The northern extent of the WAM was extended from 14° N to 26° N. Combining vegetation changes with reductions to dust led to further intensification of the WAM such that its northern extent reached 31° N. Experiments with isotope enabled Community Earth System Model version 1.2 also showed an intensification of WAM due to inclusion of vegetation changes, with precipitation anomalies of 1-2 mm/day over the Sahara (Tabor et al., 2020a). Another study using the same model and similarly prescribed vegetation changes simulated a northern extent of the WAM of 24° N (Thompson et al., 2021). Finally, experiments with the University of Toronto version of the Community Climate System Model version 4 showed that vegetation changes alone pushed the desert-steppe transition to 23° N. When combined with soil and lake extent modifications, precipitation anomalies of 100-500 mm/year resulted over northern Africa (Chandan & Peltier, 2020).

2.3 Remote effects of the Green Sahara: State of the Art

Previous simulations that explicitly incorporated the Green Saharan have elicited several potential teleconnections (Figure 2-2). These teleconnections are either not observed in simulations without the Green Saharan conditions, or are only weakly represented so as to make it difficult to identify them against natural climate variability.

Successive rounds of PMIP experiments have shown that large parts of South America were drier during the mid-Holocene, owing to a weakening of the South American monsoon system as a response to the changes in orbital forcings (P. Braconnot et al., 2007; C. M. Brierley et al., 2020a; Prado et al., 2013; Valdes, 2000). Simulations with the atmosphere-ocean Institute Pierre et Simon Laplace (IPSL) CM1 model coupled to the BIOME1 vegetation model suggested that vegetation changes over northern Africa further led to amplification of orbitally-driven reduction in precipitation over the South Atlantic Convergence Zone (SACZ) region in South America during austral summer (Silva Dias et al., 2009) which is associated with the South American Monsoon (Marengo et al., 2012). A more recent study with the isotope-enabled Community Earth System Model demonstrated improved agreement of speleothem data with simulated δ^{18}O signatures from simulations including Green Saharan vegetation changes, relative to the simulations that included only PMIP4 recommendations for the MH (Tabor et al., 2020a). Simulations with the Green Sahara included vegetation changes which led to reductions in dust through the use of a prognostic dust module. The results suggested that anomalous warmth over northern Africa due to a vegetated Sahara shifted the ITCZ northwards during boreal autumn and winter, as well as reducing precipitation in the domain of the South American Monsoon.

Early climate modelling studies suggested that the mid-Holocene was associated with a suppression of El Niño activity (Clement et al., 2000; Z. Liu et al., 2000; B. L. Otto-Bliesner et al., 2003). Results from successive rounds of PMIP experiments confirmed an orbitally-driven decrease in ENSO amplitude (An & Choi, 2014; Brown et al., 2020; Zheng et al., 2008), however, this decrease appears to under-estimate reconstructed ENSO suppression (Emile-Geay et al., 2016; McGregor & Gagan, 2004). Simulations with the coupled atmosphere-ocean model EC-Earth, which incorporated the Green Sahara through prescribed vegetation and reduced dust, indicated that ENSO variability during the MH was further reduced due to the Green Sahara through a modulation of the Atlantic Niño and the Walker Circulation (Pausata, Zhang, et al., 2017). Notably, the reduction in ENSO variability due to the Green Sahara was more than twice the orbitally-driven reduction.

Experiments with the Earth model of intermediate complexity LOVECLIM indicated that Saharan desertification led to significant cooling over the Arctic during the middle-late Holocene (Davies et al., 2015). In their experiments, up to 40% of the Arctic cooling between 9 – 0 ka was attributed to Saharan desertification. These results were corroborated by simulations with the coupled atmosphere-ocean model EC-Earth, wherein the Saharan desertification was found to reduce heat transport from the lower

latitudes towards the Arctic (Muschitiello et al., 2015). As a corollary, the Green Sahara would have led to greater heat transport to the Arctic and presumably contributed to Arctic warming during the early-middle Holocene. Experiments with the coupled atmosphere-ocean Community Earth System Model also suggested that the Green Sahara led to an intensification of the Atlantic Meridional Overturning Circulation due to advection of salinity anomalies to deep-water formation regions (Zhang et al., 2021).

In other regions of the world, simulations with EC-Earth have shown an impact on tropical cyclone activity (Pausata, Emanuel, et al., 2017), Northern Hemisphere land monsoons (Sun et al., 2019), South east Asian precipitation (Griffiths et al., 2020) and East Asian summer monsoon (Piao et al., 2020). High-resolution simulations using the Canadian Regional Climate Model and the Weather Research and Forecasting regional climate model have further corroborated the impact of the Green Sahara on tropical cyclones in the Atlantic (Dandoy et al., 2021) and South and Southeast Asian precipitation (Huo et al., 2021), respectively. Combined, these studies point to the amplification of orbitally-driven changes by the Green Saharan vegetation and land surface changes, reinforcing the necessity of adequately incorporating them in studies of MH climate.

2.4   Hypotheses

The focus of this thesis is on three key regions for which there is some evidence of a potential Green Saharan impact. Using a multi-model and proxy-model intercomparison approach, the following three hypotheses are investigated:

a) The Green Sahara led to an amplification of the orbitally-driven decrease in precipitation over different regions of South America, by weakening the South American Monsoon System.

b) The Green Sahara led to a reduction in ENSO variability through modulations to the Walker Circulation.

c) The Green Sahara led to an increase in temperatures over the north Atlantic and the Artic regions, potentially reconciling proxy-model differences in estimates for the Global Mean Surface Temperatures; and the Saharan desertification was not driven by changes in Arctic temperatures.

2.5   Objectives of this thesis

Previous studies regarding potential remote effects of the Green Sahara are limited by the use of a single model, raising the possibility of model-dependent conclusions. It is further possible that emergent teleconnections may be an artifact due to specific pathways used to simulate the Green Sahara such as the incorporation of specific land surface changes. This thesis is an attempt to provide multi-model and multi-method evidence for teleconnections that operated during the MH, supported by proxy-model comparisons to demonstrate greater realism of simulations that incorporate the Green Sahara and show the aforementioned teleconnections.

Thus, the objectives of this thesis are:

  i.   To identify whether the MH Green Sahara had an impact on South American hydroclimate, including potential mechanisms.
 ii.   To evaluate whether the reduction in the variability of the El Niño Southern Oscillation is a robust multi-model result, and to test the mechanism previously hypothesized for it.

To determine if a teleconnection existed between the MH Green Sahara and the Arctic, and the dominant direction (if any) for it.

2.6   Methodology

This thesis focuses on the use of paleoclimate model simulations to study the MH climate. Outputs from the following five fully coupled global climate models were analyzed: EC-Earth version 3.1 (Hazeleger et al., 2010), isotope-enabled Community Earth System Model or iCESM (Brady et al., 2019), University of Toronto version of Community Climate System Model referred to as UofT-CCSM4 (Peltier & Vettoretti, 2014), GISS E2.1-G (Kelley et al., 2020) and HadCM3 (Valdes et al., 2017). These models were chosen on the basis of availability of equilibrium MH simulations that incorporated Green Saharan conditions in addition to reference MH simulations following PMIP protocols only. One atmosphere-only global climate model – the Global Environmental Multiscale (GEM) model version 4.8.12 (Girard et al., 2014; McTaggart-Cowan et al., 2019) – was also used to conduct experiments for the third chapter.

For each model, two sets of MH simulations were studied – with and without the Green Sahara. All MH simulations incorporate changes to orbital forcings and greenhouse gas concentrations, as suggested by PMIP protocols. The simulations without the Green Sahara are referred to as MH_{PMIP} simulations. The simulations with the Green Sahara *additionally* incorporate vegetation and land surface changes, and are referred to as MH_{GS} simulations. Model evaluation is carried out through a comparison of PI simulations with modern observations, to assess if the models satisfactorily reproduce broad-scale features of the climate system. To mitigate the influence of model biases on conclusions, I focus on comparing MH − PI anomalies among the different models.

Lastly, model estimates for anomalies in temperature and precipitation were compared with those from proxy reconstructions using metrics such as the Cohen's Kappa (κ) and Root Mean Square Errors. The proxy datasets used for these calculations include pollen-based mean annual precipitation estimates (Bartlein et al., 2011), lake level records (Tierney et al., 2011), a multiproxy dataset for South America (Gorenstein et al., 2022), multiproxy reconstructions compiled for studying the MH ENSO (listed in Chapter 3) and the Temp12k dataset (D. Kaufman et al., 2020).

2.7   Structure of the thesis

Following the three objectives listed earlier, this thesis is structured into three chapters, each focusing on one region that was demonstrably impacted by the mid-Holocene Green Sahara.

The first chapter introduces the subject of the thesis.

The second (current) chapter provides an overview of the literature concerning proxy reconstructions and climate modelling of the Green Sahara, along with a discussion of its known remote impacts.

The third chapter is focused on the teleconnection between the Green Sahara and the hydroclimate of South America. While orbital changes were known to lead to a reduction in precipitation over South America, especially during boreal winter, this article presents robust evidence that the Green Sahara further amplified the insolation-driven drying and extended it to other seasons. The article was published

under the title "*On the Remote Impacts of Mid-Holocene Saharan Vegetation on South American Hydroclimate: A Modelling Intercomparison*" in *Geophysical Research Letter*s in June 2023.

The fourth chapter is focused on the influence of the Green Sahara on the El Niño Southern Oscillation. The article highlights how the Green Sahara led to an increase in Atlantic Niño variability, altered the Walker Circulation and resulted in a reduction in El Niño variability. The article was submitted to *AGU Advances* under the title "*Mid-Holocene ENSO variability altered by northern African vegetation changes: a model intercomparison study*" in January 2024. It is currently under review in *Communications Earth and Environment* since January 2025.

The fifth chapter explores a teleconnection between the Green Sahara and the Arctic. Motivated by seemingly synchronous changes in northern Africa (Saharan desertification) and the Arctic (neoglacial cooling), this chapter is focused on determining whether the changes over either region affected the climate over the other. This chapter is in preparation under the title "*On the mid-Holocene Green Sahara-Arctic teleconnection*", for expected submission to *Nature Geoscience* in February 2025.

The concluding chapter presents a summary of the results of my work, with an attempt to place them in a broader context of global impacts of the Green Sahara. I also discuss limitations of this work and a few promising directions for future research.
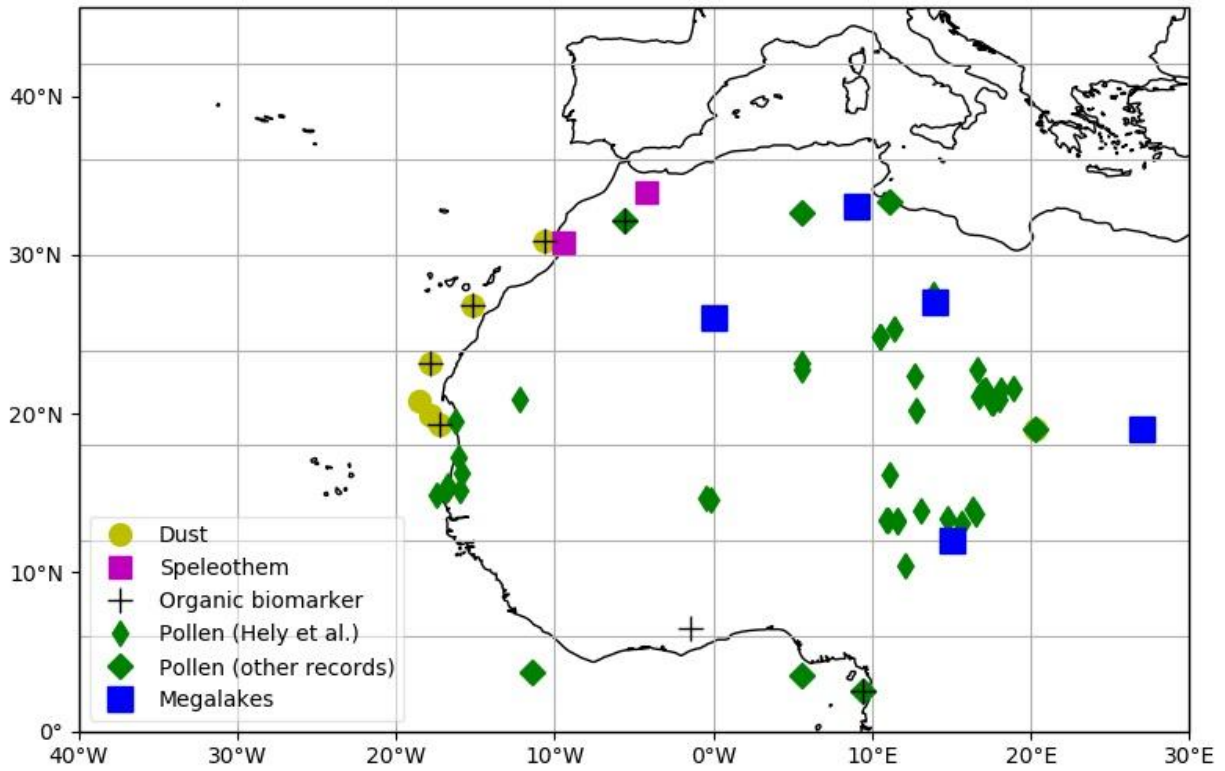
Figure 2-1 Location of key proxy records for the GSP.
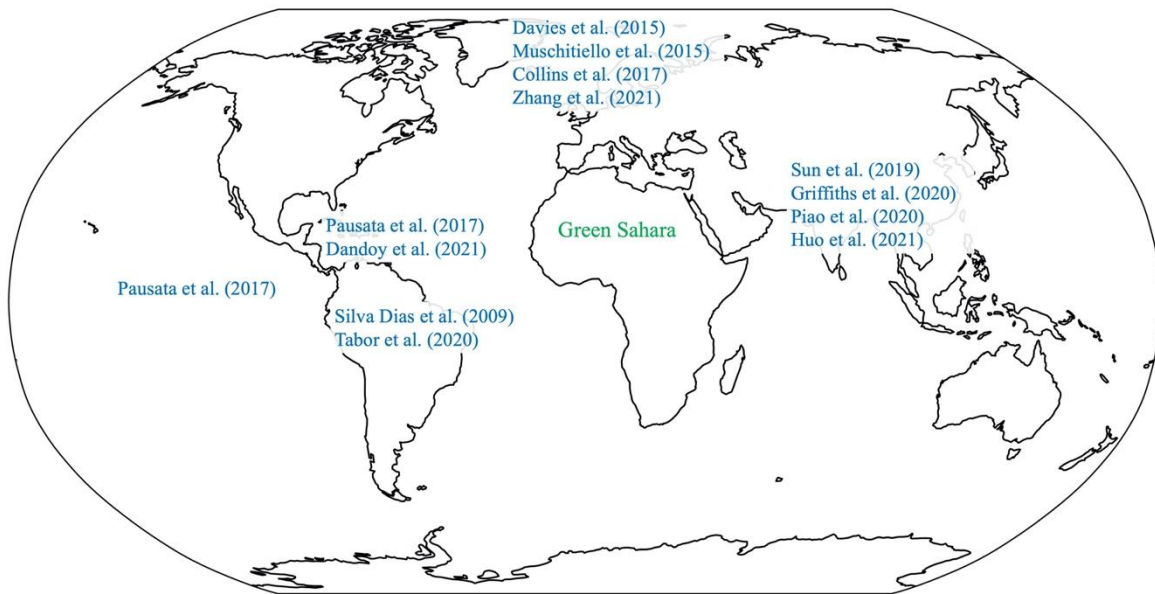
Figure 2-2 Synthesis of studies of the remote effects of the MH Green Sahara.

CHAPITRE 3

On the Remote Impacts of Mid-Holocene Saharan Vegetation on South American

Hydroclimate: A Modeling Intercomparison

S. Tiwari[1], R. D. Ramos[2], F. S. R. Pausata[1], A. N. LeGrande[3,4], M. L. Griffiths[5], H. Beltrami[6], I. Wainer[7], A. de Vernal[1], D. T. Litchmore[4,3], D. Chandan[8], W. R. Peltier[8], and C. R. Tabor[9]

[1]Centre ESCER (Étude et la Simulation du Climat à l'Échelle Régionale) and GEOTOP (Research Center on the dynamics of the Earth System), Department of Earth and Atmospheric Sciences, University of Quebec in Montreal, Montreal, Canada.

[2]Earth Observatory of Singapore, Nanyang Technological University, Singapore.

[3]NASA Goddard Institute for Space Studies, New York, New York, USA.

[4]Center for Climate Systems Research, Columbia University, New York, New York, USA.

[5]Department of Environmental Science, William Paterson University, Wayne, New Jersey, USA.

[6]Department of Earth Sciences, St. Francis Xavier University, Antigonish, Nova Scotia, Canada.

[7]Departamento de Oceanografia Física, Química e Geológica, Instituto Oceanográfico da Universidade de São Paulo, Praça do Oceanográfico, Sao Paulo, Brazil.

[8]Department of Physics, University of Toronto, Toronto, Ontario, Canada.

[9]Department of Earth Sciences, University of Connecticut, Storrs, Connecticut, USA.

Supplementary Information for this article is provided in Annexe A.

Abstract

Proxy reconstructions from the mid-Holocene (MH: 6,000 years ago) indicate an intensification of the West African Monsoon and a weakening of the South American Monsoon, primarily resulting from orbitally-driven insolation changes. However, model studies that account for MH orbital configurations and greenhouse gas concentrations can only partially reproduce these changes. Most model studies do not account for the remarkable vegetation changes that occurred during the MH, in particular over the Sahara, precluding realistic simulations of the period. Here, we study precipitation changes over northern Africa and South America using four fully coupled global climate models by accounting for the Saharan greening. Incorporating the Green Sahara amplifies orbitally-driven changes over both regions, and leads to an improvement in proxy-model agreement. Our work highlights the local and remote impacts of vegetation and the importance of considering vegetation changes in the Sahara when studying and modeling global climate.

Résumé

Les reconstructions par proxy de l'Holocène moyen (MH : il y a 6 000 ans) indiquent une intensification de la mousson d'Afrique de l'Ouest et un affaiblissement de la mousson d'Amérique du Sud, résultant principalement de changements d'insolation induits par l'orbite. Cependant, les études de modèles qui tiennent compte des configurations orbitales et des concentrations de gaz à effet de serre de l'MH ne peuvent que partiellement reproduire ces changements. La plupart des études de modèles ne tiennent pas compte des changements remarquables de la végétation qui se sont produits pendant l'MH, en particulier au-dessus du Sahara, ce qui empêche des simulations réalistes de la période. Ici, nous étudions les changements de précipitations en Afrique du Nord et en Amérique du Sud à l'aide de quatre modèles climatiques mondiaux entièrement couplés en tenant compte du verdissement du Sahara. L'intégration du Sahara vert amplifie les changements induits par l'orbite dans les deux régions et conduit à une amélioration de la concordance entre le modèle proxy et le modèle. Notre travail met en évidence les impacts locaux et éloignés de la végétation et l'importance de prendre en compte les changements de végétation dans le Sahara lors de l'étude et de la modélisation du climat mondial.

3.1   Introduction

Vegetation cover is known to impact regional climate variability, but the magnitude and global implications of vegetation changes are not well constrained due to the limited variability over the historical period. The Paleoclimate Modeling Intercomparison Project (PMIP) coordinates experiments to determine consistent responses across models that, when constrained against proxy reconstructions, can provide for a deeper understanding of how the climate system operates (Pascale Braconnot et al., 2012; Kageyama et al., 2018; B. Otto-Bliesner et al., 2017). A key interval for study is the mid-Holocene (MH), which refers to the time-slice around 6,000 years ago. The MH was characterized by paleogeographic and ice-sheet distributions comparable to today, but the orbital configuration and greenhouse gas (GHG) composition differed. Most notably, the perihelion occurred during boreal autumn as opposed to boreal winter today, enhancing Northern Hemisphere seasonality. The Northern (Southern) Hemisphere received greater (lesser) summer insolation relative to the present day. In addition, carbon dioxide and methane compositions were lower by ~7% and ~26% respectively, relative to the pre-industrial (PI) period (B. Otto-Bliesner et al., 2017). These differences are prescribed in the coordinated PMIP4 midHolocene experiments. The PMIP4 MH simulations indicate stronger monsoons in the Northern Hemisphere, especially over northern Africa (C. M. Brierley et al., 2020b). This is supported by multi-proxy reconstructions from various archives such as organic biomarkers (Collins et al., 2017; Shanahan et al., 2015; Tierney, Pausata, et al., 2017), dust (McGee et al., 2013; Palchan & Torfstein, 2019), pollen (Bartlein et al., 2011; Hély et al., 2014), speleothems (Sha et al., 2019) and paleohydrological records (Gasse, 2000; Lézine et al., 2011). However, proxy-model comparisons indicate that climate models generally under-estimate the magnitude of African precipitation change with too little rainfall to support the proxy reconstructed vegetation (Pascale Braconnot et al., 2012; C. M. Brierley et al., 2020b; Tierney, Pausata, et al., 2017).

The proxy-model discrepancy over northern Africa may be resolved to great extent through the incorporation of appropriate vegetation in climate models. There is considerable evidence that there were large-scale vegetation changes throughout the world during the MH (Bartlein et al., 2011). Most notably, the expansion of grasslands and shrubs into the current desert region of the Sahara (the so-called "Green Sahara"; e.g., Hély et al., 2014) led to significant amplification of the orbital-driven strengthening of the West African monsoon (WAM) through positive nonlinear feedbacks such as vegetation, dust and albedo feedbacks (Pausata et al., 2020; A. L. S. Swann et al., 2014). The incorporation of these changes, either

23

through dynamic vegetation (e.g., Dallmeyer et al., 2021; Levis et al., 2004; Rachmayani et al., 2015) or through the prescription of vegetation distributions (e.g., Chandan & Peltier, 2020; Pausata et al., 2016; Thompson et al., 2021), leads to simulations that are more consistent with proxy reconstructions. An important consequence of more realistic simulations is the enhanced ability to identify the far-afield impacts of the Green Sahara. For example, simulations accounting for the MH Green Sahara have elucidated the influence of the WAM on the El-Niño Southern Oscillation (Pausata, Zhang, et al., 2017), tropical cyclone activity (Pausata, Emanuel, et al., 2017), global monsoon systems (Griffiths et al., 2020; Huo et al., 2021; Piao et al., 2020; Sun et al., 2019; Tabor et al., 2020a) and high latitude climate (Muschitiello et al., 2015). While the regional changes that accompanied the Green Sahara are well-recognized, its remote impacts warrant further exploration.

The MH WAM intensification occurred in parallel with a reduction in precipitation over parts of South America. Proxy reconstructions from pollen, sedimentological and isotopic records indicate that a drier MH climate prevailed over most of tropical South America (Baker et al., 2001; Cruz et al., 2005; Novello et al., 2017; see Gorenstein et al., 2022 for a synthesis); some exceptions are found from the Cariaco Basin (Haug et al., 2001), northeast Brazil (Cruz et al., 2009), and eastern Amazonia (Wang et al., 2017). While PMIP4 models in general capture this reduction in precipitation (C. M. Brierley et al., 2020b; C. Brierley & Wainer, 2018), closer inspection reveals less consistency amongst them regarding the reduction in South American precipitation, compared with northern Africa where the models display greater agreement (C. M. Brierley et al., 2020b).

The South American Monsoon System (SAMS) brings precipitation during austral summer over the region extending from southern Amazon to southeastern Brazil (Garreaud et al., 2009; Marengo et al., 2012). The MH drying over South America has been attributed primarily to lower summer insolation and dampened seasonality in the Southern Hemisphere, which led to a weakening of the SAMS. However, few studies have addressed the mechanisms by which the MH Green Sahara could have impacted South American climate. Silva Dias et al. (2009) studied the effect of vegetation changes with two MH experiments: the first considered changes only in orbital parameters, the second additionally incorporated vegetation changes by asynchronously coupling a vegetation model to an ocean-atmosphere climate model. They observed that vegetation feedbacks could enhance some orbitally driven patterns, especially the displacement of the Intertropical Convergence Zone (ITCZ). Recently, Tabor et al. (2020) used a water isotope-enabled Earth System Model to simulate $\delta^{18}O$ changes during the MH and compare them with

speleothem reconstructions. They found that the incorporation of the Green Sahara led to better proxy-model agreement with the amplification of the drying signal over South America.

Therefore, tropical African vegetation changes are a critical prerequisite for a realistic simulation of MH climate. Given the influence of Africa over South American climate (Chen et al., 1999; Cook et al., 2004), inclusion of vegetation changes is necessary for the estimation of the remote impacts of the Green Sahara. In this study, we investigate the response of the climate of northern Africa and South America to the incorporation of a Green Sahara. To this end, we examine the differences between two MH simulations—with and without the Green Sahara—based on simulations from four coupled global climate models. To the best of our knowledge, this is the first model intercomparison study regarding the effects of land surface changes due to the Green Sahara. We also present a semi-quantitative assessment of the improved proxy-model agreement upon the inclusion of the Green Sahara, which lends further support to our approach.

3.2   Methods

For this study, we analyzed outputs from four global climate models—(a) EC-Earth version 3.1 (Hazeleger et al., 2010), (b) the water isotope-enabled Community Earth System Model version 1.2 (iCESM1; Brady et al., 2019), (c) University of Toronto version of CCSM4 (hereby referred to as UofT-CCSM4; Peltier & Vettoretti, 2014), and (d) the water isotope-enabled GISS-E2.1-G (Kelley et al., 2020). Details about the atmospheric and oceanic components of these models and their associated grids are provided in **Erreur ! Source du renvoi introuvable.** in Annexe A. Three simulations were analyzed for each model—one for the pre-industrial (PI) and two for the MH climate state. The first MH experiment follows the standard forcings and boundary conditions as specified by the PMIP4 guidelines (B. Otto-Bliesner et al., 2017) and is referred to as MH$_{PMIP}$. The second MH simulation, which additionally incorporates a Green Sahara by prescribing vegetation over northern Africa, is referred to as MH$_{GS}$. While the representation of the Green Sahara is different in each climate model, it follows the paleo distributions of vegetation suggested for the PMIP4 sensitivity experiments (B. Otto-Bliesner et al., 2017; further details in Text S2 in Annexe A).

To validate the models, we compared climatological outputs from PI simulations with the Global Precipitation Climatology Center (GPCC) Reanalysis Dataset from 1951 to 1980 (Schneider et al., 2011) and

the Global Precipitation Climatology Project (GPCP) dataset v2.2 from 1979 to 2009 (Adler et al., 2003) (Text S1 and Figure A 2 in Annexe A). Models have varying ability to simulate the climate over South America and the equatorial Atlantic Ocean, with EC-Earth showing superior ability to represent modern climate (see Text S1 in Annexe A for details about model biases and differential model performance). However, all models broadly reproduce the magnitudes and distributions of annual precipitation over the study area. Further, to redress the effect of model biases, we discuss our results in terms of MH - PI differences. We interpret the MH_{PMIP} – PI anomalies to reflect the effects of changes in orbital parameters and GHG concentrations, and the MH_{GS} – MH_{PMIP} anomalies to reflect the additional effect of the Green Sahara. All model climate variables are analyzed as averages over 100 simulation years.

To quantify proxy-model agreement, we use the Cohen's κ statistic, modifying it to implement weights for total disagreement, partial disagreement and agreement (Text S3 in Annexe A).

3.3   Results

The MH_{PMIP} simulations indicate a small but significant increase in precipitation of 0.5 mm/day over almost the entirety of northern Africa, extending beyond 30°N (Figure 3-1). The intensification of the WAM is larger over the Sahel, where it reaches the order of 1–2 mm/day between the equator and 15°N and is also reflected in stronger low-level (850 hPa) southwesterly monsoon winds. The patterns and magnitude of the increase in mean annual precipitation over northern Africa are consistent across all four models. EC-Earth 3.1 shows the highest increase of 2 mm/day over the core rainfall belt. The intensification of the WAM in the MH_{PMIP} simulations is accompanied by a decrease in mean annual precipitation over some regions of South America. This decrease is on the order of 0.5–2 mm/day but the spatial extent of the change differs among the models. EC-Earth 3.1 and GISS-E2.1-G capture a widespread decrease across nearly the full meridional extent of the continent. The UofT-CCSM4 simulation shows a greater decrease, but limited to parts of northwestern Amazon, while iCESM 1.2 shows a modest decrease of up to 0.5 mm/day in the southern half of the continent. All models show a decrease in precipitation just north of the equator in the Atlantic Ocean.

Comparing the MH_{PMIP} and the MH_{GS} simulations (Figure 3-1), we observe an amplification of orbitally-driven changes in rainfall. The increase in precipitation over northern Africa is intensified and extends

further north, with three out of four models showing an increase of 0.5–1 mm/day up to 25°N. The core rainfall belt is between 10 and 20°N, with an increase in precipitation in the order of 1–3 mm/day. EC-Earth 3.1 shows the greatest increase in the core rainfall belt, exceeding 4 mm/day between 12 and 16°N. Across the Atlantic, all models suggest greater and more widespread drying of up to 2 mm/day over South America. The drying patterns appear stronger over northern South America, but more consistent over southern South America. Notably, iCESM 1.2 shows little change from the PI over northwestern South America, with a modest but significant increase in some parts of the Amazon. All models show a decrease in precipitation immediately north of the equator and an intensification in precipitation northwards of this region, suggesting a northward shift in the position of the ITCZ. None of the MH simulations indicate an increase in precipitation over northeastern Brazil, likely due to anomalous upper-level convergence over this region (Figure 3-4).

As the WAM and the SAMS operate over different seasons and different regions in South America experience different annual precipitation cycles (Marengo et al., 2012; Figure A 1 in Annexe A), it is helpful to investigate MH-PI anomalies in monthly precipitation. The multi-model mean rainfall changes in the MH_{PMIP} simulation relative to the PI indicate an intensification of the WAM from May-October (Figure A 3 in Annexe A). With the exception of austral spring (October–November), the dominant change observed over South America is a drying throughout the year. During austral winter (May-July), this drying is restricted to regions north of 10°S, which are dominantly influenced by the ITCZ. The multi-model mean change in the MH_{GS} relative to PI indicate that the increase in precipitation over northern Africa lasted longer, from March-November, with a very prominent increase over the core rainfall belt around 15°N from May–October (Figure A 4 in Annexe A). Two notable patterns are observed in the MH_{GS} simulation relative to the PI: firstly, except for November, the domain of the SAMS was drier throughout the year; secondly, the ITCZ-influenced regions in northern South America were wetter between January-May and drier through the rest of the year. Changes in annual average values aggregate some of these seasonal changes and result in a weaker drying signal in the MH_{PMIP} simulation relative to the PI. However, since the drying signal is stronger, more widespread, and extended to a longer duration through the year in the MH_{GS} simulation relative to the PI, it remains evident in the annual average as well (Figure 3-1).

The effects of incorporating the Sahara greening into the models are evident in the multi-model mean anomalies between MH_{GS} and MH_{PMIP} (Figure 3-2). The Sahara greening leads to higher precipitation over northern South America between December–May, but drying over other regions throughout the year.

Notably, the Green Sahara leads to a larger amplitude of precipitation seasonality in the equatorial areas such as the northern Amazon. This is because the expansion of the seasonal migration range of the ITCZ in the MH_{GS} scenario leads to an increase in precipitation over equatorial South America during austral summer and a decrease during the boreal summer. Lastly, the Saharan vegetation changes are associated with enhanced subsidence and drying over northeastern Brazil throughout the year (Figure 3-4).

We assessed the agreement between proxies and models under different MH experiments using weighted Cohen's κ statistic, a semi-quantitative metric to estimate the frequency of agreement between categorical data. All models show higher κ scores in the MH_{GS} (i.e., $\kappa > 0.49$, $p < 0.01$) compared to MH_{PMIP} (i.e., $\kappa < 0.48$, $p < 0.01$) experiment, with EC-Earth 3.1 and iCESM 1.2 showing the most significant improvements (Figure 3-3; Figures A 5 and A 6 in Annexe A). This indicates that the MH_{GS} simulation better simulates the extent of a wetter northern Africa and/or a drier South America during this period relative to the MH_{PMIP} simulation. Considering the proxy-model agreement between the continents, northern Africa consistently shows higher κ scores than South America (Figure A 5 in Annexe A) with all models showing a general improvement in reflecting a greener Sahara. Over South America, all models except for GISS-E2.1-G show an improvement in capturing the drier conditions in this region in the MH_{GS} experiment (Figure A 5 in Annexe A). UofT-CCSM4 performed well over northern Africa but worse over South America resulting in overall comparable κ scores between MH scenarios (Figure 3-3; Figure A 5 in Annexe A). For GISS-E2.1-G, the κ score over South America decreases but there is a general improvement over northern Africa in the MH_{GS} simulation with comparable κ scores between MH experiments (Figure 3-3; Figure A 5 in Annexe A). The observed overall improvement in iCESM 1.2 originates from the more apparent drying over South America under MH_{GS} relative to MH_{PMIP} (Figure 3-3). EC-Earth 3.1 shows the highest κ score for both continents, outperforming all models under MH_{GS} scenarios (Figure A 5 in Annexe A).

3.4   Discussion and Conclusions

In this study, we assessed the impact of paleovegetation changes during the MH by considering two simulations — with and without the Green Sahara. A model intercomparison to robustly assess the northern African land cover changes was hitherto missing. For the first time, we compare four different Earth system models in which vegetation changes over northern Africa are accounted for, and focus on the associated hydroclimate changes over northern Africa and South America. The four models in this

study have varying performance over South America, with EC-Earth representing the modern fundamental features most satisfactorily. However, irrespective of the methods used to prescribe vegetation or the ability to simulate South American climate, the models share similarities in their teleconnections across the tropical and extra-tropical Atlantic, indicating the overwhelming importance of the Green Sahara. The Sahara greening (MH$_{GS}$) enhances the rainfall over northern Africa, while further decreasing precipitation over South America relative to the case in which only orbital forcings are accounted for (MH$_{PMIP}$).

Several modeling studies have shown a reduction in precipitation over South America as well as changes to the monsoonal cycle due to changes in seasonal insolation (Shimizu et al., 2020). The orbital-driven weakening of the SAMS during austral summer is indicated by PMIP3 (Prado et al., 2013; Shimizu et al., 2020) as well as PMIP4 models (C. M. Brierley et al., 2020b). Our MH$_{PMIP}$ simulations similarly capture a drying signal, particularly over north-western South America (Figure 3-1) and provide drying estimates comparable to previous results (around 1 mm/ day). Examining the seasonal cycle indicates that South America received less insolation during austral summer and more insolation during austral spring during the MH compared with the PI, which could have altered the cycle of the SAMS (Shimizu et al., 2020). Our MH$_{PMIP}$ simulations also capture these changes through a decrease in precipitation over the SAMS region during December-February, but an increase during October–November. However, few of the previous modeling studies focused specifically on how the Sahara greening may have influenced the MH South American hydroclimate (Silva Dias et al., 2009; Tabor et al., 2020b). Our results support their findings regarding the impact of the Green Sahara in amplifying orbital-driven weakening of the SAMS, through consistent results from four different models. Furthermore, in our study we show that South America also experienced a significant reduction in precipitation during austral winter, most likely because the prescribed vegetation led to widespread moisture redistribution during austral winter (Figure 3-2). Combined with a weakening of the SAMS during austral summer, this led to longer and greater drying over South America than seen when only considering changes in orbital forcings. Thus, the drying in South America during the MH was prevalent throughout the year and not exclusively related to changes in the SAMS.

Lastly, an interesting result of this study is the absence in our MH simulations of an east-west precipitation dipole over tropical South America, which is a key feature of modern (Chen et al., 1999; Cook et al., 2004; Lenters & Cook, 1997) and last millennium (Orrison et al., 2022) South American hydroclimate. All our MH$_{PMIP}$ simulations show anomalous upper-level convergence over northeastern Brazil leading to greater

subsidence and drying in the region, an effect that is reinforced by the vegetation changes in the MH_{GS} simulations (Figure 3-4). In this regard, our results differ from previous modeling studies that performed MH_{PMIP}-type simulations and found a wetter northeastern Brazil and a drier rest of tropical South America during the MH (Cruz et al., 2009; X. Liu & Battisti, 2015). Despite the presence of some well-dated proxy reconstructions that point to the presence of a wetter MH northeastern and central Brazil (Barreto, 2010; Cruz et al., 2009; Utida et al., 2020; Wang et al., 2017), there is considerable disagreement among proxy records. Gorenstein et al. (2022) noted that out of 43 records from this region, only six sites indicate a MH wettening, whereas 26 archive a MH drying. Thus, our results point to two possibilities: (a) the presence of the Green Sahara amplifies the models' inability to simulate this feature of South American hydroclimate, or (b) the east-west precipitation dipole is not a stationary feature of South American climate and may be masked by the presence of the Green Sahara.

Various mechanisms have been proposed to explain the influence of northern African vegetation changes on South American hydroclimate. The influence of an African heat source on eastern and northeastern Brazil has previously been established by idealized experiments (Cook et al., 2004; Gandu & Silva Dias, 1998). Silva Dias et al. (2009) suggested a northward migration of the SACZ associated with a weakening of the upper-level Bolivian High and a weakened tropical circulation, influencing inland climate. Tabor et al. (2020a) discussed the role of substantial regional warming due to the Green Sahara, which resulted in a more northerly ITCZ between November and March. Precipitation over South America was likely also modulated by MH changes in the equatorial Atlantic (C. Brierley & Wainer, 2018) and the equatorial Pacific variability (Pausata, Zhang, et al., 2017), which affected the moisture budgets through perturbations to the Hadley and Walker Circulations (D'Agostino et al., 2020). Further, different mechanisms could have contributed during different times of the year. For example, Moura & Shukla (1981) suggested that anomalously warm SSTs in the northern equatorial Atlantic during boreal summer led to thermally forced subsidence and subsequent droughts in northeastern Brazil. Grimm et al. (2007) highlighted the role of reduced soil moisture during austral spring in driving summer precipitation. Thus, various factors may have led to the widespread drying observed over different regions of South America during different parts of the year. While an in-depth investigation of the mechanism(s) behind the Green Sahara's modulation of South American hydroclimate is beyond the scope of this study, our work nonetheless shows the importance of Saharan vegetation in more accurately simulating northern African and South American teleconnections during the MH. This is clear through an analysis of the annual upper-level (200 hPa) velocity potential anomalies (Figure 3-4). A comparison of MH_{PMIP} − PI and MH_{GS} − MH_{PMIP} anomalies shows

that the impact of the Green Sahara is comparable to the impact of the changes in orbital configuration and GHG concentrations (Figure 3-4). An inadequate representation of the substantial forcing imposed by the Saharan vegetation precludes an analysis of its remote impacts.

Among all simulations, the MH_{GS} simulation from EC-Earth shows the greatest proxy-model agreement over both regions. The inclusion of vegetation changes over northern Africa in the models leads to an overall improvement in Cohen's κ scores. Over Northern Africa, the MH_{PMIP} simulations capture increases of 0.5–2 mm/day, consistent with the expansion of Sahelian and Sudanian vegetation. The MH_{GS} simulations capture a northward extension of the core rainfall belt between 10 and 20°N, with increases of 1–3 mm/day which are further consistent with the expansion of Guineo-Congolian vegetation (Hély et al., 2014). In both sets of MH simulations, proxy-model disagreement in northern Africa is limited to regions which are not dominantly influenced by the WAM. However, improvement in κ scores is less apparent over northern Africa due to the reasonable ability of MH_{PMIP} simulations to capture the spatial extent of the increase in precipitation. The drivers of improvement over South America are less straightforward. On one hand, an inclusion of the Green Sahara leads to an increase in the number of sites showing proxy-model disagreement in some regions, particularly eastern Brazil. On the other hand, inclusion of the Green Sahara leads to an improvement in the ability of models to capture the spatial extent of precipitation changes over South America, leading to an increase in sites showing proxy-model agreement. These two contending factors lead to an overall improvement in three models (except GISS-E2.1-G) to capture changes indicated by proxy reconstructions over South America. A key limitation of our work is the inclusion of proxy data irrespective of dating resolution or demonstrated fidelity to extracting climatic variability. Further, our work only assesses model-proxy agreement with respect to spatial extent, and not magnitude of precipitation changes. Notwithstanding these limitations, our work highlights the importance of vegetation as key boundary condition that should be included when simulating MH climate and comparing models to paleoclimate archives.
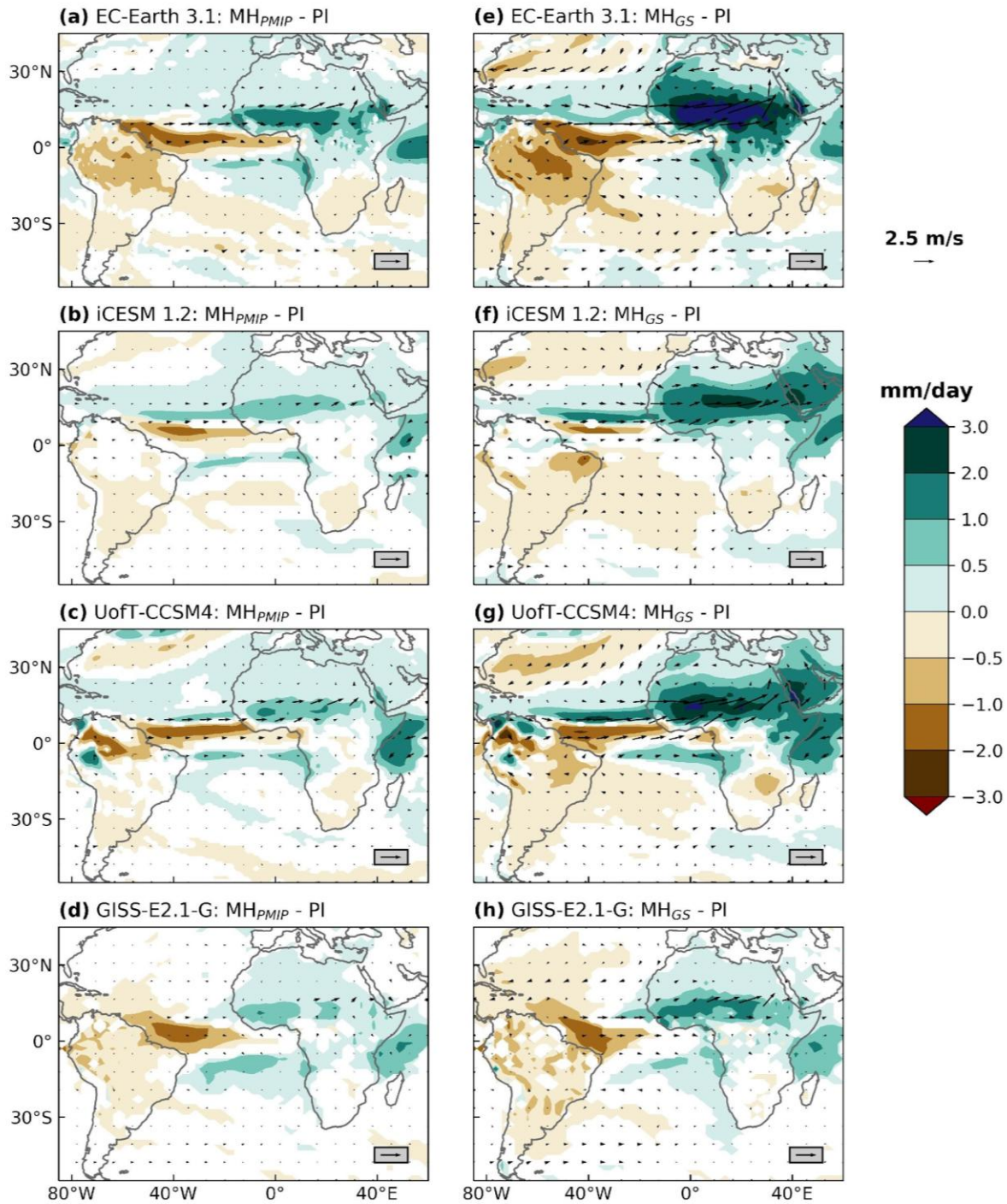
Figure 3-1 Change in annual precipitation in the MH$_{PMIP}$ (a-d) and MH$_{GS}$ (e-f) experiment relative to the PI simulation. Colors represent precipitation change in mm/day. Only changes significant at the 95% confidence level are shaded. Vectors indicate changes in low-level (850 hPa) wind strength.
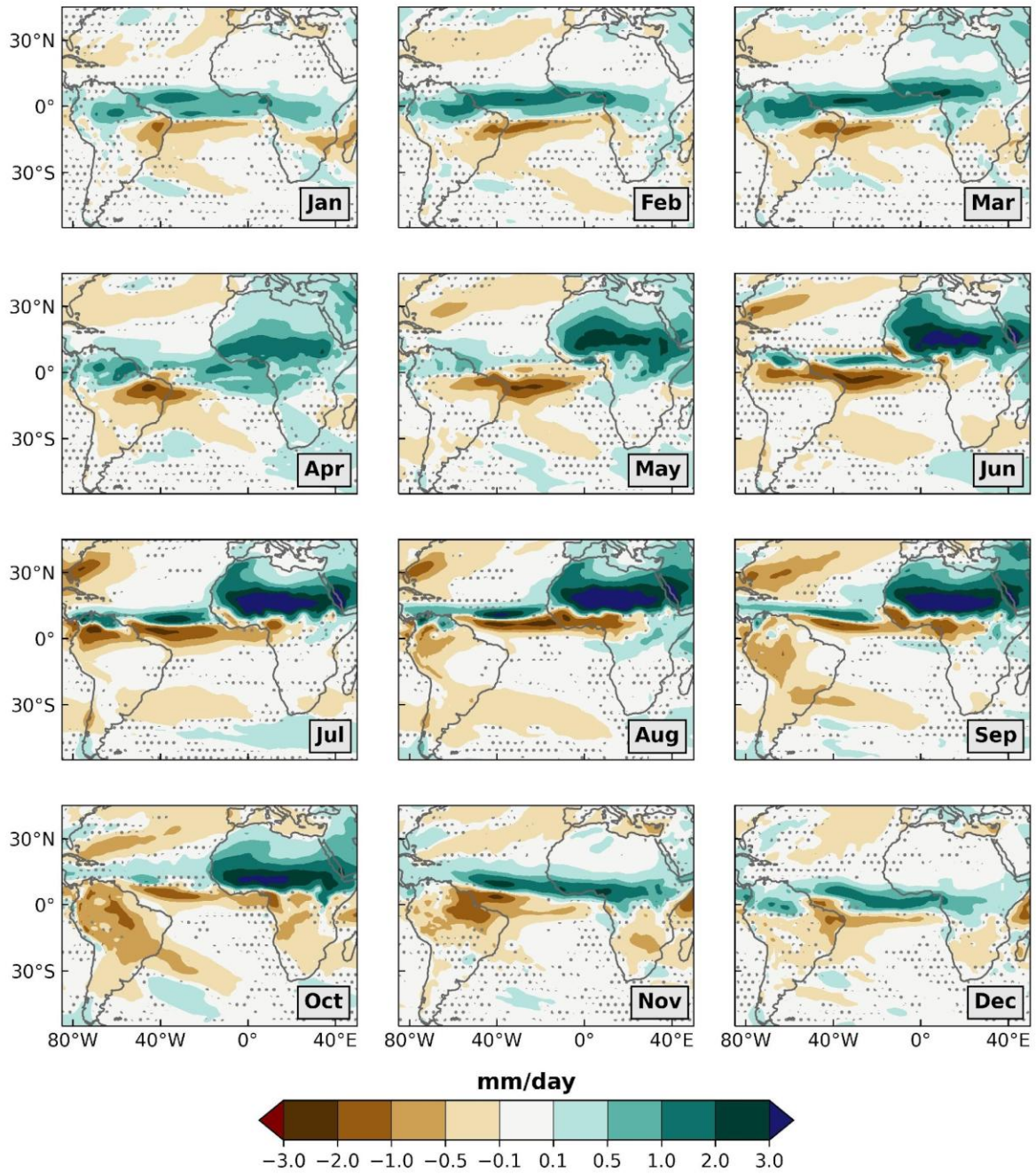
Figure 3-2 Monthly evolution of the multi-model average precipitation anomalies between MH_{GS} and MH_{PMIP}. Stippling indicates areas in which less than three models agree on the sign change.
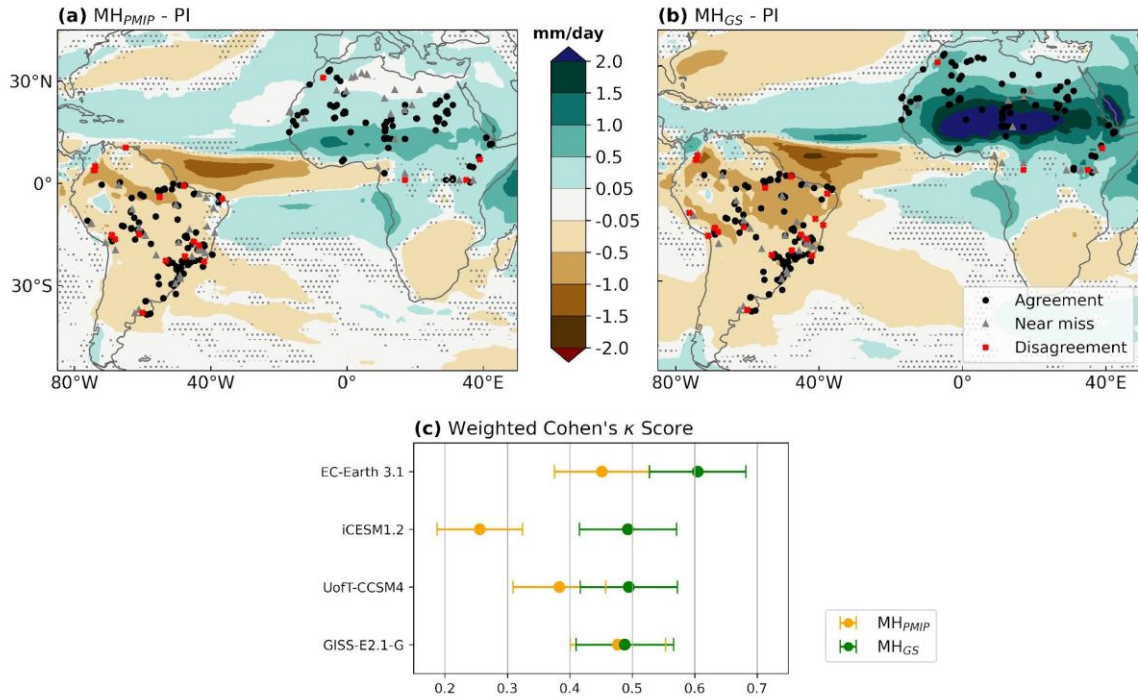
Figure 3-3 Multi-model mean change in annual precipitation, with proxy-model agreement overlain. Colors indicate (a) MH$_{PMIP}$ – PI and (b) MH$_{GS}$ – PI changes in annual precipitation in mm/day. Stippling indicates areas in which less than three models agree on the sign change. (c) Weighted Cohen's κ Scores for MH$_{PMIP}$ (orange symbols) and MH$_{GS}$ (green symbols) runs. Error bars indicate 95% confidence intervals.
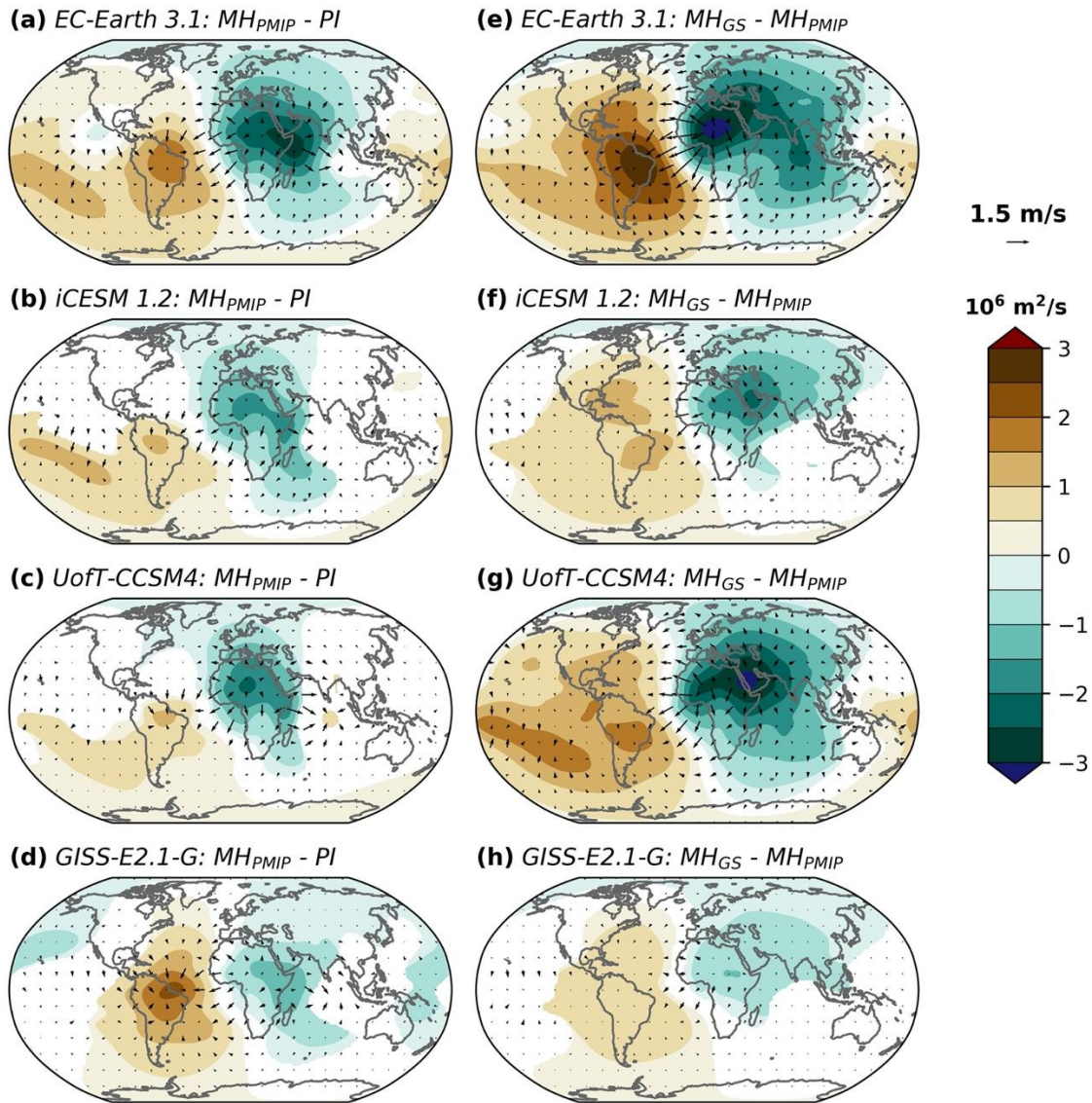
Figure 3-4 Changes in annual upper-level (200 hPa) velocity potential (a-d) for the MH$_{PMIP}$ relative to the PI experiment and (e-h) for the MH$_{GS}$ relative to the MH$_{PMIP}$ simulation. Only changes significant at the 95% confidence level are shaded. Vectors indicate changes in upper-level divergent wind.

CHAPITRE 4

Mid-Holocene ENSO Variability reduced by northern African vegetation changes: a model intercomparison study

Shivangi Tiwari[1]*, Francesco S. R. Pausata[1], Allegra N. LeGrande[2,3], Michael Griffiths[4], Ilana Wainer[5], Hugo Beltrami[1,6], Anne de Vernal[1], Peter O. Hopcroft[7], Clay Tabor[8], Deepak Chandan[9], W. Richard Peltier[9]

[1]Department of Earth and Atmospheric Sciences, University of Quebec in Montreal, Montreal, Canada.

[2]NASA Goddard Institute for Space Studies, New York, New York, USA.

[3]Center for Climate Systems Research, Columbia University, New York, New York, USA.

[4]Department of Environmental Science, William Paterson University, Wayne, New Jersey, USA.

[5]Departamento de Oceanografia Física, Química e Geológica, Instituto Oceanográfico da Universidade de São Paulo, Praça do Oceanográfico, Sao Paulo, Brazil.

[6]Department of Earth Sciences, St. Francis Xavier University, Antigonish, Nova Scotia, Canada.

[7]School of Geography, Earth and Environmental Sciences, University of Birmingham, Birmingham, UK.

[8]Department of Earth Sciences, University of Connecticut, Storrs, Connecticut, USA.

[89]Department of Physics, University of Toronto, Toronto, Ontario, Canada.

Supplementary Information for this article is provided in Annexe B.

Abstract

The relationship between the mean state of the Pacific Ocean and El Niño Southern Oscillation (ENSO) and its variability through time is inadequately understood, especially on longer timescales. Several studies have indicated that the mid-Holocene (6,000 years before present) was characterized by stronger east-west temperature contrast and lower ENSO variability relative to the present day. While climate models show a reduction in ENSO variability, they underestimate this reduction compared to many paleoclimate reconstructions. Further, the drivers behind these changes remain unclear. In this work, we use five global climate models to show that incorporating vegetation changes over northern Africa during the mid-Holocene are vital to capturing global circulation changes. Greening the Sahara alters the Walker Circulation, enhancing zonal temperature and pressure gradients in the equatorial Pacific and driving it to a La Niña-like state. Incorporating Green Sahara boundary conditions leads to reductions in interannual variability in all Niño index regions relative to orbital and GHG changes, with reductions of up to 18% in the Niño3.4 region. Our work highlights the importance of the Atlantic influence on ENSO and provides paleoclimatic evidence for this synergistic teleconnection.

Résumé

La relation entre l'état moyen de l'océan Pacifique et l'oscillation australe El Niño (ENSO) et sa variabilité au fil du temps est mal comprise, en particulier sur des échelles de temps plus longues. Plusieurs études ont indiqué que l'Holocène moyen (6 000 ans avant le présent) était caractérisé par un contraste de température est-ouest plus fort et une variabilité ENSO plus faible par rapport à aujourd'hui. Bien que les modèles climatiques montrent une réduction de la variabilité ENSO, ils sous-estiment cette réduction par rapport à de nombreuses reconstructions paléoclimatiques. De plus, les facteurs à l'origine de ces changements restent flous. Dans ce travail, nous utilisons cinq modèles climatiques mondiaux pour montrer que l'intégration des changements de végétation en Afrique du Nord au cours de l'Holocène moyen est essentielle pour saisir les changements de circulation globale. Le verdissement du Sahara modifie la circulation de Walker, augmentant les gradients de température et de pression zonaux dans le Pacifique équatorial et le conduisant à un état de type La Niña. L'intégration des conditions limites du Sahara Vert conduit à des réductions de la variabilité interannuelle dans toutes les régions de l'indice Niño par rapport aux changements orbitaux et aux GES, avec des réductions allant jusqu'à 18 % dans la région Niño3.4. Nos travaux soulignent l'importance de l'influence de l'Atlantique sur l'ENSO et fournissent des preuves paléoclimatiques de cette téléconnexion synergique.

4.1 Introduction

The El Niño Southern Oscillation (ENSO) is the largest source of interannual variability in the global climate system. Climate system teleconnections emanating from ENSO affect the lives, economic activity and livelihoods of people worldwide. It is thus necessary to understand its internal variability and its response to external forcings, especially in the context of anthropogenic impacts on ENSO variability due to climate change (Beobide-Arsuaga et al., 2021; Cai et al., 2023). Our current understanding of ENSO is primarily based on instrumental and historical records of sea-surface temperatures (SSTs) and atmospheric circulation, limited to the last ~150 years. Studying the paleoclimatic history of-ENSO provides a broader context for baseline natural ENSO variability, especially from past climates without drastic anthropogenic perturbations and with different mean states. Further, while the far-afield impacts of ENSO are widely recognized, teleconnections originating from other elements in the global climate system that impact ENSO warrant further study. Thus, an evaluation of external forcings that modulate teleconnections, which in turn affect ENSO, is vital to understanding this most prominent mode of variability in our global climate system.

The mid-Holocene (MH: 6,000 years Before Present or BP) is a key paleoclimatic interval characterized by different insolation forcing and greenhouse gas concentrations compared to the pre-industrial (PI) or the present day (Otto-Bliesner et al., 2017). Greenhouse gas concentrations were lower, with methane levels during the MH being 15% lower than the pre-industrial concentrations. Enhanced seasonal contrast in the Northern Hemisphere due to precessional changes intensified the West African Monsoon (WAM), which further led to a "Green Sahara", i.e. the expansion of shrub vegetation across northern Africa in place of the present-day Saharan Desert (Bartlein et al., 2011; Hély et al., 2014; Pausata et al., 2020). Basin-wide multi-proxy evidence from the Pacific has indicated that the MH was also characterized by a La Niña-like mean state with lower ENSO variability (see Figure B 1 for locations of proxy reconstructions discussed in this study). Proxy records from core ENSO regions such as the central equatorial Pacific (Grothe et al., 2020; White et al., 2018) and eastern equatorial Pacific (Conroy et al., 2008; Koutavas & Joanides, 2012; Moy et al., 2002) indicate fewer El Niño events, cooler and drier conditions, and a dampened ENSO during the MH. Lower ENSO variability is also shown by proxy records from ENSO-teleconnected regions such as Papua New Guinea (McGregor & Gagan, 2004), Malaysia (Chen et al., 2016) and eastern Australia (Barr et al., 2019), where changes in isotopic signatures reflecting changes in ENSO-linked precipitation are recorded. Climate models have also consistently shown that the ENSO variability during the MH was lower than for the present day (Barr et al., 2019; Clement et al., 2000; Lawman et al., 2022; Liu et al., 2000, 2014). The

Paleoclimate Modelling Intercomparison Project (PMIP) coordinates experiments for the mid-Holocene (Otto-Bliesner et al., 2017). An ensemble of PMIP3 and PMIP4 models (henceforth referred to as PMIP3/4 model ensemble) has shown a reduction in SST over the eastern and southeastern equatorial Pacific on the order of 0.5 °C and a decrease in precipitation over the equatorial Pacific of 0.1 - 2 mm/day, reminiscent of La Niña conditions (J. R. Brown, Brierley, et al., 2020). However, climate models tend to underestimate the magnitude and extent of MH ENSO changes compared to paleoclimate reconstructions. For example, a compilation of coral records indicated that ENSO variance reduced by 33-66% in different parts of the Pacific basin (Emile-Geay et al., 2016). On the other hand, few models from the PMIP3/4 model ensemble show more than a ~20% decrease in ENSO variability (J. R. Brown, Brierley, et al., 2020). The model-proxy discrepancy has previously been attributed to the lack of sufficiently long proxy data, uncertainties in the proxy reconstructions, the use of different or over-simplified metrics to estimate ENSO variability or an inadequately nuanced understanding of ENSO diversity (Emile-Geay et al., 2016; Grothe et al., 2020; Karamperidou & DiNezio, 2022; Lawman et al., 2022). Here, we explore the possibility that the model-proxy discrepancy indicates a missing teleconnection which affects ENSO, but has not been adequately captured in climate model simulations.

In recent years, the vegetation changes over the Sahara have emerged as an important driver of the MH climate, with several studies showing its remote effects on the global climate system through various teleconnections (Griffiths et al., 2020; Muschitiello et al., 2015; Pausata, Emanuel, et al., 2017; Sun et al., 2019; Tabor et al., 2020). In particular, a set of simulations with a coupled ocean-atmosphere global climate model EC-Earth version 3.1 indicated that the Green Sahara could have modulated ENSO variability through changes in the Walker Circulation (Pausata, Zhang, et al., 2017a). In contrast, most previous studies of MH ENSO focused on the effects of changes to orbital forcing, GHG concentrations, ice sheet extents and meltwater discharge, but neglected vegetation and land surface changes (Barr et al., 2019; Clement et al., 2000; Karamperidou & DiNezio, 2022; Lawman et al., 2022; Liu et al., 2000, 2014). Further, the Green Sahara does not adequately emerge in the PMIP3/4 model ensemble, indicating that incorporating orbital and greenhouse gas forcings alone does not lead to the simulation of a potential Green Sahara – ENSO teleconnection. In light of the increasingly recognized importance of the Green Sahara, model under-estimations of ENSO variability reduction, and lack of multi-model studies, it is crucial to investigate the Green Sahara – ENSO teleconnection through a model intercomparison.

The Green Sahara is hypothesized to impact ENSO variability through modulations of tropical Atlantic variability (Pausata, Zhang, et al., 2017a). Modern observational and reanalysis datasets have revealed the existence of Atlantic Niño, also called the Atlantic zonal mode, which is the leading mode of variability in the equatorial Atlantic Ocean (Lübbecke et al., 2018; Silva et al., 2021; Xie & Carton, 2004; Zebiak, 1993). Atlantic Niño events are essentially a breakdown in the development of the Atlantic Cold Tongue, which leads to anomalously warm SSTs in the eastern equatorial Atlantic Ocean. The role of tropical Atlantic variability in modulating ENSO events has been investigated in at least three contexts. First, the influence of the Atlantic was studied in the context of the climate shift of the 1970s (Ding et al., 2012; Rodríguez-Fonseca et al., 2009). Using observational datasets and model simulations, a change in the Atlantic-Pacific connection was identified, with boreal summer Atlantic Niño events shown to favor La Niña events the following winter. Secondly, ENSO hindcasts in models were shown to be improved upon the inclusion of Atlantic SST observations (Exarchou et al., 2021; Jansen et al., 2009; Keenlyside et al., 2013; Martín-Rey et al., 2015), with the equatorial Atlantic playing a more relevant role compared to the north tropical Atlantic and entire tropical Atlantic regions (Chikamoto et al., 2020). Thirdly, tropical volcanic eruptions have been found to lead to an El Niño response through the Atlantic-Pacific teleconnection in some climate models, with temperature changes over northern Africa playing a key role in generating a Matsuno-Gill response (Khodri et al., 2017; Pausata et al., 2023). Thus, regional climate changes over northern Africa and the equatorial Atlantic are a potential source of ENSO modulations.

In this work, we study MH ENSO variability in the context of the Green Sahara using simulations from five global climate models. For each model, we analyzed outputs from two MH simulations – with and without prescribed vegetation and land surface changes over northern Africa (MH_{GS} and MH_{PMIP}, respectively) to isolate the impact of the Green Sahara on the equatorial Pacific and Atlantic oceans. Both the MH_{PMIP} and MH_{GS} simulations incorporate changes in orbital parameters and GHG concentrations following PMIP recommendations. The MH_{GS} simulations additionally incorporate the presence of the Green Sahara through vegetation and land surface changes. These include prescribing various vegetation types over the Sahara, reduction of dust, changes to soil albedo and composition and including mega-lakes. The MH_{GS} simulations were carried out differently for each model, with the central idea of adequately representing the vegetation and land surface changes that occurred over northern Africa during the mid-Holocene. Regardless of the specific Green Sahara conditions, all MH_{GS} simulations show a significantly strengthened WAM relative to the MH_{PMIP} simulations, indicated through precipitation and wind strength changes (Figure B 2). A previous quantification of the proxy model agreement indicated that the MH_{GS} simulations

provide a more realistic picture of the MH than simulations that do not account for the Saharan vegetation changes (Tiwari et al., 2023). In this work, we show that all models show a consistent reduction in ENSO variability due to the incorporation of the Green Sahara, through an Atlantic-Pacific teleconnection which also operates in the present day.

4.2   Materials and Methods

4.2.1   Climate model experiments

We used five fully coupled global climate models for this study: EC Earth version 3.1 (Hazeleger et al., 2010), isotope-enabled Community Earth System Model (iCESM) version 1.2 (Brady et al., 2019), University of Toronto version of Community Climate System [UofT-CCSM4 (Peltier & Vettoretti, 2014)], water-isotope enabled Goddard Institute of Space Studies (GISS) model E2.1-G (Kelley et al., 2020) and Hadley Centre coupled model version 3 [HadCM3 (Valdes et al., 2017)]. Details about the model components and resolutions are provided in Supplementary Table S1. For each model, we ran three simulations: pre-industrial (PI), mid-Holocene following PMIP recommendations for insolation and greenhouse gas forcings (MH$_{PMIP}$) and mid-Holocene following PMIP recommendations for insolation and greenhouse gas forcings with additional vegetation and land cover changes (MH$_{GS}$). For EC Earth, PMIP3 recommendations for PI and mid-Holocene were followed (Taylor et al., 2012). For all other models, PMIP4 recommendations for PI and mid-Holocene were followed (Otto-Bliesner et al., 2017).

The MH$_{GS}$ simulations were carried out differently for each model, with the central idea of adequately representing the vegetation and land surface changes due to the mid-Holocene Green Sahara. For EC Earth, the vegetation type over the Saharan region (11-33°N; 15°W-35°E) was set to shrub and the dust amount was set to 80% of the PI dust (Pausata et al., 2016). For iCESM, land conditions at 11°N were extended to the Sahara and Arabian peninsula, and Saharan dust was reduced through the use of a prognostic dust module (Tabor et al., 2020). For UofT-CCSM4, tropical vegetation was extended northwards and the Saharan region was replaced by a mix of shrubs, steppe and savanna, with different distributions across 25°N. In addition to vegetation changes, soil albedo was also reduced and the presence of five mid-Holocene megalakes was incorporated in the MH$_{GS}$ simulation (Chandan & Peltier, 2020). For GISS, arid shrub and grassland were prescribed over the Saharan region (Tiwari et al., 2023). For HadCM3, a 90% grass advance was prescribed over the Sahara. These vegetation changes are in accordance with proxy

reconstructions (Hély et al., 2014), and broadly align with PMIP4 recommendations for vegetation sensitivity experiments (Otto-Bliesner et al., 2017). The different MH$_{GS}$ simulations represent different pathways of achieving a comparable strengthening of the West African Monsoon as indicated by proxy records for the mid-Holocene Green Sahara.

4.2.2   ENSO metrics

We quantify Pacific mean state through zonal gradients. The West Pacific sea surface temperature (SST) gradient is used to quantify the zonal SST gradient (Hoell & Funk, 2013). It is defined as the difference between the mean SST over the West Pacific Ocean (0-10°N, 130-150°E) and central Pacific Ocean (5°S-5°N, 160°E-150°W; also known as the Niño-4 region). Values for the Trans-Niño index (Trenberth & Stepaniak, 2001) and the Eastern Pacific SST Gradient (J. R. Brown, Brierley, et al., 2020) were also calculated. The Equatorial Southern Oscillation Index was used to quantify the zonal gradient in sea level pressure (SLP). It is defined as the difference between the mean SLP over Indonesia (5°S-5°N, 90-140°E) and the eastern Pacific (5°S-5°N, 130°W-80°W). ENSO amplitude is estimated by SST variability, calculated through the standard deviation of boreal winter (DJF) SST anomalies (J. Brown et al., 2008). The SST anomalies were not detrended.

4.3   Results

4.3.1   Mean state changes

Our simulations suggest that the equatorial Pacific was characterized by a La Niña-like mean state during the MH (Figure 4-1). Both the MH$_{PMIP}$ and the MH$_{GS}$ multi-model mean SST anomalies indicate a cooling of 0.5 - 0.75 °C in the equatorial Pacific and in the present-day South Pacific Convergence Zone (SPCZ) during boreal winter. The cooling over the present-day SPCZ is accompanied by warming of about 0.5 °C to its southwest during boreal winter. Zonal SST gradients, which are typically higher during La Niña events than during El Niño events, were calculated using three indices. The West Pacific Gradient increases from PI through MH$_{PMIP}$ to MH$_{GS}$ for four out of five models (Supplementary Table S2). The exception to this increase is in the case of GISS, which shows an increase in zonal SST gradient from PI to MH$_{PMIP}$, but the lowest gradient occurs in the MH$_{GS}$ simulation. Other indices for the zonal SST gradient such as the Trans-Niño index and the Eastern Pacific Gradient did not show consistent trends among models. The Green Sahara also induced extensive drying (Figure 4-2) and easterly wind anomalies (Figure 4-3) over the

western and central equatorial Pacific. During boreal winter, the equatorial Pacific was characterized by negative precipitation anomalies of 0.5 mm/day (Figure 4-2). Notably, the present-day SPCZ region witnessed drying of more than 1.5 mm/day, with positive anomalies of up to 1.5 mm/day in the region southwest of it. Anomalous drying of more than 2 mm/day is observed over the central equatorial Pacific during boreal summer. Zonal wind strength anomalies indicate anomalous easterlies in the western and central equatorial Pacific extending to the present-day SPCZ and westerly anomalies to the southwest of the present-day SPCZ (Figure 4-3). The anomalous easterlies in the western and central equatorial Pacific during boreal summer lead to the La Niña-like mean state (discussed further below). Combined with the SST and precipitation anomalies particularly during winter, the zonal wind strength anomalies suggest a southwesterly shift in the SPCZ. Mean state changes are also evident in SLP anomalies. The Equatorial Southern Oscillation Index, which typically has positive values during La Niña events and negative values during El Niño events, increases consistently for all five models going from PI to MH_{PMIP} to MH_{GS} simulations (Supplementary Table S2). In summary, our simulations indicate two key mean state changes during the MH: a La Niña-like cooling and drying over the equatorial Pacific, and a southwesterly shift of the SPCZ. These changes are primarily orbitally-driven but are further amplified by the Green Sahara.

4.3.2 ENSO variability changes

The models in this study do not capture a strictly consistent response to the insolation changes (Figs. 4A-E, S4). EC-Earth, UofT-CCSM4 and HadCM3 show up to 30% reductions in SST variability in parts of the equatorial Pacific in the MH_{PMIP} simulations relative to the PI. iCESM shows small but varied anomalies in SST variability (-6% to +2%) in the equatorial Pacific, however, the reductions are not statistically significant. GISS shows a decrease in variability over the Niño1+2 region, but increases of 10-18% over the other index regions. On the other hand, all models show significant reductions in SST variability in the MH_{GS} simulations relative to the PI (Figure 4-4). These reductions are manifested in different parts of the equatorial Pacific in different models. For EC-Earth, the Green Sahara leads to the greatest reduction in SST variability in the western-central equatorial Pacific with a 0.1 °C decrease (31% decrease relative to the PI) over the Niño4 region. For the other models, the greatest reductions in SST variability occur in the central-eastern equatorial Pacific with decreases of 0.1-0.2 °C in the Niño3 region, which correspond to upto 17% reduction relative to the PI.

Notably, the MH_{GS} simulations show reduced SST variability relative to the PI in nearly all the Niño index regions (Figure B 6). The exception to this is GISS which shows an increase of 0.02 °C over the Niño3.4

region (Figure 4-4). However, this increase is not significant at the 95% confidence level, assessed using the Bartlett' test for equal variances. This small and exceptional increase in SST variability in the Niño3.4 region is not due to a contrary effect of the Green Sahara, but instead arises because of the exceptional insolation-driven increase shown by GISS. This increase is unique to GISS, with all others models showing an orbitally-driven decrease in SST variability in the Nino3.4 region. The large insolation-driven increase of about 0.4 °C is not entirely offset by the Green Sahara-driven decrease in SST variability (Figure 4-4). Thus, all models consistently show a reductive effect of the Green Sahara on equatorial Pacific SST variability, though this reduction is weaker in the case of HadCM3 due to substantial warm bias and inadequate representation of changes in the tropical Atlantic (discussed further below).

4.3.3   Changes over the equatorial Atlantic Ocean

The models in this study show several biases that limit their ability to capture interannual variability over the tropical Atlantic Ocean, especially during boreal summer. Comparisons between our PI simulations and observations show significant warm biases, a westward displacement of the Atlantic Cold Tongue and an underestimation of the zonal SST gradient (Annexe B). The warm bias is particularly noteworthy in the case of HadCM3 (Annexe B). In spite of substantial biases, the models show several consistent features in their MH simulations (Figure 4-5). During the MH, the intensified WAM was associated with intensified southwesterly winds during boreal summer (Figure 4-3) that brought moisture into the Saharan region (Figure 4-2). Close to the equator, all models show westerly wind anomalies which inhibit upwelling during boreal summer. Reduced upwelling is expected to lead to positive anomalies in SST, however, such anomalies appear only in EC-Earth and UofT-CCSM4 (Figure 4-5). In the other models, these anomalies are masked by cooling driven by insolation and greenhouse gas changes. However, all models indicate that the Green Sahara led to a warming of the equatorial Atlantic and the Benguela region, with the strongest signature in EC-Earth and the weakest signature in HadCM3. Two models (EC-Earth and iCESM) show a reduction in the zonal SST gradient during boreal summer from PI through MH_{PMIP} to MH_{GS}, consistent with Atlantic Niño-like conditions. The other models show no clear changes in the SST gradient between the three simulations, with the climate signal likely being overshadowed by the SST biases. Interannual variability over the equatorial Atlantic during boreal summer and fall shows a marked decrease during the MH in the models EC-Earth and iCESM. On the other hand, UofT-CCSM4 shows positive anomalies in interannual variability, while the other models do not show any clear signature. It is possible that GISS and HadCM3 show seasonally displaced Atlantic Niño signatures and associated MH-PI negative anomalies. Lastly, in addition to the Atlantic Niño-like conditions during boreal summer and fall, the Green Sahara

also leads to significant warming over the northern tropical Atlantic during February-April (contours in Figure 4-5). This warming is most pronounced in EC-Earth and weaker in GISS and HadCM3.

4.3.4   The Atlantic-Pacific teleconnection

The modulation of ENSO variability by the tropical Atlantic is effected due to changes in the Walker Circulation, which lead to anomalous divergence over the central Pacific. This divergence is reflected in negative precipitation anomalies during boreal summer (Figure 4-2) and leads to easterly wind anomalies over the western and central equatorial Pacific during boreal summer (Figure 4-3). These easterly wind anomalies may also be generated in part due to the anomalous warming over the northern tropical Atlantic during boreal spring (Figure 4-5), which can lead to an anticyclonic flow over the western Pacific. The easterly wind anomalies drive a shoaling of the thermocline during boreal summer, reflected in positive sea temperature anomalies between the 100-500 m in the western equatorial Pacific (Annexe B). These anomalies are up to 1.5°C in the MH_{PMIP} simulations and 2°C in the MH_{GS} simulations. The $MH_{GS} - MH_{PMIP}$ difference suggests that the Green Sahara alone induces sea temperature anomalies of up to 2°C during boreal winter in some regions of the western and central equatorial Pacific. In all MH simulations, the sea temperature anomalies propagate eastward during boreal fall and winter, accompanied by negative sea temperature anomalies in the order of $0.75 - 1$ °C in the eastern equatorial Pacific. The sea temperature anomalies are primarily driven by insolation changes and amplified by the Green Sahara.

4.4   Discussion and Conclusions

In this study, we use five global climate models to show that the mid-Holocene Green Sahara impacted ENSO mean state and variability. All models show a La Niña-like mean state during the MH and a reduction in ENSO variability due to the strengthening of the WAM. This reduction is independent of model physics or the specific vegetation and land surface changes incorporated to simulate the Green Sahara. Instead, it depends on and is constrained by the ability of climate models to adequately simulate the Atlantic Niño and its changes, which lead to alterations to the Walker Circulation. Thus, reducing biases in the tropical Atlantic may be key to simulating the Green Sahara – ENSO teleconnection. Our results are in agreement with a previous study using the model EC-Earth (Pausata, Zhang, et al., 2017b), and show that the modulation of ENSO by the Green Sahara is neither a model-specific result, nor is driven solely by the

choice of a specific vegetation distribution or dust reduction. Lastly, our work highlights the southwesterly shift in the SPCZ which was not identified previously.

Due to the incorporation of the Green Sahara, our MH simulations provide additional insight into the climate of the mid-Holocene over the PMIP3/4 model ensemble. The reduction in boreal winter SSTs in our MH$_{PMIP}$ and MH$_{GS}$ ensembles is slightly greater than that shown by the PMIP3/4 model ensemble. The PMIP3/4 model ensemble showed a small cooling of ~0.5 °C, restricted to the eastern part of the Pacific basin (J. R. Brown, Brierley, et al., 2020). Our MH$_{PMIP}$ and MH$_{GS}$ ensemble shows a slightly greater cooling of up to 0.75 °C in the same regions, with a cooling of ~0.5 °C extending over the entire equatorial Pacific as well as in the southeastern tropical Pacific. However, while the PMIP3/4 ensemble mean does not show warming over any region, a marked warming anomaly is present in a northwest-southeast oriented region in the southern tropical Pacific extending from the Maritime Continent to about 110°W. Together, the cooling anomaly over the southeastern Pacific and nearby warming to the southwest of it, represent a southwestward shift of the South Pacific Convergence Zone (SPCZ), similar to observations during La Niña events in the present day (J. R. Brown, Lengaigne, et al., 2020). This southwestward shift is also reflected in precipitation anomalies. Boreal winter precipitation response of the PMIP3/4 model ensemble shows a reduction in precipitation over the equatorial and southwestern Pacific, and an increase in precipitation over a northwest-southeast band contiguous and southwest of the region showing the drying anomaly (J. R. Brown, Brierley, et al., 2020). Thus, the PMIP3/4 model ensemble also captures the southwestward shift of the SPCZ. The drying and wettening anomalies are ~1 mm/day and ~0.5 mm/day, respectively, comparable to those shown by our MH$_{PMIP}$ ensemble. However, our MH$_{GS}$ ensemble shows greater drying and wettening anomalies in the order of ~1.5 mm/day and ~0.75 mm/day. Further, the meridional displacement of the SPCZ is greater than that suggested by the PMIP3/4 ensemble. Thus, vegetation changes act as a positive feedback as the effect of the Green Sahara is to amplify the insolation-driven southwestward shift of the SPCZ. Over the broader equatorial Pacific, our MH$_{GS}$ ensemble shows greater drying anomalies compared to our MH$_{PMIP}$ ensemble and the PMIP3/4 ensemble. A reduction in ENSO amplitude is also indicated through a reduction in the standard deviation of SSTs over the Niño 3.4 region. Compared to the PMIP3 and PMIP4 model ensemble estimates which indicate a ~7% and ~10% reductions in ENSO variability, our MH$_{PMIP}$ and MH$_{GS}$ model ensembles capture reductions of ~9% and ~13%. A reduction in variability is also simulated over nearly all El Niño index regions. Over the equatorial Pacific, the models capture some statistically significant differences in SST variability between the MH$_{PMIP}$ and PI simulations (reflecting the forced response to insolation changes), between the MH$_{GS}$ and PI simulations

(reflecting the forced response to all MH changes) as well as between the MH$_{GS}$ and MH$_{PMIP}$ simulations (reflecting the forced response due to the Green Saharan changes alone). Experiments with the GFDL Climate Model have shown that model simulations can show large, unforced internal variability on the multi-decadal and centennial timescales, which makes the identification of forced responses challenging (Wittenberg, 2009; Wittenberg et al., 2014); however, a first-order test of statistical difference (Bartlett's test for equal variances) that identifies differences in variances between simulations relative to their internal variabilities lends confidence to our conclusions.

Simulations using Green Sahara mid Holocene vegetation have greater agreement with proxy reconstructions than mid Holocene simulations that incorporate only modern vegetation (Figure 4-6). Proxy reconstructions from lake sediments (Barr et al., 2019; Conroy et al., 2008; Moy et al., 2002), marine sediments (Koutavas & Joanides, 2012; White et al., 2018), speleothems (Chen et al., 2016) and corals (Grothe et al., 2020; McGregor & Gagan, 2004) indicate a reduction in ENSO variability during the middle Holocene, from both core ENSO regions as well as ENSO teleconnection regions. A previous coral record from the central equatorial Pacific suggested that there was no notable reduction in ENSO variability during the mid-Holocene (Cobb et al., 2013), however, new work from the same sites has indicated otherwise (Grothe et al., 2020). While the ability of climate models to capture MH changes is qualitatively clear, quantitative estimations tend to be muted compared to those from proxy reconstructions. For instance, coral water isotopologue anomalies from the western and central equatorial Pacific suggested a 15% and 64% reduction in ENSO amplitude, respectively (Emile-Geay et al., 2016; McGregor & Gagan, 2004). In contrast, SST standard deviations over the Niño 3.4 region from PMIP3 and PMIP4 model ensemble suggest a 6.9% and 9.7% reduction in ENSO variability, respectively (J. R. Brown, Brierley, et al., 2020). As discussed above, the PMIP3/4 ensemble also underestimates SST and precipitation changes associated with the La Niña mean state and the displacement of the SPCZ. The inclusion of the Green Sahara leads to higher estimates of ENSO variability reductions, and more extensive mean state changes, reconciling many of the differences with proxy reconstructions.

The presence of an Atlantic Niño-like state in the tropical Atlantic is difficult to identify in the MH$_{PMIP}$ or the MH$_{GS}$ simulations due to model biases. Most models are unable to correctly simulate the observed equatorial Atlantic SST mean state, which results in a cold bias in the western equatorial Atlantic Ocean, a warm bias in the eastern equatorial Atlantic Ocean, and a westward displacement of the Atlantic Cold Tongue (Lübbecke et al., 2018; Richter & Xie, 2008). This affects the ability of the model to capture changes

to the MH mean state. Further, SST changes associated with the Atlantic Niño are also masked by the seasonal cooling observed during the MH, also observed in the PMIP4 multi-model ensemble (Brierley et al., 2020a). However, the MH_{GS} anomalies relative to the MH_{PMIP} simulation clearly indicate the effect of the Green Sahara in nudging the tropical Atlantic into an Atlantic Niño-like mean state. The alterations in the Walker Circulation led to a La Niña response, similar to mechanisms identified previously (Chikamoto et al., 2020; Rodríguez-Fonseca et al., 2009). The proposed mechanism is a shift in the Walker Circulation due to the occurrence of Atlantic Niño events, resulting in a strengthening of the ascending branch over the equatorial Atlantic and a strengthening of the descending branch over the equatorial Pacific. Increased surface convergence in the equatorial Atlantic is accompanied by increased surface divergence in the equatorial Pacific, the latter leading to reduced precipitation, easterly wind anomalies, and shoaling of the thermocline in the central and western equatorial Pacific during boreal summer. These anomalies are propagated to the eastern equatorial Pacific through Kelvin waves, resulting in La Niña events during the boreal winter. Previous studies (which did not explicitly consider the Green Saharan changes) have also investigated the possibility that the ENSO variance is governed by the annual cycle. A coral record from the central equatorial Pacific previously suggested that internal variability largely eclipsed any forced changes in ENSO during the Holocene, and reconstructions showing decreases in ENSO variability may simply have been recording changes in the annual cycle (Cobb et al., 2013). The said coral record has since then been updated with new oxygen isotope measurements which indicate a clearer reduction in variability between 5-3 ka (Grothe et al., 2020). However, it is noteworthy that modelling studies have so far elicited no clear answer. PMIP2/3 models have shown a positive (An & Choi, 2014) as well as a negative relationship between the annual cycle and ENSO variability, depending on the region considered. PMIP4 simulations that considered a range of time-slices suggested a weak positive correlation between the annual cycle and ENSO amplitude for the MH, but no clear relationship across experiments (Brown et al., 2020). Future work should focus on understanding the role of the annual cycle changes, ensuring a proper representation of the Green Sahara which affected temperature patterns across the tropical Pacific.

While our work is based on simulations for the MH (6,000 years BP), the teleconnection between northern Africa and ENSO would have operated during the entire Green Sahara Period of the Holocene (Pausata et al., 2020) as well as during the Green Sahara Periods of the pre-Holocene past (Kutzbach et al., 2020; Larrasoaña et al., 2013; Shi et al., 2024). This study is the first model intercomparison investigating the changes in ENSO associated with vegetation changes over northern Africa during the mid-Holocene. Our work adds to a growing body of literature that identifies the remote impacts of the Saharan vegetation

changes during the MH (Griffiths et al., 2020; Piao et al., 2020; Tabor et al., 2020). The importance of the MH Green Sahara and its remarkable influence on global climate arise from the fact that land surface feedbacks operated over a very large and uninterrupted landmass, acting to amplify the effects of solar forcings. Without the use of dynamical vegetation and land surface models, these feedbacks and their consequences on global climate are entirely neglected in climate model simulations that account only for insolation and greenhouse gas changes, prohibiting the identification of important teleconnections (Brierley et al., 2020b). Thus, future work focusing on Green Sahara Periods should ensure an appropriate representation of vegetation changes over northern Africa. Our work also highlights the equatorial Atlantic-to-Pacific teleconnection through an instance of WAM strengthening which is unmatched in the instrumental record. This shows that WAM strength plays an important role in modulating Atlantic Niño and La Niña events, deserving greater attention in ENSO forecasting. Lastly, our work is especially relevant in the context of geoengineering projects such as the Great Green Wall (Ingrosso & Pausata, 2024), which are planned to develop vegetation in the Sahel. While such initiatives may have global benefits through a potential reduction in ENSO variability, in addition to the local benefits over northern Africa, they may also have adverse local impacts in some specific regions such as eastern China, Papua New Guinea and other Pacific islands. More work is required to identify remote impacts of such vegetation changes on a regional and local scale.
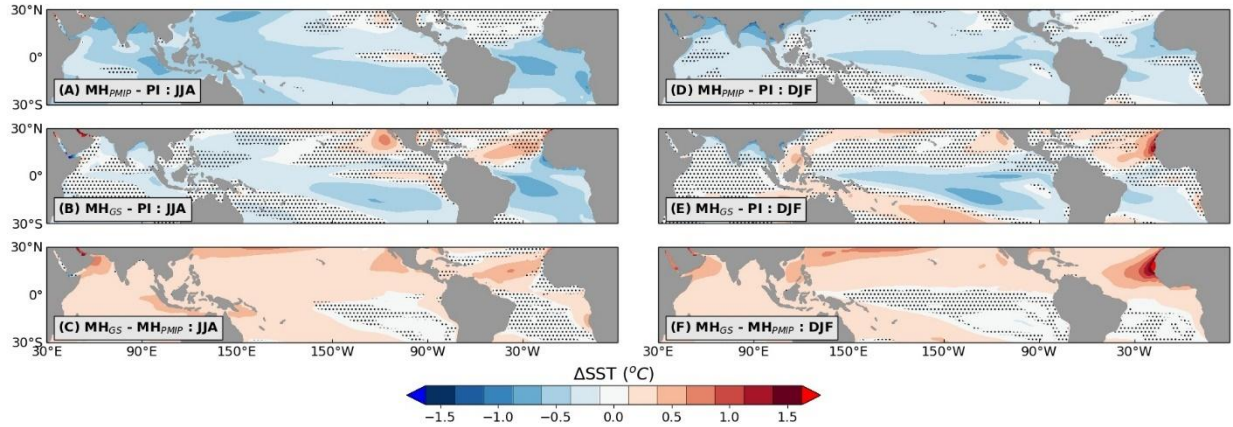
Figure 4-1 Multi-model mean changes in sea surface temperatures for the mid-Holocene. SST anomalies for boreal summer (A-C) and boreal winter (D-F) for MH_{PMIP} relative to PI (A, D), MH_{GS} relative to PI (B, E), and MH_{GS} relative to MH_{PMIP} (C, F) which reflect the effect of the Green Sahara alone. Un-stippled areas indicate at least 4 of 5 models agree on the sign of change, whereas stippling indicates model disagreement regarding sign of change.
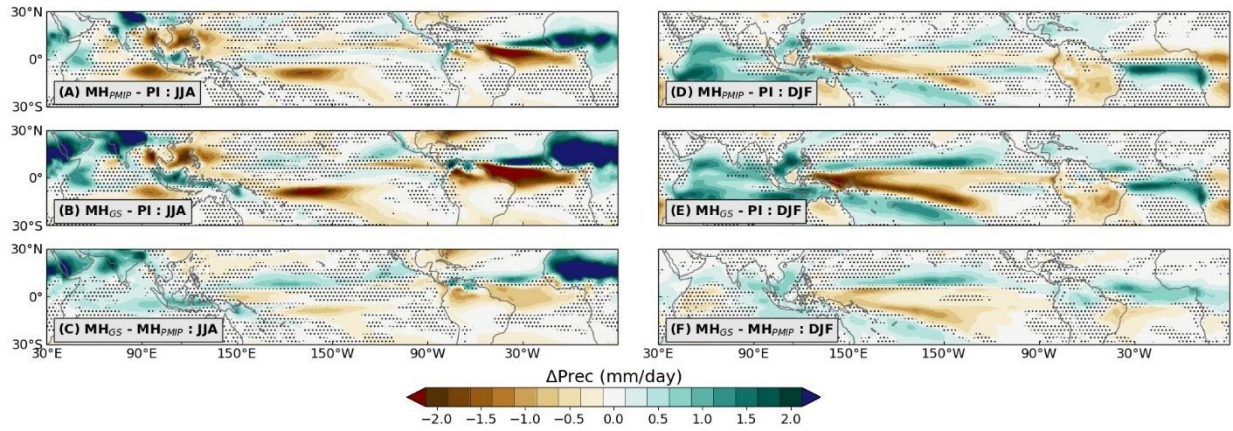
Figure 4-2 Multi-model mean changes in precipitation for the mid-Holocene. Precipitation anomalies for boreal summer (A-C) and boreal winter (D-F) for MH$_{PMIP}$ relative to PI (A, D), MH$_{GS}$ relative to PI (B, E), and MH$_{GS}$ relative to MH$_{PMIP}$ (C, F) which reflect the effect of the Green Sahara alone. Un-stippled areas indicate at least 4 of 5 models agree on the sign of change, whereas stippling indicates model disagreement regarding sign of change.
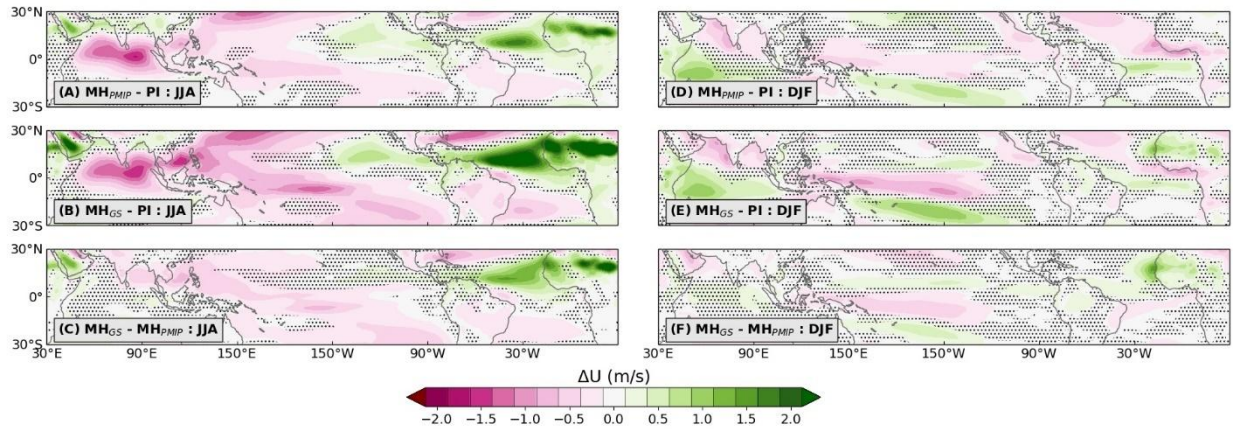
Figure 4-3 Multi-model mean changes in zonal wind strength at the surface for the mid-Holocene. Zonal surface wind strength anomalies for boreal summer (A-C) and boreal winter (D-F) for MH$_{PMIP}$ relative to PI (A, D), MH$_{GS}$ relative to PI (B, E), and MH$_{GS}$ relative to MH$_{PMIP}$ (C, F) which reflect the effect of the Green Sahara alone. Un-stippled areas indicate at least 4 of 5 models agree on the sign of change, whereas stippling indicates model disagreement regarding sign of change. Positive values indicate eastward (westerly) anomalies.
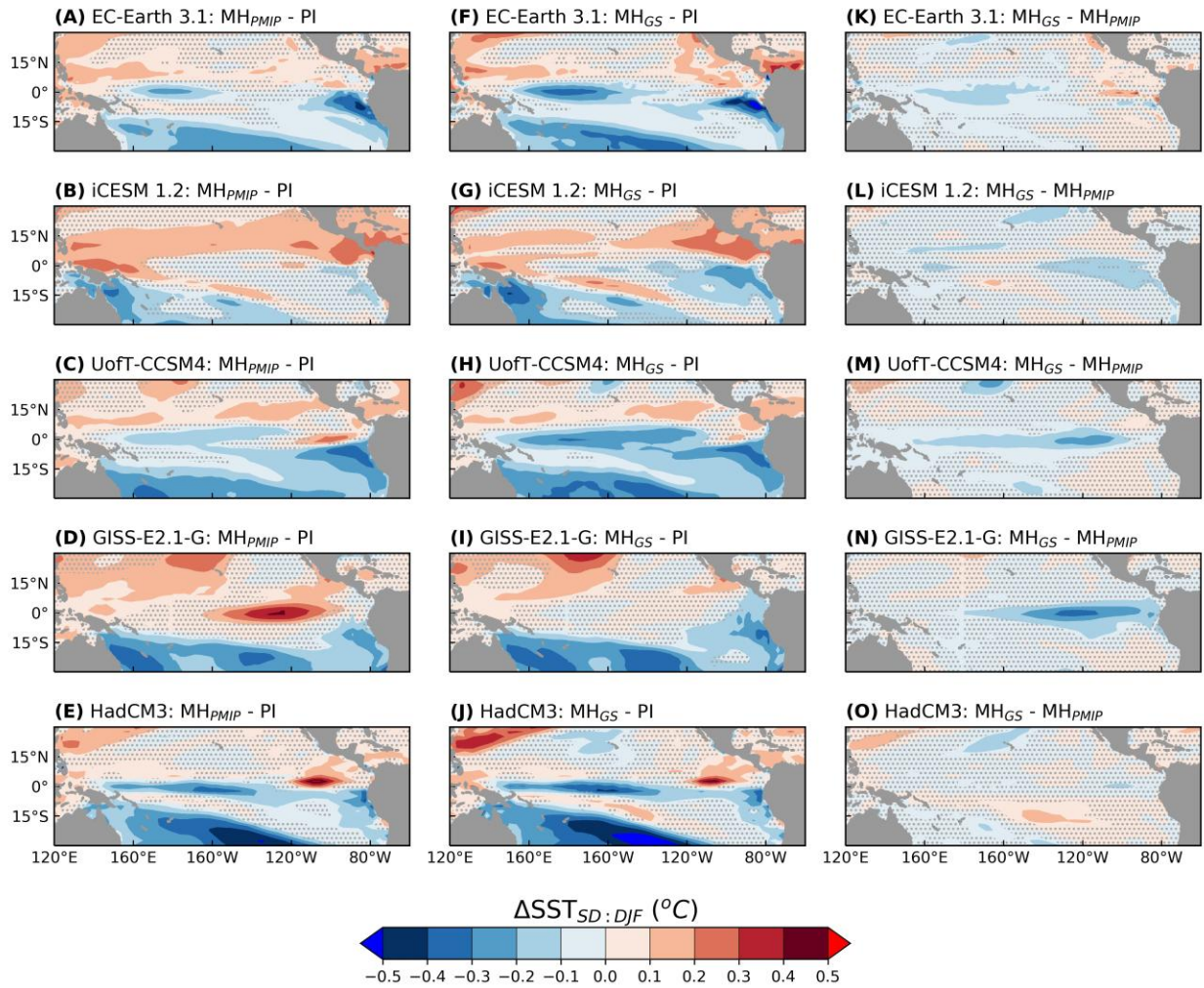
Figure 4-4 Changes in sea surface temperature variability. Anomalies in interannual SST variability over boreal winter for the MH$_{PMIP}$ (A-E) and the MH$_{GS}$ (F-J) simulations relative to the reference PI simulation and for the MH$_{GS}$ simulation relative to the MH$_{PMIP}$ simulation (K-O). Stippling indicates changes which are not significant at the 95% confidence level, evaluated using the Bartlett's test for equal variances.
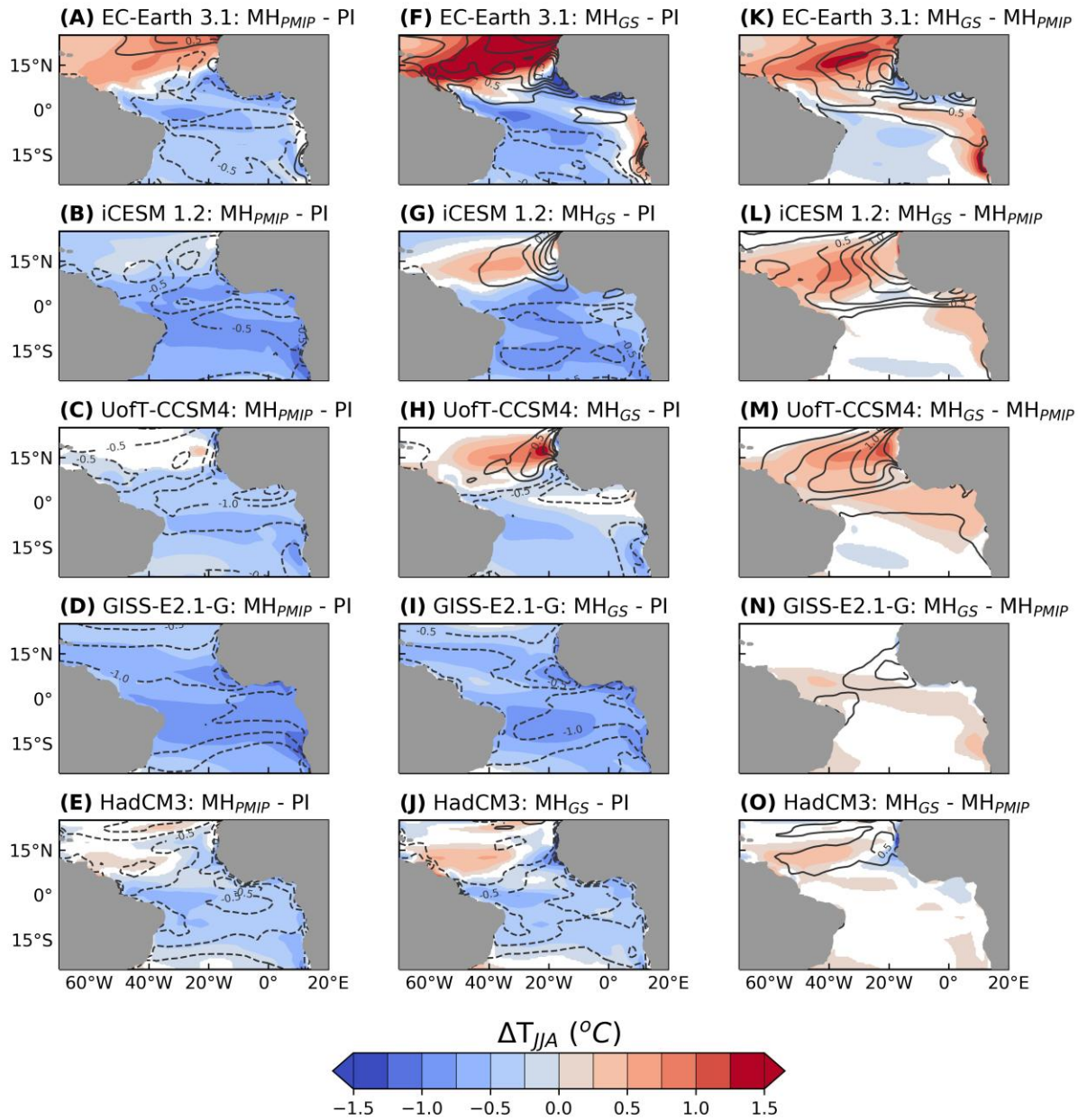
Figure 4-5 Changes in sea surface temperatures over the Atlantic. Colors show SST anomalies over boreal summer (JJA) and contours show SST anomalies over February-April (FMA) for the MH$_{PMIP}$ (A-E) and the MH$_{GS}$ (F-J) simulations relative to the reference PI simulation and for the MH$_{GS}$ simulation relative to the MH$_{PMIP}$ simulation (K-O). Contours are spaced at 0.25 °C. Only anomalies which are significant at the 95% confidence level are shown.
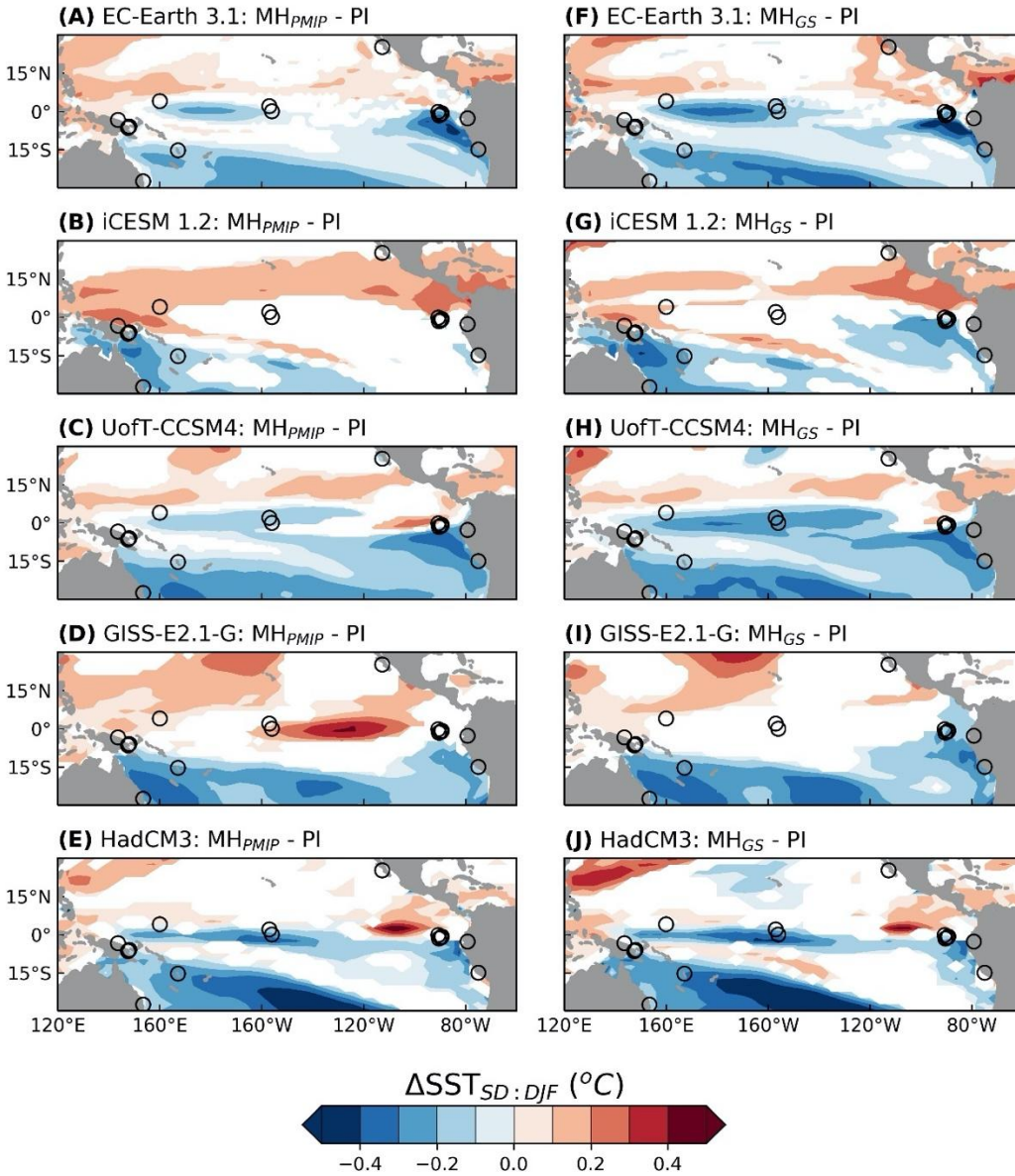
Figure 4-6 Changes in sea surface temperature variability. Anomalies in interannual SST variability over boreal winter for the MH$_{PMIP}$ (A-E) and the MH$_{GS}$ (F-J) simulations relative to the reference PI simulation. Only changes which are significant at the 95% confidence level are shown, evaluated using the Bartlett's test for equal variances. Overlain circles show sites of paleoclimatic records which show a reduction in ENSO variability during the Green Sahara Period. For details about the records, please refer to Table 5 provided in Annexe B.

CHAPITRE 5

Enhanced West African Monsoon amplified Arctic warming during the Green Sahara Period

S. Tiwari[1], F. S. R. Pausata[1], A. de Vernal[1], H. Beltrami[2], A. N. LeGrande[3,4], M. L. Griffiths[5]

[1]Department of Earth and Atmospheric Sciences, University of Quebec in Montreal, Montreal, Canada.

[2]Department of Earth Sciences, St. Francis Xavier University, Antigonish, Nova Scotia, Canada.

[3]NASA Goddard Institute for Space Studies, New York, New York, USA.

[4]Center for Climate Systems Research, Columbia University, New York, New York, USA.

[5]Department of Environmental Science, William Paterson University, Wayne, New Jersey, USA.

Supplementary Information for this article is provided in Annexe C.

Abstract

Northern Africa witnessed substantial vegetation and land surface changes between 11,000-5,000 years ago, referred to as the Green Sahara. Several paleoclimate reconstructions from the Arctic indicate concurrent anomalous warmth during this period, with some records indicating an abrupt cooling coinciding with the Saharan desertification. This has prompted studies into a potential teleconnection between the Green Sahara and the Arctic, leading to conflicting hypotheses regarding the dominant direction and mechanism for this teleconnection. In this study, we use simulations for the mid-Holocene (6,000 years ago) from five fully coupled global climate models to identify the impact of the Green Sahara on the Arctic region. Through the difference of two sets of simulations – with and without the Green Sahara – we show simulations incorporating the Green Sahara yield considerably higher Arctic warming relative to simulations without explicit prescriptions of vegetation changes. We also conducted simulations with an atmosphere-only global climate model to isolate the potential impact of Arctic temperature changes on northern African rainfall. Our findings reveal that the simulated changes in Arctic temperatures induced only weak atmospheric changes over northern Africa, which would not substantially contribute to Saharan desertification as previously suggested.

Résumé

L'Afrique du Nord a connu des changements substantiels de la végétation et de la surface terrestre entre 11 000 et 5 000 ans avant notre ère, appelés Sahara vert. Plusieurs reconstitutions paléoclimatiques de l'Arctique indiquent une chaleur anormale simultanée au cours de cette période, avec certains enregistrements indiquant un refroidissement brutal coïncidant avec la désertification du Sahara. Cela a donné lieu à des études sur une téléconnexion potentielle entre le Sahara vert et l'Arctique, conduisant à des hypothèses contradictoires concernant la direction et le mécanisme dominants de cette téléconnexion. Dans cette étude, nous utilisons des simulations pour l'Holocène moyen (il y a 6 000 ans) à partir de cinq modèles climatiques mondiaux entièrement couplés pour identifier l'impact du Sahara vert sur la région arctique. Grâce à la différence de deux séries de simulations – avec et sans le Sahara vert – nous montrons que les simulations intégrant le Sahara vert produisent un réchauffement de l'Arctique considérablement plus élevé par rapport aux simulations sans prescriptions explicites de changements de végétation. Nous avons également effectué des simulations avec un modèle climatique mondial basé uniquement sur l'atmosphère pour isoler l'impact potentiel des changements de température de l'Arctique sur les précipitations en Afrique du Nord. Nos résultats révèlent que les changements simulés des températures de l'Arctique n'ont induit que de faibles changements atmosphériques en Afrique du Nord, qui ne contribueraient pas de manière substantielle à la désertification du Sahara comme suggéré précédemment.

5.1   Introduction

Paleoclimate studies offer opportunities to investigate climate dynamics and variability beyond the limited scope of the instrumental record. The mid-Holocene (MH; 6000 years ago i.e. 6 ka before present or BP) is a key time slice for paleoclimate studies. The MH was characterized by a different orbital configuration than the present, with increased insolation in the Northern Hemisphere during boreal summer and reduced insolation during boreal winter, leading to greater seasonality relative to the present day (Otto-Bliesner et al., 2017). The increased Northern Hemisphere summer and fall insolation led to a strengthening of the monsoons (Sun et al., 2019), including the West African Monsoon (WAM) which governs the hydroclimate of northern Africa (Nicholson, 2009; Thorncroft et al., 2011). The stronger WAM and the increased precipitation resulted in a northward expansion of equatorial rainforests and the development of shrub and savannah vegetation in the present-day Saharan desert (Hély et al., 2014; Watrin et al., 2009). These vegetation and land surface conditions characterizing northern Africa during the MH have been termed the "Green Sahara". The Green Sahara Period occurred during the early and middle Holocene (~11 − 5 ka BP) due to the amplification of the insolation changes by positive climate feedbacks (Pausata et al., 2020). Evidence for the MH Green Sahara is available from a diverse array of paleoclimatic archives (Bartlein et al., 2011; deMenocal et al., 2000; Gasse, 2002; Lézine et al., 2011; Sha et al., 2019; Tierney, Pausata, et al., 2017). A compilation of 96 proxy reconstructions from northern Africa indicated that the termination of the Green Sahara Period occurred in a time-transgressive manner (Shanahan et al., 2015); while southern sites (southward of 15° N) show termination at around 2.5 − 4 ka BP, sites northward of the present-day WAM belt (i.e. northward of 15° N) record Saharan desertification between 5 − 6 ka BP.

In concert with a wetter-than-present northern Africa, some proxy reconstructions suggest that the MH climate was also characterized by a warmer-than-present Arctic. For instance, an alkenone record from the Norwegian Sea points to a climatic optimum between 8.5 − 5.5 ka BP (Calvo et al., 2002), which aligns with a nearby foraminiferal record indicating the optimum period between 10 − 5 ka BP (Kandiano & Bauch, 2002). Furthermore, pollen and dinoflagellate cyst records from the subpolar North Atlantic and southern Greenland margins show relatively high summer temperatures during the MH (Fréchette & De Vernal, 2009). Dinoflagellate cyst-based reconstructions of sea-ice concentrations (SIC) and summer sea surface temperatures (SSTs) show MH conditions warmer than the pre-industrial in the Fram Strait (Falardeau et al., 2018), the Baffin Bay and the Labrador Sea (Gibb et al., 2015; De Vernal et al., 2013) as well as in the central Arctic near the Laptev Sea shelf (De Vernal et al., 2020). A compilation of 66 glacier and ice cap-fed

lake records across the circumpolar Arctic also reveals that 90% of the records indicate warming between 7.1 – 5.7 ka BP, with glacier regrowth signaling cooling after ~6 ka BP (Larocca & Axford, 2022). The warming over the Arctic regions has been attributed to the insolation forcing, ice-sheet retreat, high latitude vegetation changes and associated feedbacks (O'Ishi & Abe-Ouchi, 2011). However, most modelling studies that incorporate these forcings do not show a Holocene Thermal Maximum or Arctic warming comparable to the proxy reconstructions (D. S. Kaufman & Broadman, 2023). Further, several proxy records show a cooling over the Arctic between ~6 – 5 ka BP (Calvo et al., 2002; England et al., 2008; Fréchette & De Vernal, 2009; Kandiano & Bauch, 2002; Larocca & Axford, 2022), coinciding with the Saharan desertification. The cooling over these Arctic regions occurred after a substantial lag of several millennia from peak insolation at high latitudes as well as any major changes to ice-sheet volumes (Patton et al., 2017; Ullman et al., 2016), and hence cannot be explained by said forcings.

The concurrent desertification of northern Africa around 5 ka BP and onset of Arctic cooling has prompted studies on a potential Saharan-Arctic teleconnection. However, there is no consensus yet on the predominant direction of this teleconnection during the MH. For example, simulations using LOVECLIM, an Earth model of intermediate complexity, indicated that 17-40% of the Arctic cooling over the course of the Holocene was caused by the Saharan desertification, suggesting that Arctic climate was influenced by low-latitude changes (Davies et al., 2015). The mechanism proposed in this study links the desertification of the Green Sahara with an increase in surface pressure over the Sahara, which weakened the mid-latitude westerlies and polar easterlies, leading to a reduction in heat transport from the tropics to the Arctic. These conclusions were supported by experiments with the fully coupled model EC-Earth version 3.1, wherein idealized simulations of "Green Sahara" and "Desert Sahara" indicated lesser poleward heat transport following the Saharan desertification, through both atmospheric and oceanic mechanisms (Muschitiello et al., 2015). Specifically, their results showed that a weaker atmospheric tropical-to-subtropical temperature gradient led to weakened atmospheric baroclinicity and reduced eddy activity. Meanwhile, in the ocean, the Saharan desertification led to reduced intensity of the Atlantic Meridional Overturning Circulation (AMOC). By contrast, another study using the fully coupled Community Climate System Model (CCSM) version 3 indicated that high-latitude cooling led to a reduction in the meridional gradient of upper tropospheric temperatures between the Sahara and the equator (Collins et al., 2017). A result of this was a weakened Tropical Easterly Jet (TEJ), reduced upper-level divergence and strengthened African Easterly Jet (AEJ), which further drove a reduction in upward vertical motion and consequent convective precipitation over the Sahara. Thus, previous studies have proposed mechanisms, but they did

not definitively establish cause-and-effect roles in the Saharan-Arctic teleconnection during the MH. This is because they relied on simulations with coupled climate models that do not allow pinpointing the direction of this teleconnection unequivocally.

Establishing the operative direction of the Saharan-Arctic teleconnection is key to identifying an important source of remote effects of regional climate changes during the MH, with potential insights into climate dynamics for the present and future climate. For example, recent Arctic climate changes have been proposed to presently exert a remote influence on the climate of the mid-latitudes (Cohen et al., 2014; Francis & Vavrus, 2012), with similar mechanisms potentially operating during the MH (Routson et al., 2019). Thus, the possibility that Arctic cooling contributed to Saharan desertification merits further investigation (Collins et al., 2017), as it could help evaluate the potential influence of ongoing Arctic Amplification on the lower latitudes. On the other hand, vegetation changes over northern Africa had an impact on global climate, such that incorporating them may help reconcile the Holocene Temperature Conundrum – i.e. reduce the proxy-model differences with respect to Northern Hemisphere temperature changes during the Holocene (Thompson et al., 2022). Thus, isolating the remote impact of the MH Green Sahara could help contextualize the recent temperature changes relative to the Holocene climate. In this study, we focus on two key questions: (i) Did the MH Green Sahara lead to greater Arctic warming? and (ii) Did Arctic cooling lead to or amplify Saharan desertification? To help answer these questions, we compare results from five fully coupled global climate models, using simulations run with (MH_{GS}) and without (MH_{PMIP}) the MH Green Sahara that conform to the PMIP protocols for orbital and greenhouse gas changes (Otto-Bliesner et al., 2017; Taylor et al., 2012; for further details, see Methods). The coupled models used here include EC-Earth version 3.1, isotope-enabled Community Earth System Model (iCESM) version 1.2, University of Toronto version of the Community Climate System Model version 4 (UofT-CCSM4), Goddard Institute of Space Studies model version E2.1-G (GISS-E2.1-G) and Hadley Centre Coupled Model version 3 (HadCM3). Results from all coupled models show an increase in Arctic temperatures with the incorporation of the MH Green Sahara, irrespective of the specific vegetation and land surface changes prescribed over northern Africa. To constrain the direction of this teleconnection pattern, we also ran a suite of experiments with an atmosphere-only global climate model – the Global Environmental Multiscale (GEM) model – wherein we make changes to the Sahara and the Arctic in turn. The GEM experiments are driven using sea surface temperature and sea ice concentration outputs from two simulations with EC-Earth with and without the Green Sahara (Methods, Figure C 1). Our results suggest that Arctic climate

changes did not have a substantial influence on the Green Sahara, indicating that the dominant remote influence extended from the Green Sahara towards the Arctic and not vice versa.

5.2   Methods

5.2.1   Simulations with fully coupled global climate models

We simulated the MH climate using five fully coupled global climate models – EC-Earth version 3.1 (Hazeleger et al., 2010), isotope-enabled Community Earth System Model version 1.2 or iCESM 1.2 (Brady et al., 2019), University of Toronto version of CCSM4, hereafter referred to as UofT-CCSM4, (Peltier & Vettoretti, 2014), GISS-E2.1-G (Kelley et al., 2020) and Hadley Centre Coupled Model version 3 (Valdes et al., 2017). Two sets of MH simulations were considered for each model – MH_{PMIP} and MH_{GS}. The MH_{PMIP} simulations incorporate changes to orbital forcing and GHG concentrations, following PMIP protocols. We note that in our model ensemble, EC-Earth simulations were conducted following the PMIP3 protocol (Taylor et al., 2012), while simulations with the other four models were conducted following the PMIP4 protocol (B. Otto-Bliesner et al., 2017). The PMIP4 protocol had lower GHGs than the PMIP3 protocol, which resulted in a slightly warmer MH climate in EC-Earth relative to the other three models. In addition to the PMIP recommendations for orbital and GHG forcings, the MH_{GS} simulations additionally incorporated the Green Sahara through different pathways. For EC-Earth, vegetation over the Sahara was set to shrub, and dust was reduced by 80% relative to the pre-industrial (Pausata et al., 2016). For iCESM, Sahelian land surface and vegetation characteristics were imposed over the Sahara, and dust mobilization decreased due to the use of an interactive dust scheme (Tabor et al., 2020a). For UofT-CCSM4, tropical rainforests were extended northwards, and the Sahara was replaced by a mix of shrub, steppe and savanna (Chandan & Peltier, 2020). Further, soil albedo was reduced and the presence of five MH mega lakes was incorporated. For GISS, the Sahara was replaced by arid shrub or grassland (Tiwari et al., 2023). For HadCM3, a 90% grass advance was prescribed over the Sahara.

5.2.2   Simulations with atmosphere-only global climate model

We conducted several experiments with the Global Environmental Model (GEM) version 4.8.12, developed by Environment Canada and Climate Canada (Girard et al., 2014). Three boundary conditions were changed: (a) vegetation over northern Africa, (b) dust, and (c) sea-surface temperatures (SST) and sea-ice concentrations (SIC). The Green Sahara was simulated by prescribing evergreen broadleaf shrubs over the present-day Saharan region and prescribing an 80% dust reduction for the MH relative to the PI. We used SST and SIC conditions from monthly outputs from two simulations using the fully coupled global climate

model EC-Earth version 3.1 (Pausata et al., 2016). In the EC-Earth simulations, the inclusion of the Green Sahara (their MH$_{GS-RD}$ simulation) led to warmer SSTs over most of the Northern Hemisphere, relative to the control run that incorporated orbital and GHG changes only (their MH$_{CNTRL}$ simulation). Hence, we use "warm" and "cool" SSTs and SIC outputs from their MH$_{GS-RD}$ and MH$_{CNTRL}$ runs respectively to drive our GEM experiments (Figure C 1). Note that the two sets of SST and SIC driving data are warmer or cooler relative to each other, not with respect to the PI or present-day climate. We also ran two experiments to study the effect of Arctic climate changes over the Green Sahara: MH$_{WA+DS}$ (Warm Arctic + Desert Sahara) and MH$_{CA+GS}$ (Cold Arctic + Green Sahara). For the MH$_{WA+DS}$ experiment, we prescribed warm SST and SIC conditions over the Arctic, with no Green Saharan changes over northern Africa. For the MH$_{CA+GS}$ experiment, we prescribed a Green Sahara, but with cool SST and SIC conditions over the Arctic. In both the MH$_{WA+DS}$ and MH$_{CA+GS}$ experiments, the SST and SIC changes over the Arctic ($> 60°$ N) were smoothened towards the lower latitudes between $55° - 60°$ N.

5.2.3   Comparison with proxy reconstructions

We compared model simulated temperatures with proxy reconstructions from the Temp12k dataset (D. Kaufman et al., 2020). We quantified proxy-model agreement through two metrics: Cohen's Kappa index (κ) and Root Mean Square Error (RMSE). κ quantifies agreement between two datasets for categorical data (i.e. across categories such as "warmer" or "colder"). It is a unitless metric that ranges from 0 (complete disagreement) to 1 (complete agreement), and incorporates the possibilities of agreement occurring due to random chance. RMSE indicates the difference in model results and proxy estimates, and was calculated as the mean of the absolute differences between a proxy estimate and the modelled temperature at the nearest grid cell.

5.3   Results

5.3.1   Impact of MH Green Sahara on Arctic and global warming

To understand the effect of the Green Saharan changes on Arctic temperatures, we assessed MH anomalies in mean annual temperature (MAT) relative to the PI. MH$_{PMIP}$ anomalies relative to PI indicate an increase in MAT averages over the Arctic region for four models (Figures 4-1, 4-2 and 4-3). The exception is GISS which shows a statistically insignificant decrease over the Arctic region. The MH$_{PMIP}$ - PI anomalies range from -0.03 °C for GISS to 2.32 °C for EC-Earth. All models show positive MAT anomalies in the MH$_{GS}$

experiments, which are larger than the anomalies observed in the MH$_{PMIP}$ experiments. MH$_{GS}$ − PI anomalies range from 0.37 °C for GISS to 3.38 °C for EC-Earth. All models show a consistent warming effect of the Green Sahara in the northern Atlantic, Greenland Sea, Norwegian Sea, Fennoscandia and the Barents Sea, estimated through MH$_{GS}$ − MH$_{PMIP}$ anomalies (Figure 4-3). The largest warming is induced over the Barents Sea, with the highest values shown in EC-Earth (4 °C), followed by UofT-CCSM4 and HadCM3 (3 °C).

The inclusion of Green Saharan changes leads to an increase in the Global Mean Surface Temperatures (GMST) in all models (not shown). Four out of five MH$_{PMIP}$ experiments showed negative GMST anomalies relative to the PI, ranging from -0.46 °C for GISS to -0.1 °C for HadCM3, while EC-Earth showed a positive GMST anomaly of 0.38 °C. On the other hand, in the case of MH$_{GS}$ experiments, four out of five models showed positive GMST anomalies relative to the PI, ranging from 0.04 °C for HadCM3 to 0.84 °C for EC-Earth, with GISS showing a negative GMST anomaly of -0.3 °C. In all models, the Green Saharan changes add a warm anomaly to the GMST, ranging from 0.14 °C for HadCM3 to 0.47 °C for UofT-CCSM4. The increases in GMST are largely driven by warming over the Arctic, where the Green Sahara alone adds a warm anomaly of 0.41 °C − 1.05 °C. The inclusion of the Green Sahara also leads to warming in the mid-latitudes. In the case of MH$_{PMIP}$ experiments, three out of five models (except EC-Earth) show negative anomalies over the mid-latitudes. On the other hand, in the case of MH$_{GS}$ experiments, four out of five models (except GISS) show positive anomalies over the same region. Lastly, warming over the Saharan region contributes substantially to GMST changes. In three out of five models, the Green Sahara leads to warming of up to 6 °C in the Saharan region. GISS and HadCM3 show no warming over northern Africa, and consequently show the lowest GMST changes induced by the Green Sahara. MH$_{GS}$ experiments show an overall warming of the Northern Hemisphere relative to the PI in four models (except GISS), but the signature of the Southern Hemisphere remains mixed.

Anomalies in mean annual sea level pressure for MH experiments relative to the PI indicate that the Green Sahara leads to a decrease in pressure over the Arctic and an increase in pressure over parts of the North Atlantic in all four models (Figure 5-4). While the response in the MH$_{PMIP}$ experiments is mixed, all models show a decrease in pressure over the Arctic in the MH$_{GS}$ experiments with an accompanying increase over the western subtropical North Atlantic, suggesting a positive phase of the Arctic Oscillation. Over northern Africa, a decrease in pressure indicates a strengthening of the Saharan Heat Low, consistent with the increase in temperature.

5.3.2   Model-proxy comparison

The Temp12k compilation of proxy reconstructions (D. Kaufman et al., 2020) includes 61 records that reflect changes in annual mean temperatures over the Arctic. Out of these, 47 show warm conditions during the MH while the remaining 14 show cooler than present temperatures (Figure 5-3). Out of 69 records of summer temperatures, 43 indicate warmer conditions, 25 indicate cooler conditions, and 1 record shows no change. Similarly, out of 28 records of winter temperatures, 20 indicate warmer MH winters, while 8 indicate cooler MH winters. Thus, Arctic warmth during the MH does not appear to have been consistent across the region on an annual or seasonal basis. A dominantly warm signature around 6 ka surfaced only over Baffin Bay, around Greenland, Fennoscandia and southern Alaska. On regional scales, there are differences in proxy reconstructions over Iceland, Beaufort and Chukchi Seas and in the Arctic around northern Greenland towards the Laptev Sea, pointing to the regionalism and complexity of processes in the Arctic realm. Over Iceland, the melting of ice cap records indicates warmth during the Holocene, with recovery and expansion recorded at ~5.5 ka BP (Larsen et al., 2012), whereas over Greenland the minimum ice volume was achieved between 5 and 3 ka BP (Larsen et al. 2015; Briner et al. 2016). Marine sediment cores from the North Icelandic Shelf, as well as the southern Greenland margins and the Norwegian Sea, show a general decline in surface temperature from the early to late Holocene (Calvo et al., 2002; Kandiano & Bauch, 2002; Bendle & Rosell-Melé, 2007; Solignac et al., 2006; Gibb et al., 2015; Falardeau et al., 2018).

Regardless of the complexity of the temperature changes in the Arctic, the inclusion of the Green Sahara leads to an increase in values for the Cohen's Kappa index (κ), which measures agreement among two datasets regarding categorical data (such as "warmer" or "cooler" climate). κ increases for four out of five models (iCESM, UofT-CCSM4, GISS and HadCM3), with increases of up to 0.27 and does not change for EC-Earth. These increases are primarily due to an expansion of area showing positive temperature anomalies, particularly in Fennoscandia, leading to improved qualitative agreement between proxy records and model results. EC-Earth shows no change in κ because the warming pattern is already strong in the MH_{PMIP} experiment across the Arctic, and the categorical differences (change in sign) between the MH_{PMIP} and MH_{GS} simulations largely occur in areas with no coverage of the proxy dataset. Root mean square error changes ($\Delta RMSE$) in mean annual temperatures, which provides an indication of the absolute differences in proxy and model estimates, show less coherence in quantitative terms. RMSE increases from MH_{PMIP} to

MH$_{GS}$ in the case of EC-Earth (ΔRMSE = 0.025), iCESM (ΔRMSE = 0.34) and HadCM3 (ΔRMSE = 0.122), whereas it decreases in the case of UofT-CCSM4 (ΔRMSE = -0.218) and GISS (ΔRMSE = -0.264). This indicates that while the inclusion of the Green Sahara improves the spatial extent of positive anomalies in EC-Earth, iCESM and HadCM3, it also leads to an over-estimation of temperatures. It is important to note that these results depend on the proxy reconstructions included, and are impacted by the fidelity of various proxies to recording mean annual surface temperatures (Andersson et al., 2010).

5.3.3 Impact of Arctic SST and SIC changes on Saharan climate

To determine whether concurrent changes in Saharan and Arctic climate were driven by a remote impact exerted by the Arctic on the Sahara, we conducted experiments using the atmosphere-only GEM model and isolated the impact of Arctic temperature changes on the Saharan precipitation and atmospheric circulation (Methods, Figure C 1). The MH$_{PMIP}$ and MH$_{GS}$ experiments were driven by the SST and SIC conditions simulated by previously run MH$_{PMIP}$ and MH$_{GS}$ experiments with EC-Earth. The MH$_{WA+DS}$ (Warm Arctic + Desert Sahara) experiment was driven by relatively warm conditions over the Arctic as simulated by the EC-Earth MH$_{GS}$ experiment, and relatively cool conditions over the rest of the world as simulated by the EC-Earth MH$_{PMIP}$ experiment. Conversely, the MH$_{CA+GS}$ (Cold Arctic + Green Sahara) experiment was driven by relatively cool conditions over the Arctic as simulated by the EC-Earth MH$_{PMIP}$ experiment, and relatively warm conditions over the rest of the world as simulated by the EC-Earth MH$_{GS}$ experiment.

The inclusion of the warmer SST and reduced SIC conditions over the Arctic leads to positive precipitation anomalies of up to 0.4 mm/day during boreal summer over small regions between 10-15 °N (Figure 5-5). Elsewhere, the inclusion of the warmer Arctic yields no statistically significant anomalies in precipitation over most of northern Africa in the MH$_{WA+DS}$ experiment relative to the MH$_{PMIP}$ experiment. Over the Sahara, precipitation anomalies (less than 0.1 mm/day) are not comparable to the anomalies resulting from the inclusion of the Green Saharan changes (>2 mm/day, Figure C 2). Thus, our results suggest that a warming over the Arctic, as prescribed here, did not lead to a positive feedback effect in the strengthening of the WAM. Similarly, the MH$_{CA+GS}$ experiment also shows statistically significant changes in precipitation relative to the MH$_{GS}$ experiment over limited regions in northern Africa (Figure 5-5). Negative anomalies of about 0.5 mm/day emerge over small regions northward of 12 °N, with positive anomalies of up to 0.4 mm/day over small regions southward of 12 °N. Overall, precipitation anomalies due to the inclusion of the cooler Arctic are too small to suggest that the Arctic could have drastically reduced WAM precipitation.

These observations are consistent with changes to the zonal wind strength, which reflect changes to the regional atmospheric jets. The MH$_{WA+DS}$ experiment shows a weakening of the upper-level (~150 hPa) Tropical Easterly Jet relative to the MH$_{PMIP}$ experiment (Figure 5-5). This is in contrast to the clear and significant intensification of the African Westerly Jet, northward shift of the African Easterly Jet and intensification of the Tropical Easterly Jet shown by all models considered in this study, upon the inclusion of the Green Sahara (Figure C 3). In contract, the MH$_{CA+GS}$ experiment shows a weakening of the low-level (850 hPa) African Westerly Jet relative to the MH$_{GS}$ experiment, which is consistent with a weakening of the WAM.

5.4   Discussion

The possibility of an MH Saharan – Arctic teleconnection has been previously suggested on the basis of concurrent climatic changes between the two regions (Collins et al., 2017; Davies et al., 2015; Muschitiello et al., 2015) and the remote impacts exerted by these regions during the MH (Routson et al., 2019; Zhang et al., 2021) or the present day (Cohen et al., 2014; Francis & Vavrus, 2012; Gaetani et al., 2011). In this study, we investigated the existence and the dominant direction (if any) of this teleconnection. Based on consistent responses simulated by five fully coupled global climate models, as well as targeted experiments using an atmosphere-only global climate model, we conclude that changes in the Arctic climate had a limited impact on the Green Sahara. Previous work using the CCSM3 model suggested that the Arctic cooling at about 5.5 ka BP led to the Saharan desertification (Collins et al., 2017). This study was based on a simulation for the Early Holocene (8.5 ka BP) with no explicit vegetation changes, and used a freshwater perturbation to simulate the high latitude cooling. Our experiments with GEM use targeted experiments for the MH with and without Green Saharan changes, and do not support a central role of the Arctic climate changes in the Saharan desertification. Furthermore, previous compilations of proxy reconstructions have indicated that the warming over the Arctic during the middle Holocene was not spatially homogenous (Cartapanis et al., 2022), nor was the Arctic cooling during the middle-late Holocene synchronous (McKay et al., 2018). Thus, it appears improbable that the Arctic cooling could have induced the Saharan desertification.

On the other hand, the greening of the Sahara favored a warming in the Atlantic-influenced sector of the Arctic through increased heat transport from the low to the high latitudes. The MH Green Saharan changes

lead to regional anomalies in mean annual temperatures of 2-3 °C in northwest Africa and 3-6 °C in northeast Africa. These anomalies are consistent with results from previous studies that incorporated such changes (Davies et al., 2015; Gaetani et al., 2024; Muschitiello et al., 2015; Zhang et al., 2021) but are considerably higher than results from the PMIP3 or PMIP4 model ensemble (C. M. Brierley et al., 2020a) which show large-scale cooling over northern Africa during the MH due to the absence of vegetation changes. The temperature changes are accompanied by positive anomalies in mean annual sea level pressure over northern Africa, negative anomalies over the Arctic and parts of North America and positive anomalies over the western North Atlantic. Thus, the Green Sahara led to a strengthening of the Saharan Heat Low and a shift towards the positive phase of the Arctic Oscillation, also seen in previous experiments (Davies et al., 2015; Muschitiello et al., 2015). Finally, a strengthening of the mid-latitude westerlies and a slight strengthening of the polar easterlies led to an increase in atmospheric heat transport to the Arctic (Davies et al., 2015; Muschitiello et al., 2015). Previous experiments have also shown that the Green Sahara led to increased oceanic heat transport (Muschitiello et al., 2015; Zhang et al., 2021). In particular, the Green Sahara led to increased advection of anomalously saline waters from the western North Atlantic towards the Irminger Sea, with the ensuing salinity anomaly over the deepwater formation region leading to a strengthening of the AMOC (Zhang et al., 2021). The models in this study also show a warming and a decrease in precipitation over the western north Atlantic resulting from the inclusion of the Green Sahara. These changes are consistent with the mechanism proposed by Zhang et al. (2015), but in contrast to the results from LOVECLIM which suggest reduced oceanic heat transport due to the Green Sahara (Davies et al., 2015) and the PMIP3/4 model ensembles which suggest no change in AMOC strength between the MH and PI (C. M. Brierley et al., 2020a). Notwithstanding these differences, it is notable that all models in this study show consistent warming over the regions of the Arctic which are influenced by the AMOC. The Arctic warming could have been further amplified by the mid and high latitudes vegetation changes, which were not the focus of this study.

The Green Sahara-induced warming is not limited to the Arctic region but also extends to the Northern Hemisphere mid-latitudes. The overall warming of the Northern Hemisphere is a consistent feature of the MH$_{GS}$ experiments, leading to an overall increase in the GMST relative to the PI. This suggests that the inclusion of the Green Saharan changes may be key to estimating the evolution of Holocene temperatures and resolving the Holocene Temperature Conundrum (D. S. Kaufman & Broadman, 2023; Liu et al., 2014). Our results support the conclusions of a recent study using the CESM 1.2 model, wherein GMST estimates for 9 ka, 6 ka and 3 ka time slices showed a closer match with proxy reconstructions when vegetation

changes over the Northern Hemisphere were considered (Thompson et al., 2022). Intriguingly, in contrast to Thompson et al. (2022), our simulations only consider changes in vegetation over northern Africa, underpinned with dust reduction and land surface changes. This suggests that most of the Northern Hemisphere MST response to land cover changes is due to vegetation in northern Africa, and including vegetation changes at mid- and high-latitudes would have led to even larger warming in our simulations.

There are a few caveats to our conclusions: firstly, the use of an atmosphere-only model limits our ability to detect oceanic mechanisms of Arctic impact on north African climate, such as through impacts of Arctic climatic changes on the AMOC. A set of organic biomarker records from four marine sites off northwest Africa show the presence of an 8ka "pause" in Green Sahara conditions (Tierney, Pausata, et al., 2017). Such a pause is also observed in paleoanthropological records of human occupation in Niger , and somewhat coincides with the 8.2 ka event associated with a weakening of the AMOC . This pause has not been widely observed in other proxy reconstructions of the GSP which may be limited in temporal resolution. However, large-scale changes to the AMOC likely had an impact on north African hydroclimate (Rohling & Pälike, 2005). Secondly, we apply vegetation and other Green Saharan land surface changes uniformly throughout the year. The use of dynamic vegetation and land surface components would be an improvement, provided that it leads to an adequate simulation of the Green Sahara in the first place. Lastly, the impacts of the high latitude (Bigelow et al., 2003) and mid latitude vegetation (Binney et al., 2017) changes that occurred during the MH are not considered here. Apart from albedo changes, high-latitude vegetation changes also lead to enhanced transpiration and trigger ocean and cloud feedbacks (Kim et al., 2020; A. L. Swann et al., 2010). Mid-latitude vegetation changes could also feed back into the strengthening and northward expansion of the WAM (A. L. S. Swann et al., 2012, 2014). These vegetation changes are less well understood compared to the Green Saharan changes, and the lack of reliable vegetation maps poses a challenge in incorporating them adequately (B. Otto-Bliesner et al., 2017). Nevertheless, the SST and SIC conditions from the EC-Earth MH$_{GS}$ simulation (which were used to drive the MH$_{WA+GS}$ and MH$_{GS}$ experiments) reasonably capture the spatial extent and potentially over-estimate the magnitude of the reconstructed Arctic warming (Figure 5-3). Thus, the first-order temperature changes are not under-estimated, and hence, the conclusions drawn here regarding the role of the Arctic will not be affected by the inclusion of mid-to-high latitude vegetation change. However, future studies would benefit from the incorporation of such latitude vegetation changes as well.

The results of this study should be viewed in conjunction with several recent studies which have shown remote impacts of the MH Green Sahara (Griffiths et al., 2020; Pausata, Emanuel, et al., 2017; Pausata, Zhang, et al., 2017; Tabor et al., 2020). These teleconnections between the Green Sahara and various regions of the world are not likely restricted to the Holocene, but also to the previous Green Sahara Periods (Crocker et al., 2022; Kutzbach et al., 2020; Larrasoaña et al., 2013; Shi et al., 2024), thus holding wide implications for paleoclimate studies of the Quaternary. Our work reinforces the necessity to incorporate vegetation feedbacks and further explore the role of other land surface feedbacks, such as soil albedo and lake extent changes. It also holds implications for the future, where large-scale afforestation initiatives like the African Great Green Wall (Ingrosso & Pausata, 2024) or the planting of 50 billion trees from the Saudi Arabia – Middle East Green Initiative could have unintended consequences in far-afield regions.

(a) EC-Earth 3.1: MH$_{PMIP}$ - PI   (f) EC-Earth 3.1: MH$_{GS}$ - PI

(b) iCESM 1.2: MH$_{PMIP}$ - PI   (g) iCESM 1.2: MH$_{GS}$ - PI

(c) UofT-CCSM4: MH$_{PMIP}$ - PI   (h) UofT-CCSM4: MH$_{GS}$ - PI

(d) GISS-E2.1-G: MH$_{PMIP}$ - PI   (i) GISS-E2.1-G: MH$_{GS}$ - PI

(e) HadCM3: MH$_{PMIP}$ - PI   (j) HadCM3: MH$_{GS}$ - PI

ΔT_{ANN} (^{o}C)
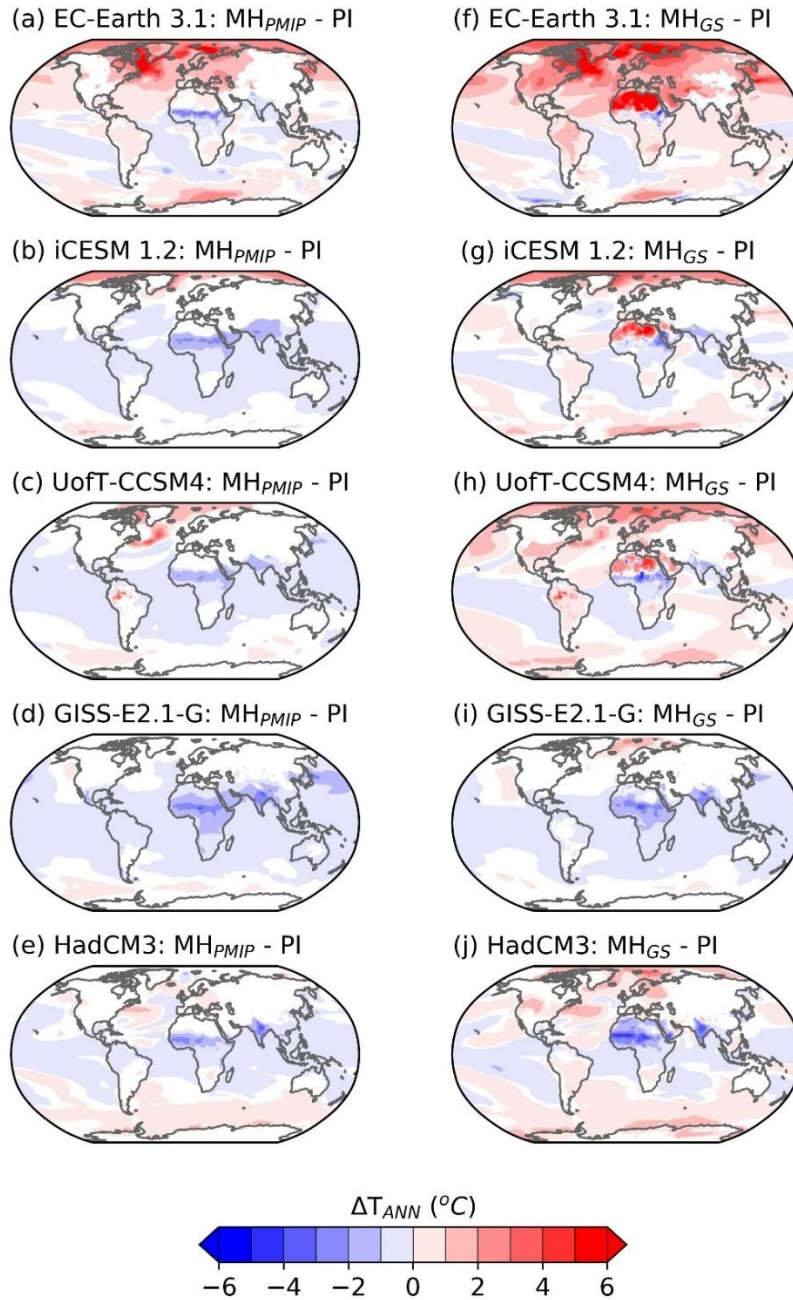
−6 −4 −2 0 2 4 6

Figure 5-1 Anomalies in mean annual temperature for (a-e) MH$_{PMIP}$ and (f-j) MH$_{GS}$ experiments relative to the PI. Only temperature changes statistically significant at the 95% confidence level, tested using the Student's t test, are shown.
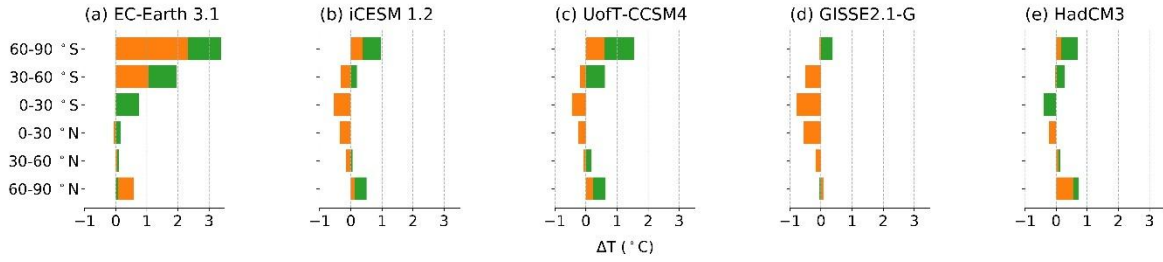
Figure 5-2 Temperature anomalies averaged over 30 °latitude bands for each model for MH$_{PMIP}$ simulations (orange) and MH$_{GS}$ simulations (green), relative to the PI.
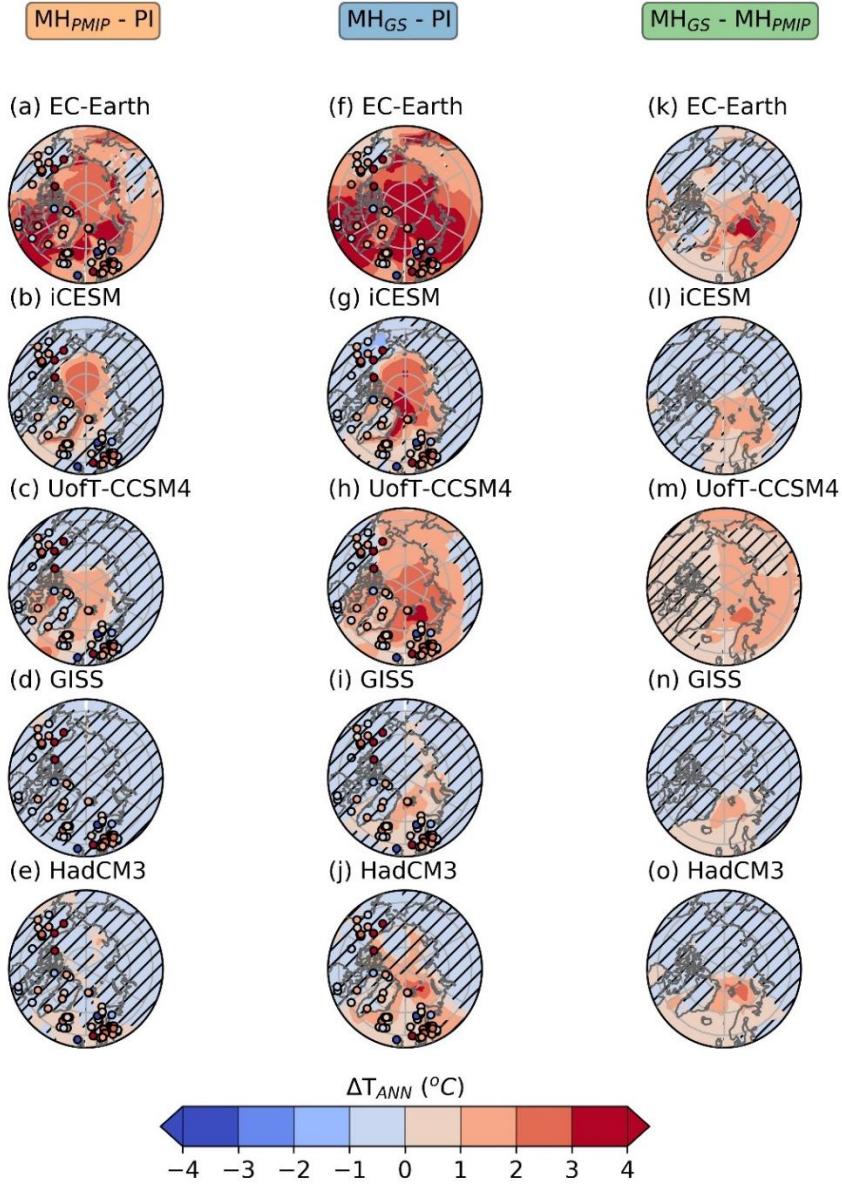
Figure 5-3 Model-proxy comparison. Colors indicate anomalies in mean annual temperature (in °C) for (a-e) MH$_{PMIP}$ relative to the PI simulations, (f-j) MH$_{GS}$ relative to the PI simulations and (k-o) MH$_{GS}$ relative to the MH$_{PMIP}$ simulations. Filled circles indicate proxy reconstructions from the Temp12k database. Hatching indicates regions where temperature anomalies were not significant at the 95% confidence level, according to the Student's t test.
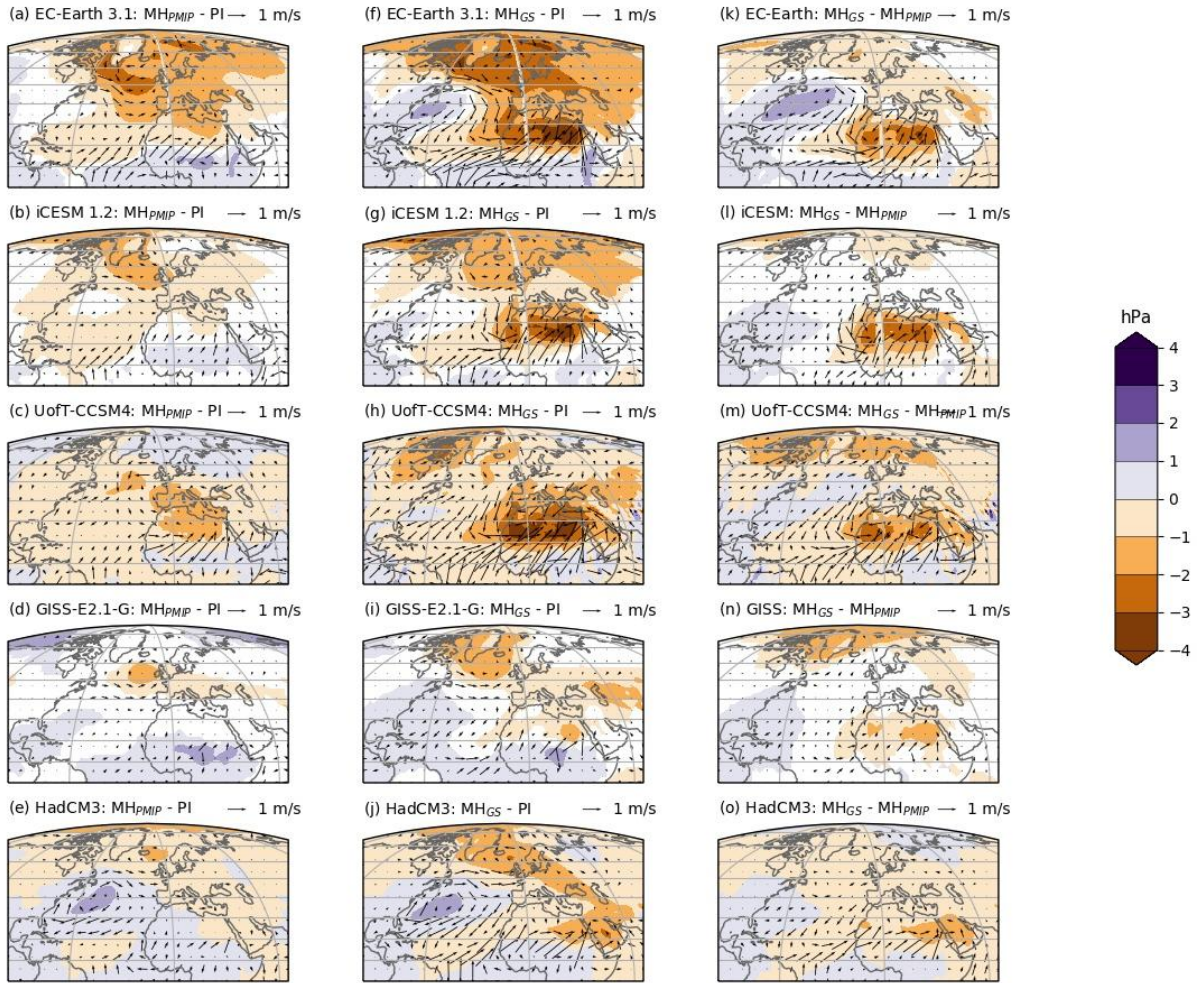
Figure 5-4 Anomalies in mean annual sea-level pressure (in hPa, shown in colors) and surface winds (overlying vectors) for (a-e) MH$_{PMIP}$ experiments relative to PI, (f-j) MH$_{GS}$ experiments relative to PI, and (k-o) MH$_{GS}$ experiments relative to MH$_{PMIP}$ experiments. At the time of submission, monthly output for sea level pressure was not available for the models UofT-CCSM4 and HadCM3, prohibiting statistical testing. For the other models, only sea-level pressure anomalies which are statistically significant at the 95% confidence level (based on the Student's *t* test) are shown.
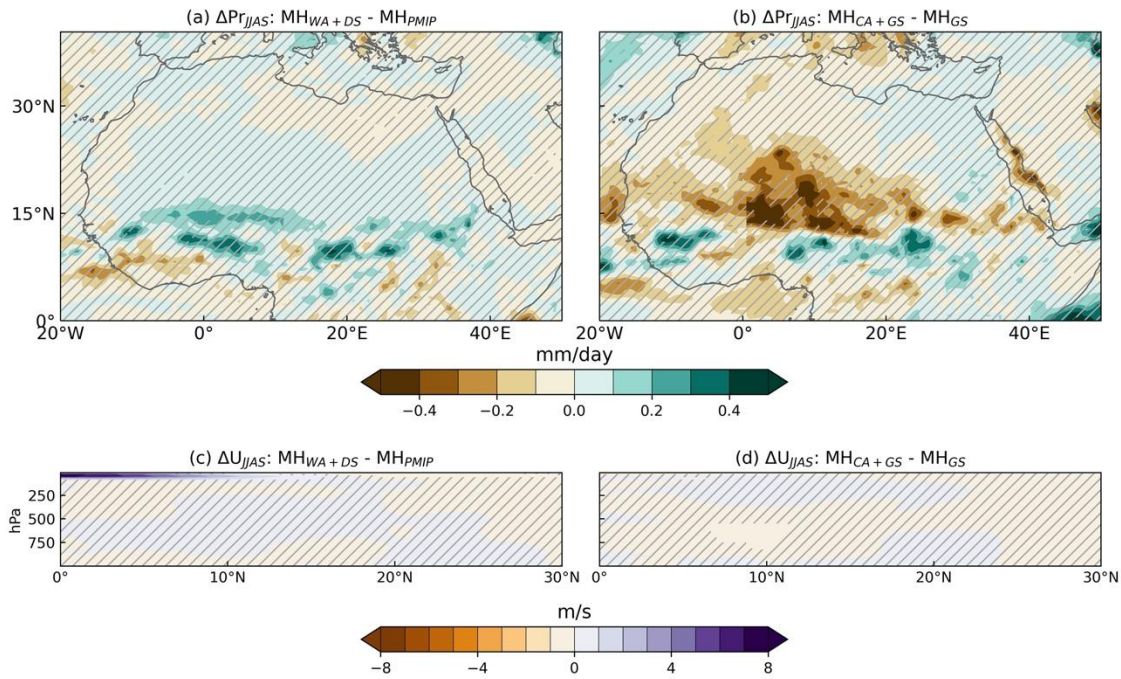
Figure 5-5 Effect of Arctic temperature changes over northern Africa. Top row shows boreal summer (JJAS) precipitation anomalies in mm/day for (a) the MH$_{WA+DS}$ experiment relative to the MH$_{PMIP}$ experiment, and for (b) the MH$_{CA+GS}$ experiment relative to the MH$_{GS}$ experiment. Bottom row shows boreal summer zonal wind strength anomalies in m/s at 0 °E for (c) the MH$_{WA+DS}$ experiment relative to the MH$_{PMIP}$ experiment, and for (d) the MH$_{CA+GS}$ experiment relative to the MH$_{GS}$ experiment. Positive values indicate eastward (westerly) winds. Hatching indicates anomalies which were not significant at the 95% confidence level.

Model	ΔGMST (°C)		Cohen's Kappa		ΔRMSE (°C)	
	MH$_{PMIP}$ – PI	MH$_{GS}$ - PI	MH$_{PMIP}$	MH$_{GS}$	MH$_{PMIP}$	MH$_{GS}$
EC-Earth	0.38	0.84	0.435	0.435	5.49	5.515
iCESM	-0.28	0.12	0.01	0.28	6.687	7.027
UofT-CCSM4	-0.17	0.3	0.164	0.435	5.443	5.255
GISS	-0.46	-0.3	0.0	0.077	8.41	8.146
HadCM3	-0.1	0.04	0.146	0.435	5.396	5.518

Table 5-1 Key results for GMST changes and proxy-model intercomparison based on mean annual temperature data.

CONCLUSION

Key outcomes of the thesis

This PhD thesis focused on the remote impacts of the mid-Holocene (MH) Green Sahara on three specific regions: South America, the equatorial Pacific and the Arctic. The focus was to identify consistent multi-model results, so as to avoid identifying teleconnections which were dependent on model physics or the specific ways used to simulate the Green Sahara. To this end, four fully coupled global climate models were used: EC-Earth version 3.1 (Hazeleger et al., 2010), isotope enabled Community Earth System Model (iCESM) version 1.2 (Brady et al., 2019), University of Toronto version of the Community (Peltier & Vettoretti, 2014) 4 (Peltier & Vettoretti, 2014) or UofT-CCSM4, and Goddard Institute of Space Studies (GISS) Model E2.1-G (Kelley et al., 2020). For each model, two simulations with (MH$_{GS}$) and without the Green Sahara (MH$_{PMIP}$) were analysed. The MH$_{GS}$ simulations showed improved proxy-model agreement, lending greater credence to the simulation protocols used and reinforcing the need for incorporating Green Saharan changes in studies of MH climate. The atmosphere-only Global Environmental Multiscale (GEM) model version 4.8.12 (Girard et al., 2014; McTaggart-Cowan et al., 2019) was also used to run experiments designed to isolate the role of Arctic climate changes (Chapter 3).

Consistent multi-model results show that:

i.   The Green Sahara led to a reduction in precipitation over the South American continent. The models indicate a reduction of 0.5 mm/day in large parts of the continent, with some regions showing a reduction of 2 mm/day. This drying was related to, but not limited to, a weakening of the South American Monsoon during austral summer.

ii. The Green Sahara led to a La Niña-like mean state and a reduction in the El Niño Southern Oscillation (ENSO) variability in the equatorial Pacific. SST variability during boreal winter over the Niño3.4 region shows reductions of 5-28% in the different models.

iii. The Green Sahara led to an increase in temperatures over the Arctic, particularly in the Atlantic-influenced sector. The models indicate an increase of 1 °C over various regions such as Greenland Sea, Norwegian Sea, Fennoscandia and Barents Sea, with warming of up to 4 °C in the Barents Sea. The Northern Hemisphere saw warming over the mid-latitudes as well, eventually leading to an increase in global-mean mean annual surface temperatures in the order of 0.1 – 0.8 °C.

Synthesis of results

A synthesis of results from the three chapters shows that the temperature, precipitation and SST variability anomalies driven by the Green Sahara (estimated through MH_{GS} anomalies relative to the MH_{PMIP} simulation) were similar in direction and comparable in magnitude to the changes driven by orbital forcings (estimated through MH_{PMIP} anomalies relative to the PI, where PI refers to the pre-Industrial). Thus, the Green Sahara led to an amplification of orbitally-driven changes, evidenced by the following:

- The first instance is over northern Africa itself, where the orbital forcings lead to a modest increase in precipitation of up to 2 mm/day, and the inclusion of the Green Sahara increased this to at least 3 mm/day.

- Over South America, the inclusion of the Green Sahara exacerbated the orbitally driven reduction in precipitation (~1 mm/day over most parts) to up to 3 mm/day.

- In the case of ENSO variability, this holds true for three out of four models (except GISS), where the orbital forcings drives 1-12% reductions in Niño3.4 variability, which are amplified to 5-28% reductions upon the inclusion of the Green Sahara. In the case of GISS, the orbital forcing leads to an increase in Niño3.4 variability during the MH relative to the PI. However, the Green Sahara drives a reduction in the ENSO variability (like the other three models).

- Lastly, in the case of the Arctic, the orbital changes led to positive anomalies in mean annual temperature averaged over the Arctic in the case of three models, which are amplified by the inclusion of the Green Sahara. Again, the exception is GISS, which shows a small and statistically insignificant cooling over the Arctic due to the orbital forcing, but an overall warming upon the inclusion of the Green Sahara.

Implications of the findings

The most significant implication of the findings presented here is that simulations of the MH that do not account for Green Saharan changes (particularly the vegetation changes) lead to inadequate

representation of teleconnections between northern Africa and other regions of the world. Thus, it is imperative to include these changes while studying the MH climate of any region over the world, especially in coordinated experiments such as those conducted by the Paleoclimate Modelling Intercomparison Project (B. Otto-Bliesner et al., 2017). These vegetation changes could be included either by using dynamic vegetation or through prescribed vegetation. If prescribing vegetation changes, it would be preferable to include vegetation changes over other regions as well, such as the Northern Hemisphere mid-latitudes (Binney et al., 2017) and high-latitudes (Bigelow et al., 2003). However, the understanding of these changes is limited compared to that of the vegetation changes over northern Africa (Bartlein et al., 2011; Hély et al., 2014; Watrin et al., 2009). In theory, a convenient workaround could be the use of dynamic vegetation models. However, past studies have shown that the use of dynamic vegetation does not necessarily lead to an adequate representation of the Green Sahara (Pascale Braconnot et al., 2012; Tierney, Pausata, et al., 2017). Further, the use of dynamic vegetation models presents its own set of challenges, such as the choice of appropriate model parameterizations and delineating the impacts of land use changes (Pascale Braconnot et al., 2019; Dallmeyer et al., 2023). A few recent studies have simulated precipitation changes comparable to those estimated by proxy reconstructions (Dallmeyer et al., 2021; Thompson et al., 2022). Provided they are first validated through comparison with proxy reconstructions, dynamic vegetation models offer the most feasible way for future studies of the Green Sahara. Lastly, vegetation changes should also be included in the study of pre-Holocene GSPs (Crocker et al., 2022b; Larrasoaña et al., 2013).

Taking a broader perspective, these findings reinforce that non-linear feedbacks in the climate system can lead to rapid changes. These feedbacks must be incorporated in simulations of the future to provide an adequate estimation of the risk of abrupt and unmitigable climate change (O'Neill et al., 2016).

Limitations of this work

The climate models used in this study have spatial resolutions comparable to PMIP4 models; however, the representation of atmosphere-land surface surface interactions would be improved with higher resolution models. The use of dynamic vegetation would likely lead to an improved representation of seasonality in the vegetation cover compared to the use of prescribed vegetation, provided this improvement is not offset by an under-representation of resultant precipitation anomalies. The models used in this study

broadly follow the PMIP4 recommendations for vegetation sensitivity experiments, and have prescribed Green Saharan changes which are well-supported by proxy reconstructions. However, the simulation protocols were not strictly the same. For example, two models in this study incorporate reduced dust conditions during the MH, while the other three do not. The impacts of such differences are difficult to quantify. Lastly, the metrics used for proxy-model comparisons provide limited insight. The Cohen's Kappa score takes into account only qualitative agreement between proxies and models, and thus may not reflect improvements over several areas. These limitations may be addressed in future work, as recommended below.

Recommendations for future research

A few questions emerge related to the representation of the Green Sahara in model simulations as well as the specific teleconnections identified in this thesis.

What is the role of GCM resolution in determining the ability of a climate model to simulate the MH Green Sahara as well as its remote impacts? The models used in this study had spatial resolution ranging from 1° (UofT-CCSM4) to 3.75° (HadCM3). Future work should attempt to better constrain the effect of orbital changes on the WAM using higher resolution models and/or dynamically downscaled outputs, taking advantage of the improved representation of land-atmosphere interactions.

Several positive feedback mechanisms played a role in amplifying the orbitally-driven intensification of the WAM during the MH (such as vegetation, lake and soil feedbacks). Firstly, it appears that the vegetation feedback was the most crucial, since simulations excluding vegetation changes but including other land surface changes do not show an adequate intensification of the WAM. Do current dynamic vegetation models adequately represent the vegetation feedback during the GSP? Secondly, while the importance of the vegetation feedback is relatively clear, the individual role of other land surface changes needs to be understood. This is an important consideration to determine where future modelling efforts should be directed. For eg., after the inclusion of vegetation changes, would simulations be improved more by including the presence of megalakes or changes to soil albedo? Thirdly, what is the role of dust changes in driving changes to local and remote climates? Only two models in this study (EC-Earth and iCESM) incorporated dust changes during the MH, yet, the results obtained from all models are qualitatively

consistent. It remains possible to simulate the Green Sahara through the use of different pathways, highlighting the limitations of our understanding of the role of individual changes.

The teleconnections identified here are based on physical processes which are also observed during the present day, and are unlikely to have changed during the recent geological past. Thus, it may be expected that these remote impacts of the Green Sahara were also operative during the pre-Holocene GSPs. However, the modulation of these teleconnections by other forcings such as the insolation changes warrants study.

In the absence of dynamic vegetation, model simulations depend on prescribed changes to vegetation cover. Currently, there is a lack of widely accepted paleo-vegetation distribution maps which make it difficult to include the vegetation feedback in studies of the MH. Future efforts should be focused on developing reliable maps of vegetation cover for the MH as well as for the pre-Holocene GSPs (for eg. the *lig127k* time slice popularly used for studying the Last Interglacial).

Two mechanisms likely played a role in the Green Sahara-driven reduction in ENSO variability during the MH: changes to the Atlantic Niño and the North Tropical Atlantic warming. The relative role of these two mechanisms during different phases of the GSP should be studied further and quantified. Future work should also focus on the role of the Barents Sea Bias in modelling of the MH Arctic climate, and a potential role of the middle-late Holocene Arctic cooling in contributing to Saharan desertification through oceanic pathways which could not be studied due to the use of an atmosphere-only model in this thesis. Lastly, future work should attempt to identify if the Green Sahara played a role in driving variability in other tropical regions such as the Indian Ocean.

ANNEXE A

SUPPLEMENTARY INFORMATION FOR ARTICLE 1

Text S1.

Model evaluation

A comparison of the model pre-Industrial simulations with observational and reanalysis datasets elicits some shortcomings that are common to all models, albeit to different extents:

1. The models display a spurious second Inter Tropical Convergence Zone (ITCZ) in the southern equatorial Atlantic Ocean, which leads to an over-estimation of precipitation in the relatively dry region of northeastern Brazil.

2. The models do not adequately represent the South Atlantic Convergence Zone (SACZ). The northwest-southeast oriented precipitation band over South America is problematic in all models except EC-Earth. The spurious second ITCZ is a probable cause of an unrealistic Hadley Circulation which leads to increased subsidence over the south western Atlantic Ocean, and inhibiting convective precipitation over the SACZ.

There are also some model-specific regional biases. For example, there is an overestimation of precipitation in northwestern Amazon region in UofT-CCSM4 and an under-estimation of precipitation in northern South America in iCESM 1.2.

Overall, different models have different abilities to capture key elements of the climate over South America and the equatorial Atlantic Ocean. GISS-E2.1-G shows the largest (wettest) second ITCZ bias and under-estimates precipitation over the continental SACZ region. iCESM shows the widest second ITCZ, spanning nearly the entire equatorial Atlantic . EC-Earth performs relatively better than the other models, with the most muted second ITCZ and the most realistic representation of the SACZ. These observations are in line with previous studies of the ability of CMIP6 models to simulate the present-day climate over this region which indicated the superior performance of EC-Earth (Almazroui et al., 2021; Dias & Reboita,

2021). However, a relatively better performance in simulating present-day climate, where interannual variability dominates, does not necessarily indicate better ability to simulate the paleo-climate, where changes to orbital forcing, greenhouse gas concentrations or topography were more important. For instance, despite simulating present-day climate reasonably, CESM2 has been shown to have a high Equilibrium Climate Sensitivity (Zhu et al., 2022). Thus, despite inherent biases, there are important conclusions that can be drawn by the results common to all models.

Text S2.

Representation of the mid-Holocene Green Sahara (MH$_{GS}$) in the models

The mid-Holocene (MH) was characterized by large-scale vegetation changes from desert to shrub and savanna over northern Africa. The PMIP4 recommendations for vegetation sensitivity experiments include changing vegetation over the Sahara to evergreen shrub up to 25 °N and savanna/steppe vegetation poleward of 25 °N (B. Otto-Bliesner et al., 2017). The vegetation changes also led to decreases in dust mobilization and soil albedo, and changes in surface hydrology.

Different models in this study treat the presence of the Green Sahara differently. In the EC-Earth 3.1 MH$_{GS}$ simulation, vegetation over the Sahara was set to shrub, and dust was reduced by up to 80% relative to the PI. In the iCESM 1.2 MH$_{GS}$ simulation, present day Sahelian land surface and vegetation characteristics at 11 °N were imposed over the Sahara. The use of an interactive dust scheme led to a decrease in dust mobilization. In the UofT-CCSM4 MH$_{GS}$ simulation, tropical rainforests were extended northwards, the Sahara was completely replaced by evergreen shrubs up to 25 °N and almost completely (90%) replaced by a mix of steppe and savanna beyond 25 °N. Further, soil albedo was reduced to reflect greater moisture and organic matter, and the presence of five megalakes was incorporated through land surface changes. In the GISS-E2.1-G MH$_{GS}$ simulation, bare soil and grass over the Sahara were replaced by arid shrub below 25 °N and by grassland above 25 °N. The vegetation changes lead to a reduction in surface albedo from ~0.3 to 0.15-0.19 over the Sahara.

Text S3.

Proxy-model comparisons

To compare the effects of the Green Sahara on monsoon regimes within northern Africa and South America, we considered precipitation proxies from terrestrial and marine records within these respective domains: 0°-38°N; 20°W-45°E and 50°S-15°N; 80°W-30°W. The proxy data, derived from previously synthesized databases, includes records of pollen-based mean annual precipitation reconstructions (Bartlein et al., 2011), lake level records from Africa (Tierney et al., 2011), and an updated multiproxy hydroclimate reconstruction from South America (Gorenstein et al., 2022). We also included hydroclimate reconstructions from Bolivia, Colombia and Peru (Harrison et al., 2003) to fill in more data gaps in the tropical South American region. In total, we have collated 252 proxy records in which each MH hydroclimate response relative to PI is compared against model outputs.

To compare the proxies with models, MH precipitation responses relative to PI conditions were all categorically defined as either drier (rated as -1), wetter (1), or unchanged (0). Field reconstructions of mean annual precipitation from (Bartlein et al., 2011) were converted to these categories based on the reported change for each grid point. Original classifications of lake level reconstructions from Africa (i.e., "low", "intermediate", and "high" (Tierney et al., 2011) for MH and PI periods were used to derive lake level status. These included higher, lower and unchanged to represent wetter, drier and unchanged, respectively. Categories for hydroclimate reconstructions from South America and additional records in this region follow the interpretation of the original publications (i.e., Gorenstein et al., 2022; Harrison et al., 2003). Simulated changes in precipitation from the nearest grid points to the proxy sites were extracted and similarly placed into three categories based on the direction of change and statistical significance.

To quantify the agreement between models and proxies, we used Cohen's κ statistic defined as the observed fractional agreement (p_o) between raters (i.e., proxies and models) relative to the probability of random agreement (p_e):

$$\kappa = (p_o - p_e) / (1 - p_e)$$

where p_o is the sum of the diagonal elements in the proxy-model matrix divided by the total number of samples, N; and p_e is the product of the sum of each matrix row and column (given by the frequency of occurrence of each category) normalized by N. We implemented weights in the κ calculation by multiplying the data by a weight matrix that penalizes models for a total disagreement (i.e., drier when it should be wetter and vice versa) to a value of 0 and near miss (i.e., drier or wetter when it should be unchanged) to a value of 0.5.
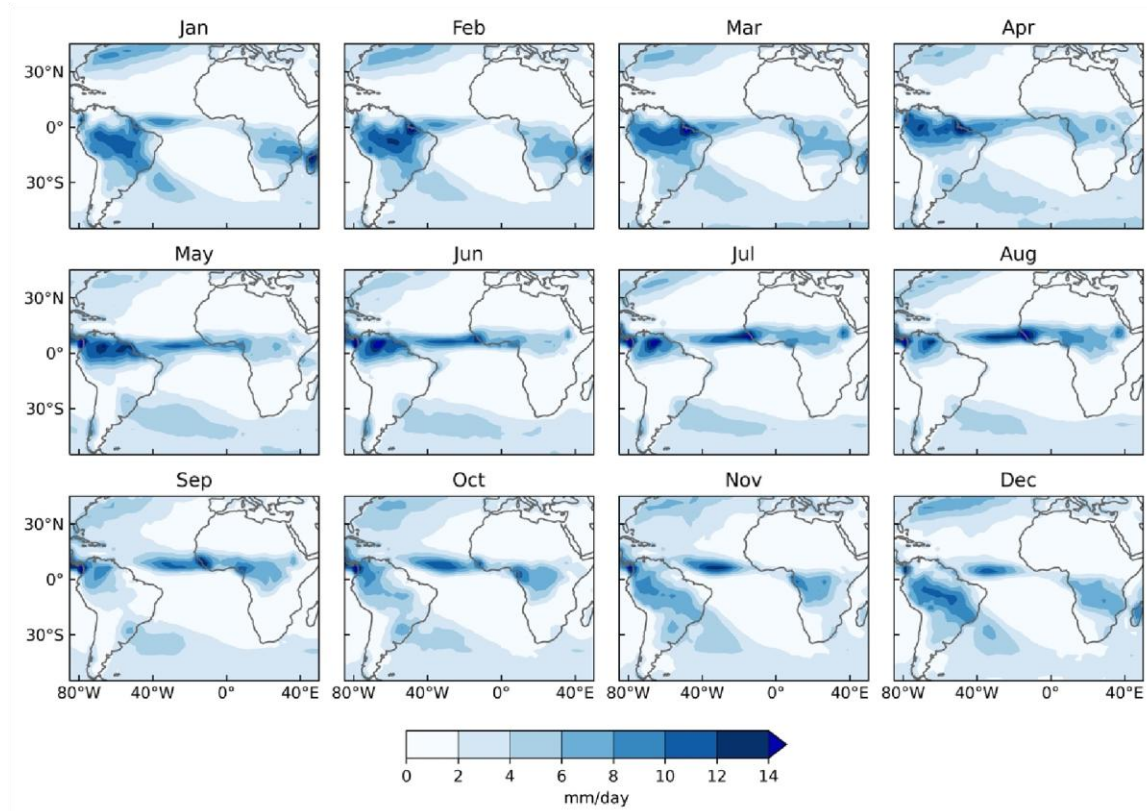
Figure A 1 Present-day monthly precipitation patterns from the Global Precipitation Climatology Project (GPCP) version 2.2 from 1979-2009 (Huffman et al., 2015).
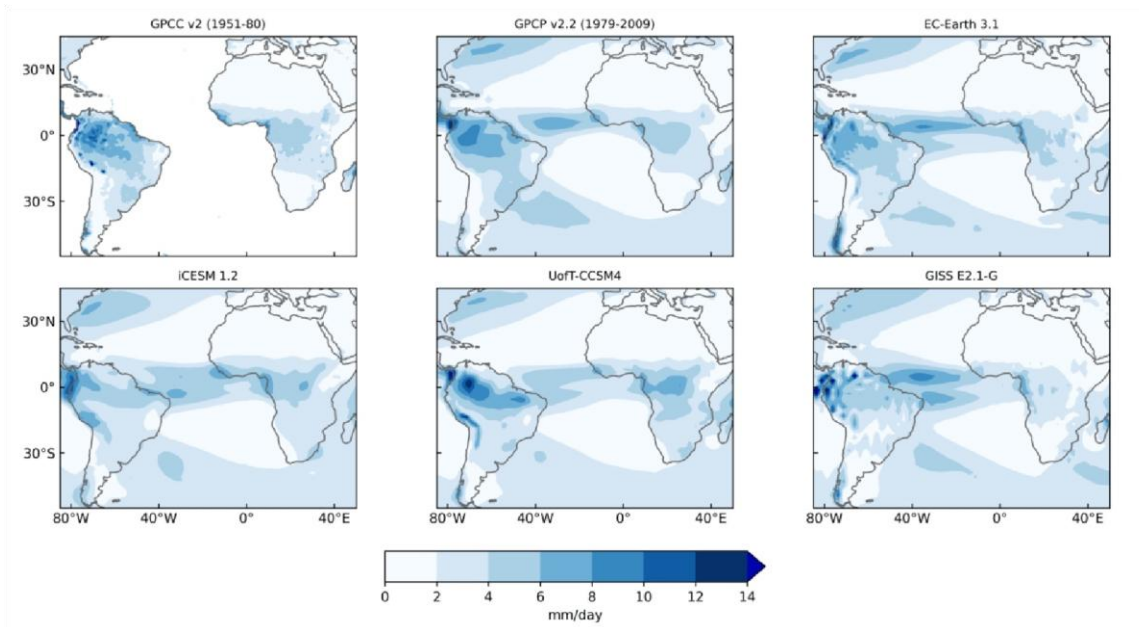
Figure A 2 Comparison of annual precipitation patterns over South America between the Global Precipitation Climatology Centre (GPCC) Reanalysis Dataset, Global Precipitation Climatology Project (GPCP) Dataset and the PI simulations from EC-Earth 3.1, iCESM 1.2, UofT-CCSM4 and GISS-E2.1-G.
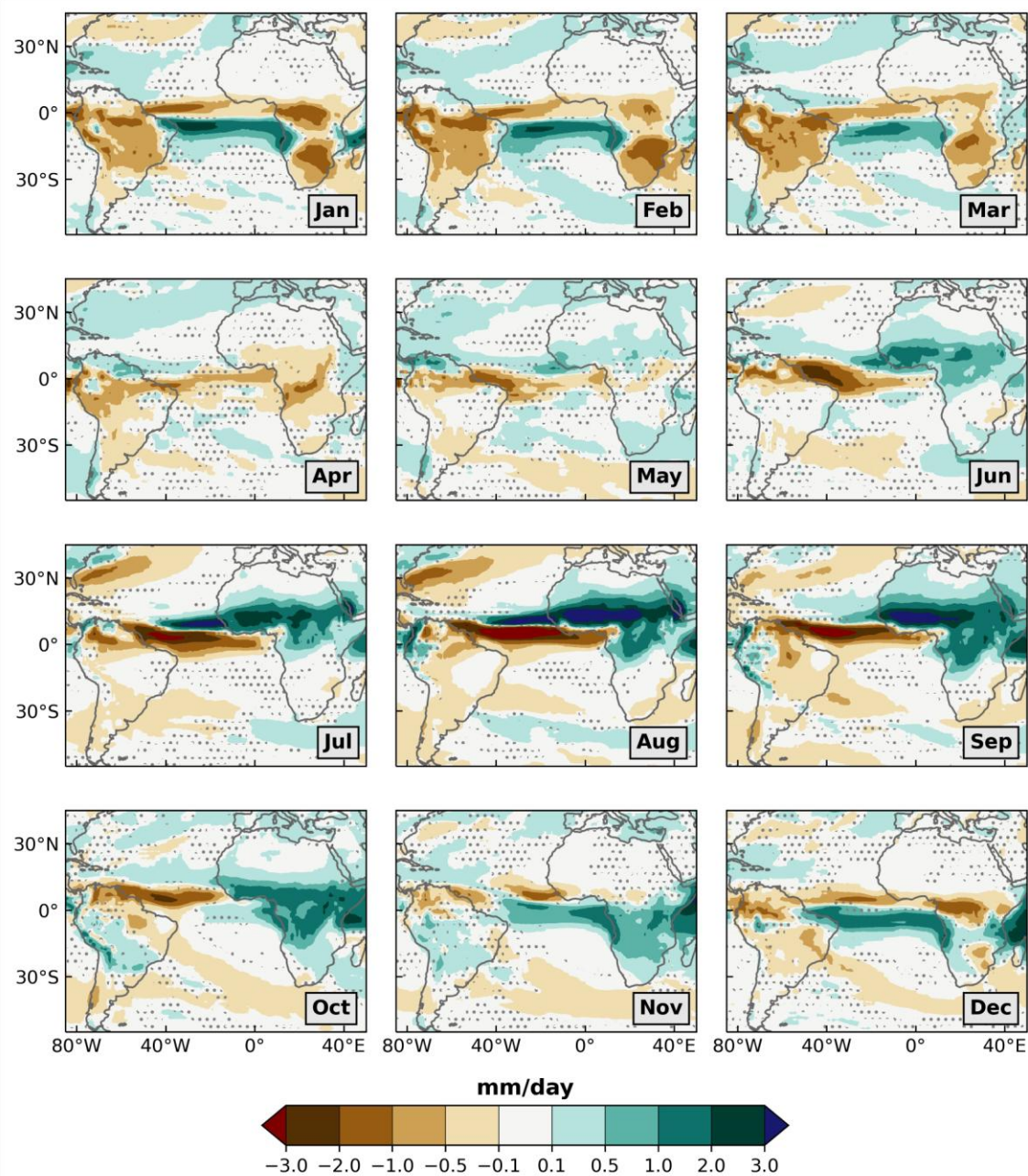
Figure A 3 Precipitation changes between MH_{PMIP} and PI experiments, shown as multimodel averages for each month. Stippling indicates areas in which less than three models agree on the sign change.
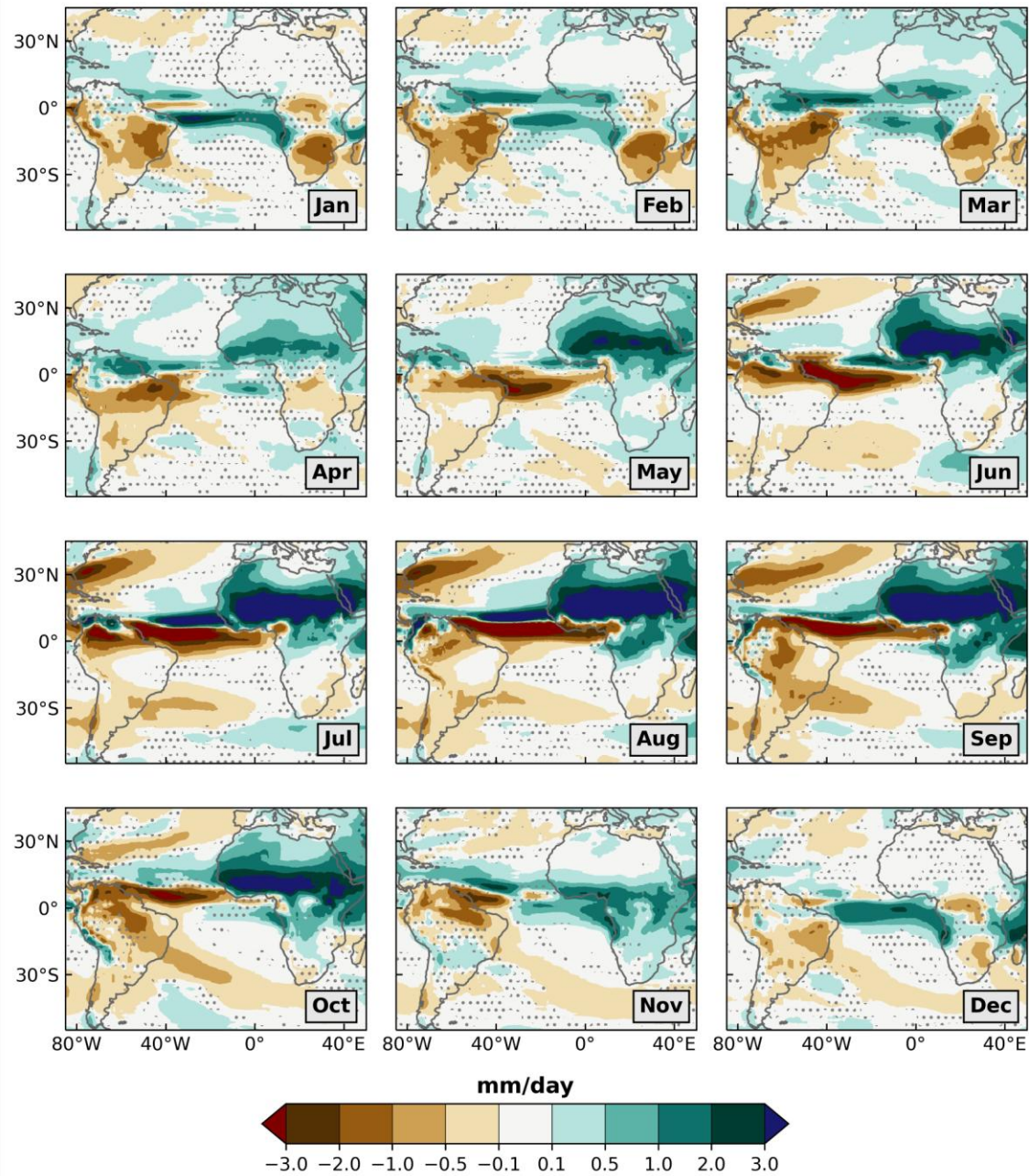
Figure A 4 Precipitation changes between MH$_{GS}$ and PI scenarios, shown as multi-model averages for each month. Stippling indicates areas in which less than three models agree on the sign change.
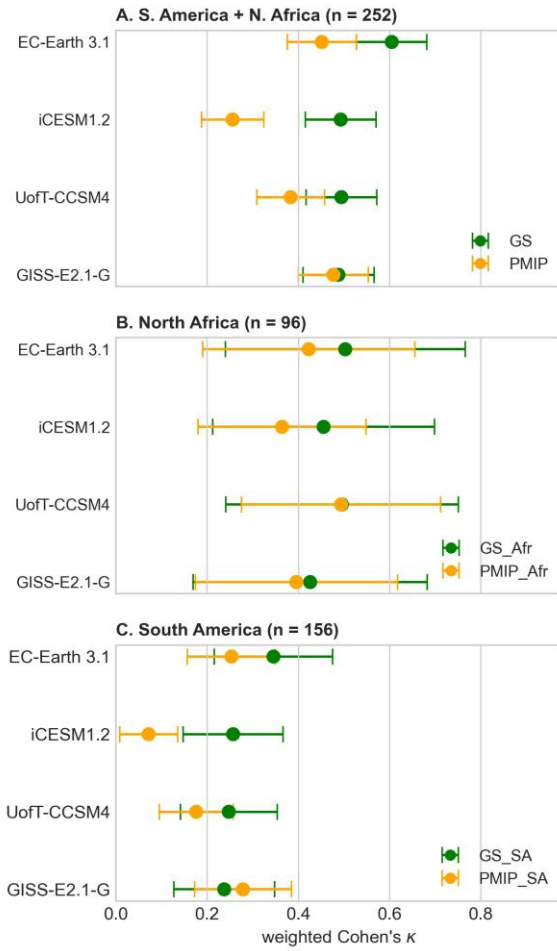
Figure A 5 Weighted Cohen's κ score between MH$_{GS}$ (green dots) and MH$_{PMIP}$ (orange dots) scenarios over (a) South America and northern Africa, (b) northern Africa (0° to 38°N and 20°W to 45°E) and (c) South America (50°S to 15°N and 80°W to 30°W) regions. All datapoints are statistically significant (p < 0.05). Error bars indicate 95% confidence intervals.
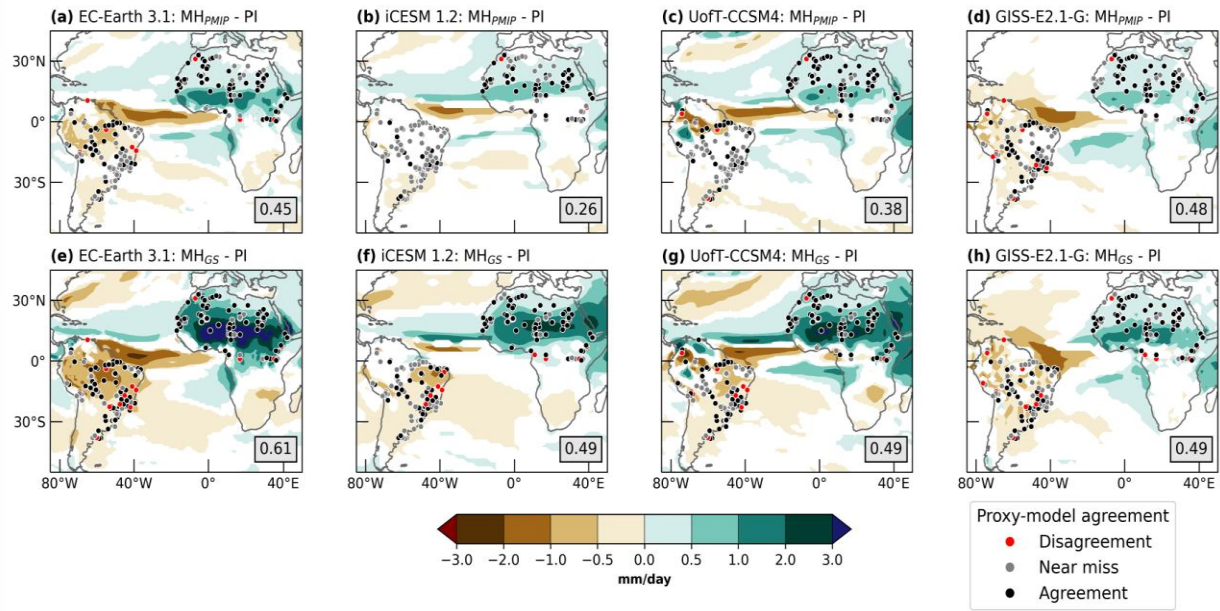
Figure A 6 Proxy-model agreement over the region of study. Colors show MH-PI annual precipitation changes in mm/day. Only changes significant at the 95% confidence level are shown. Proxy sites are shown by circles, with the color indicating disagreement ("total miss"; red), near-miss (grey) and agreement (black).

	EC-Earth 3.1	**iCESM 1.2**	**UofT-CCSM4**	**GISS-E2.1-G**
Model name	EC-Earth	Community Earth System Model	Community Climate System Model	Goddard Institute for Space Studies Model
Atmospheric component	Integrated Forecast System	Community Atmosphere Model v5.3 (iCAM5)	Community Atmosphere Model v4 (CAM4)	Goddard Institute for Space Studies Model E2.1
Atmospheric grid	1.125 x 1.125 (62)	1.9 x 2.5 (30)	1 x 1 (26)	2 x 2.5 (40)
Oceanic component	Nucleus for European Modelling of the Ocean v2 (NEMO2)	Parallel Ocean Program v2.0 (POP2)	Parallel Ocean Program v2.0 (POP2)	GISS Ocean Model v1
Oceanic grid	1 x 1 (46)	1 x 1 (60)	1 x 1 (60)	1 x 1.25 (40)
Simulation protocols	CMIP5 / PMIP3	CMIP6 / PMIP4	CMIP6 / PMIP4	CMIP6 / PMIP4
Feedbacks incorporated in the MH$_{GS}$ simulation	Vegetation, dust	Vegetation, dust, soil	Vegetation, soil, lakes	Vegetation
PI-to-MH albedo change over northern Africa	0.3 to 0.15	0.3 to 0.15	0.3 to 0.16	0.3 to 0.19
Reference for simulations	Pausata et al. (2016)	Tabor et al. (2020)	Chandan and Peltier (2020)	This paper

Table A 1 Model details. Numbers in parentheses indicate number of vertical levels in the atmospheric or oceanic grid.

ANNEXE B

SUPPLEMENTARY INFORMATION FOR ARTICLE 2

Text S1 : Model evaluation

The climate models used in this study suffer from certain common model biases.

Firstly, climate models commonly suffer from the double ITCZ problem i.e. the presence of a second, spurious precipitation band south of the equator in the tropical Pacific and Atlantic Oceans. The models used in this study also show the second ITCZ in both oceans, with the notable exception of EC-Earth which has no second ITCZ in the tropical Pacific. The second ITCZ is most pronounced in HadCM3.

Secondly, climate models commonly suffer from various biases in the Atlantic, particularly related to the simulation of the Atlantic Niño. The models used in this study show a warm bias in the region of the Atlantic Cold Tongue, with only EC-Earth and UofT-CCSM4 showing a small and disjunct cool patch in the central equatorial Atlantic which is positioned too westwardly. HadCM3 shows a considerable warm bias in the tropical Atlantic. The absence/westward displacement of the Atlantic Cold Tongue is also reflected in a significant under-estimation of west-to-east SST gradients in the equatorial Atlantic during boreal summer. The under-representation of Atlantic Niño in climate models can also be gauged by the SST variability, which is expected to peak during boreal summer with the development of the Atlantic Cold Tongue. EC-Earth shows higher variability than observational datasets. The other four models show lower or temporally displaced variability.

Thirdly, climate models commonly suffer from various biases in the Pacific, most notably the Pacific Cold Tongue bias and the Western Pacific Warm Pool bias. With the exception of GISS, the climate models used in this study show a greater westward extension of the Pacific Cold Tongue, compared to observational datasets. The westward extent of the Pacific Cold Tongue is reasonable in GISS, but there is a warm bias in the southeast tropical Pacific (between 70-100 W). EC-Earth and UofT-CCSM4 show a cool bias in the Cold Tongue region. The Western Pacific Warm Pool is generally simulated inadequately warmly, with the exception of iCESM. However, iCESM shows a greater extension of the Warm Pool in the southern tropical

Pacific. With regards to SST variability, all models showed a reasonable magnitude and extent of the region with the highest SST variability in the equatorial Pacific.
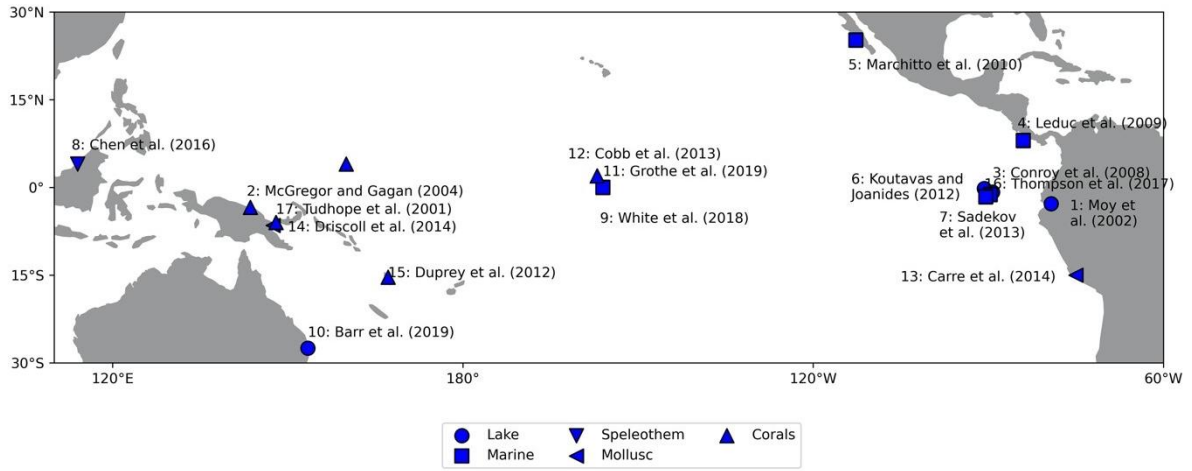
Figure B 1 Sites of paleoclimatic reconstructions cited in this study and listed in Table 5.
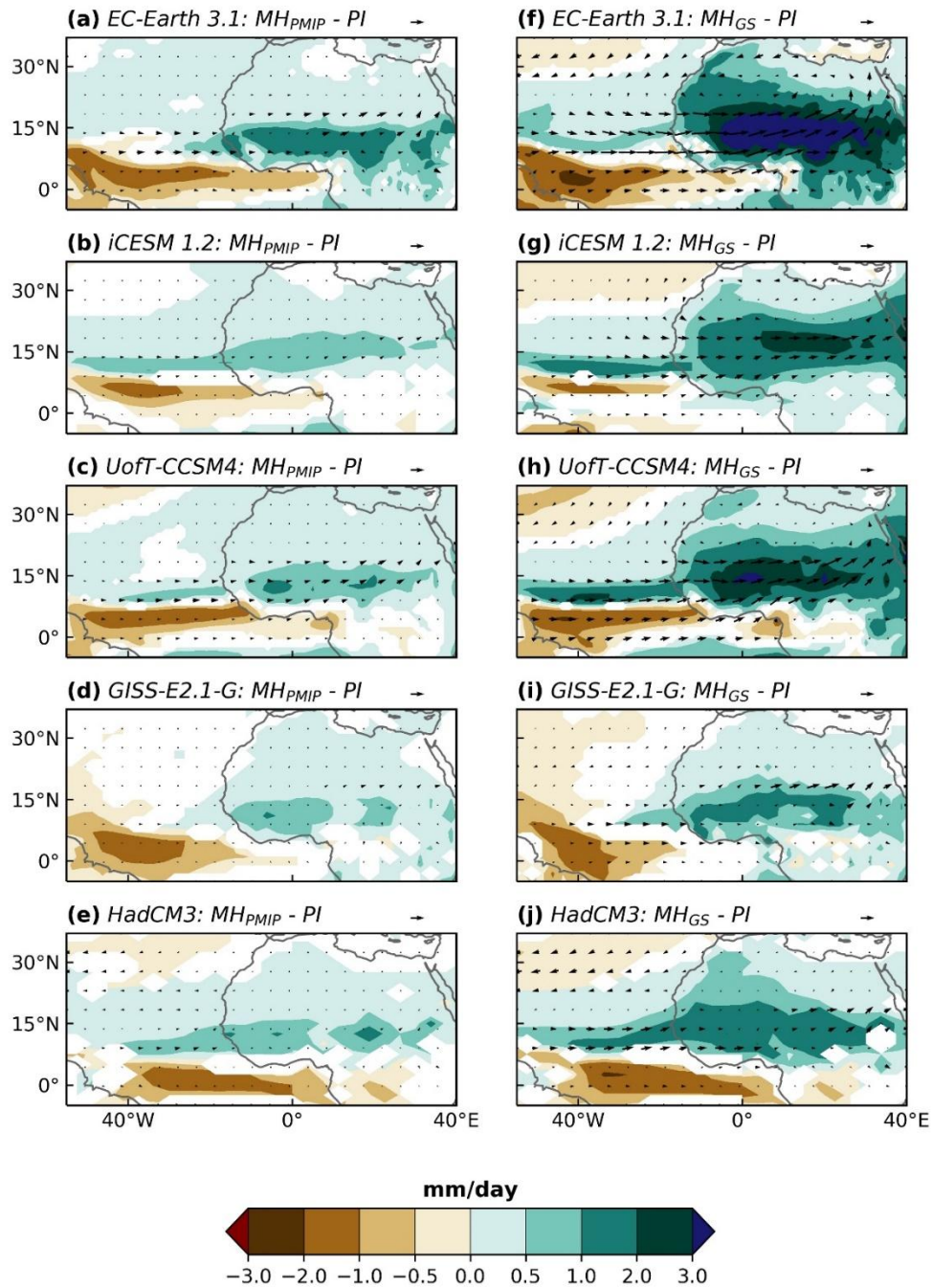
Figure B 2 Annual precipitation and low-level (850 hPa) wind anomalies for (a-e) MH$_{PMIP}$ and (f-j) MH$_{GS}$ simulations, relative to the respective PI simulations. Arrow keys on the top-right indicate wind strength of 2.5 m/s.
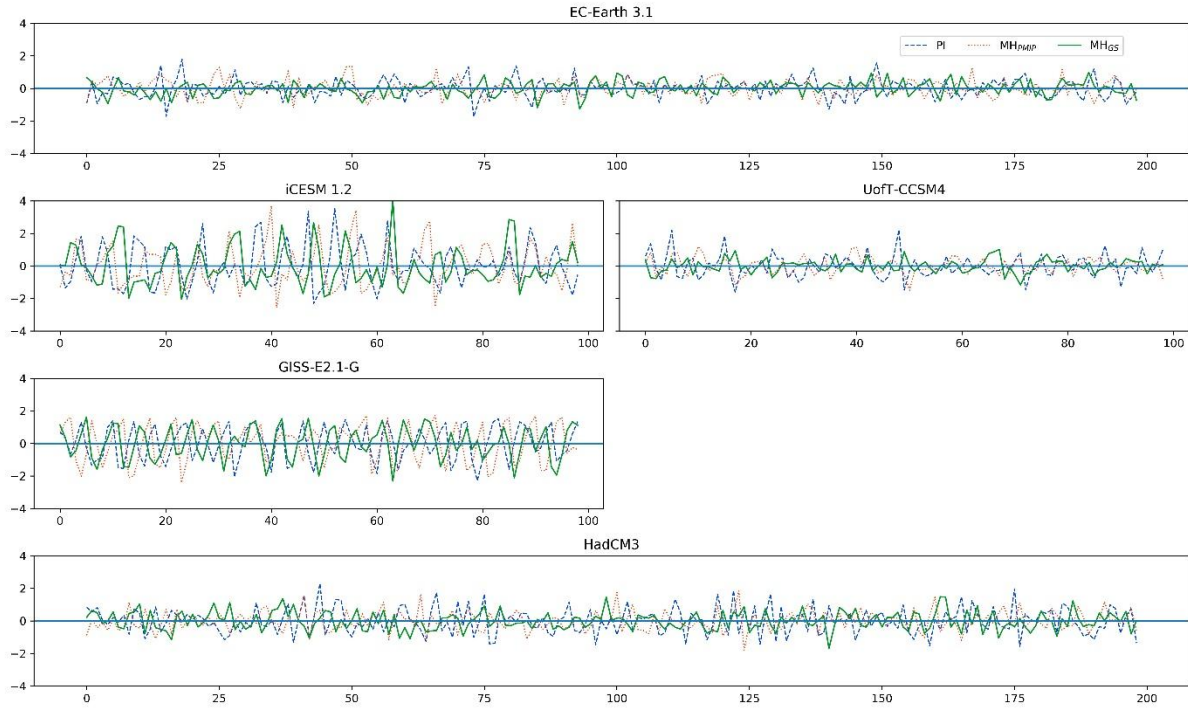
Figure B 3 Time series for 5-month smoothened boreal winter (DJF) SST anomalies averaged over the Niño3.4 region. Note that the x-axis for each model depends on the length of the available model outputs.
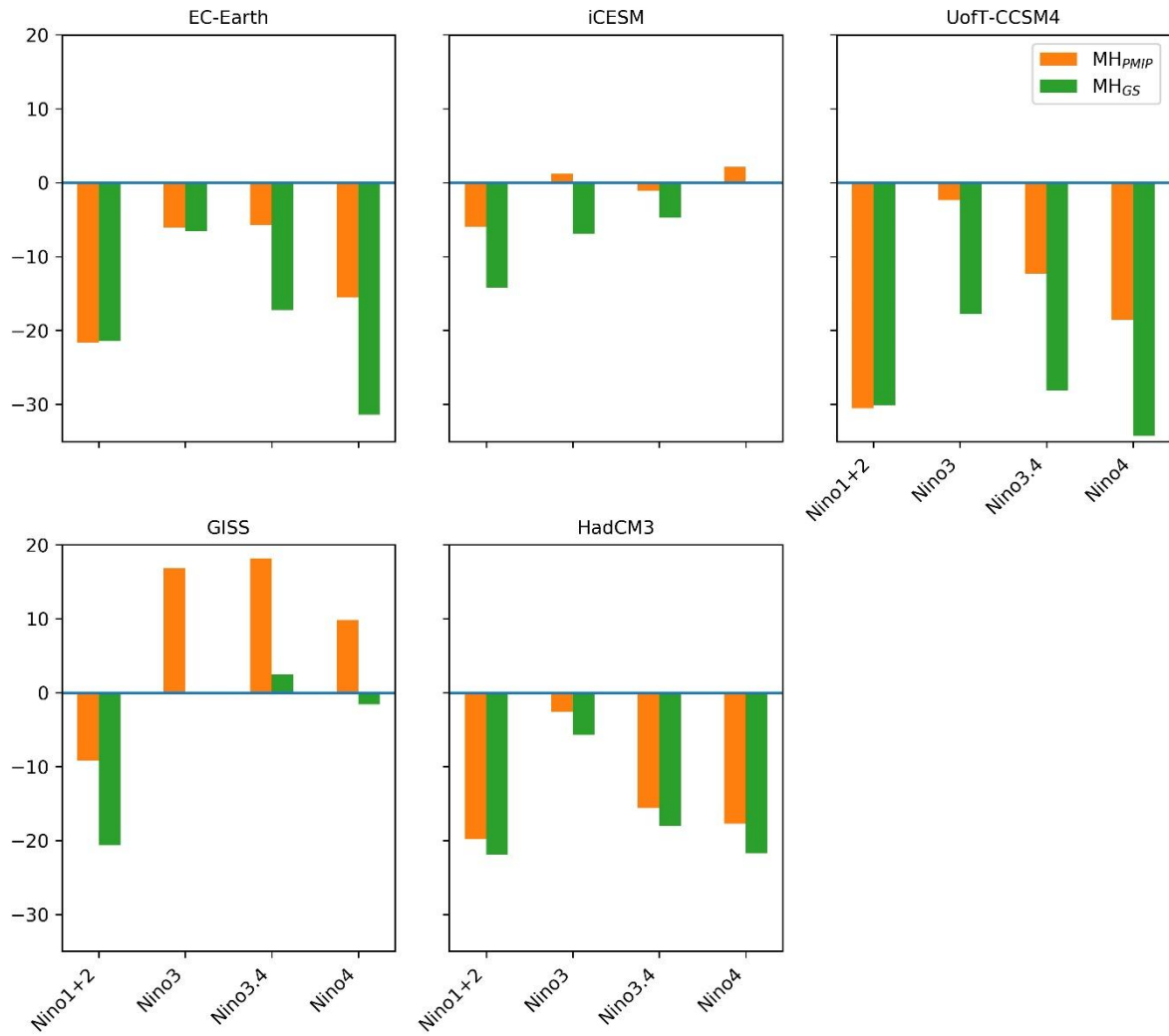
Figure B 4 Percentage change in interannual SST variability averaged over the Niño index regions, for the MH$_{PMIP}$ and MH$_{GS}$ simulations relative to the PI.
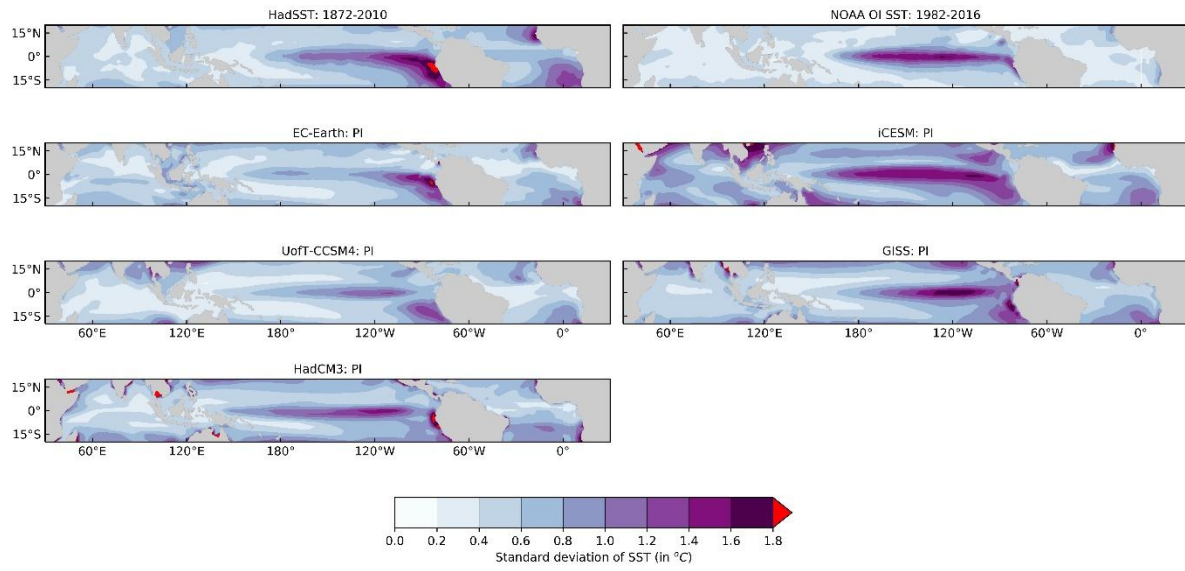
Figure B 5 Comparison of boreal winter (DJF) sea surface temperature variability over the tropical oceans shown by model PI simulations, with observational datasets.
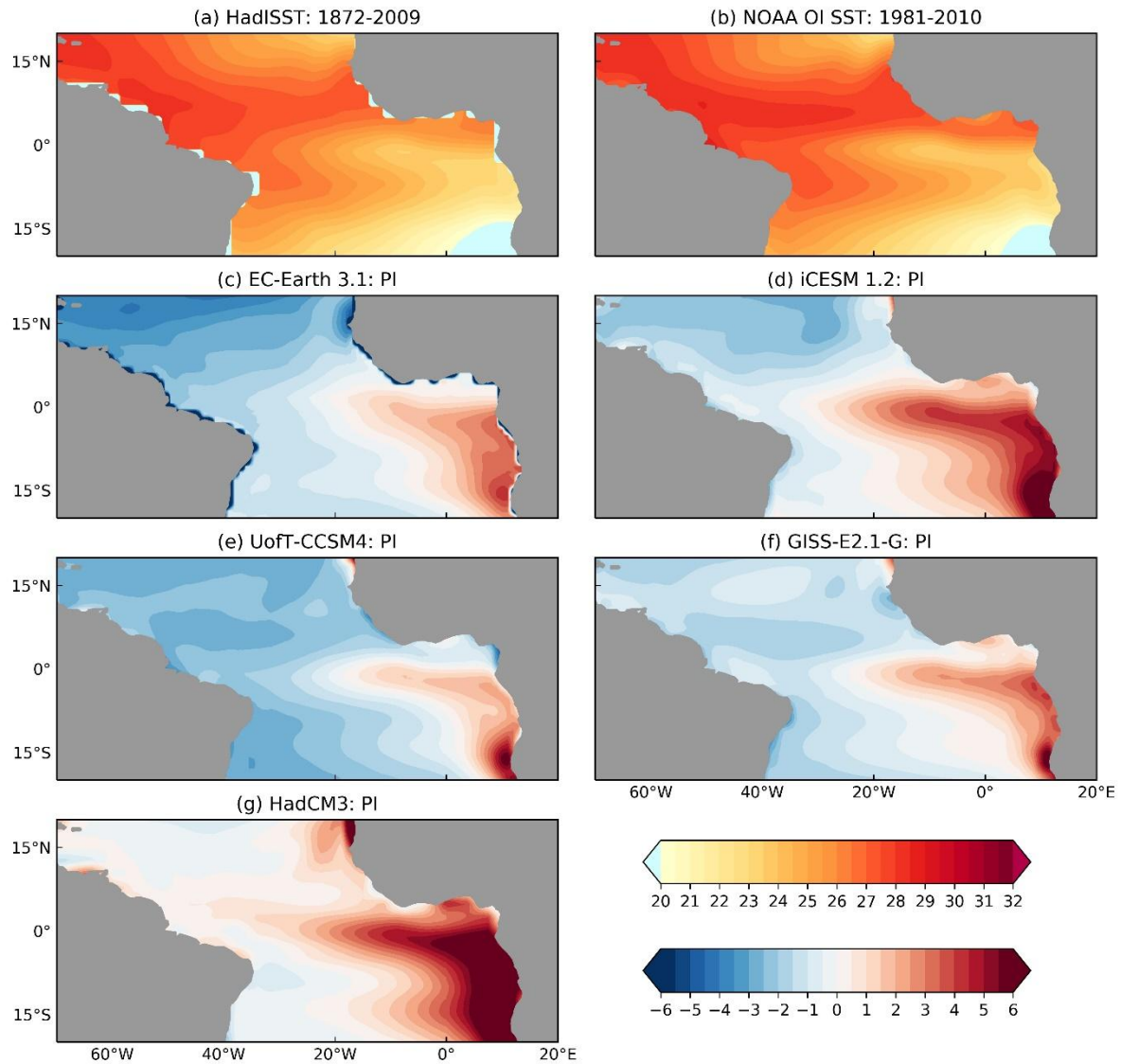
Figure B 6 (a-b) Boreal summer (JJA) sea surface temperatures over the tropical Atlantic for the present-day observational datasets (c-g) Boreal summer SST biases in model PI simulations relative to the NOAA OI SST dataset shown in (b).
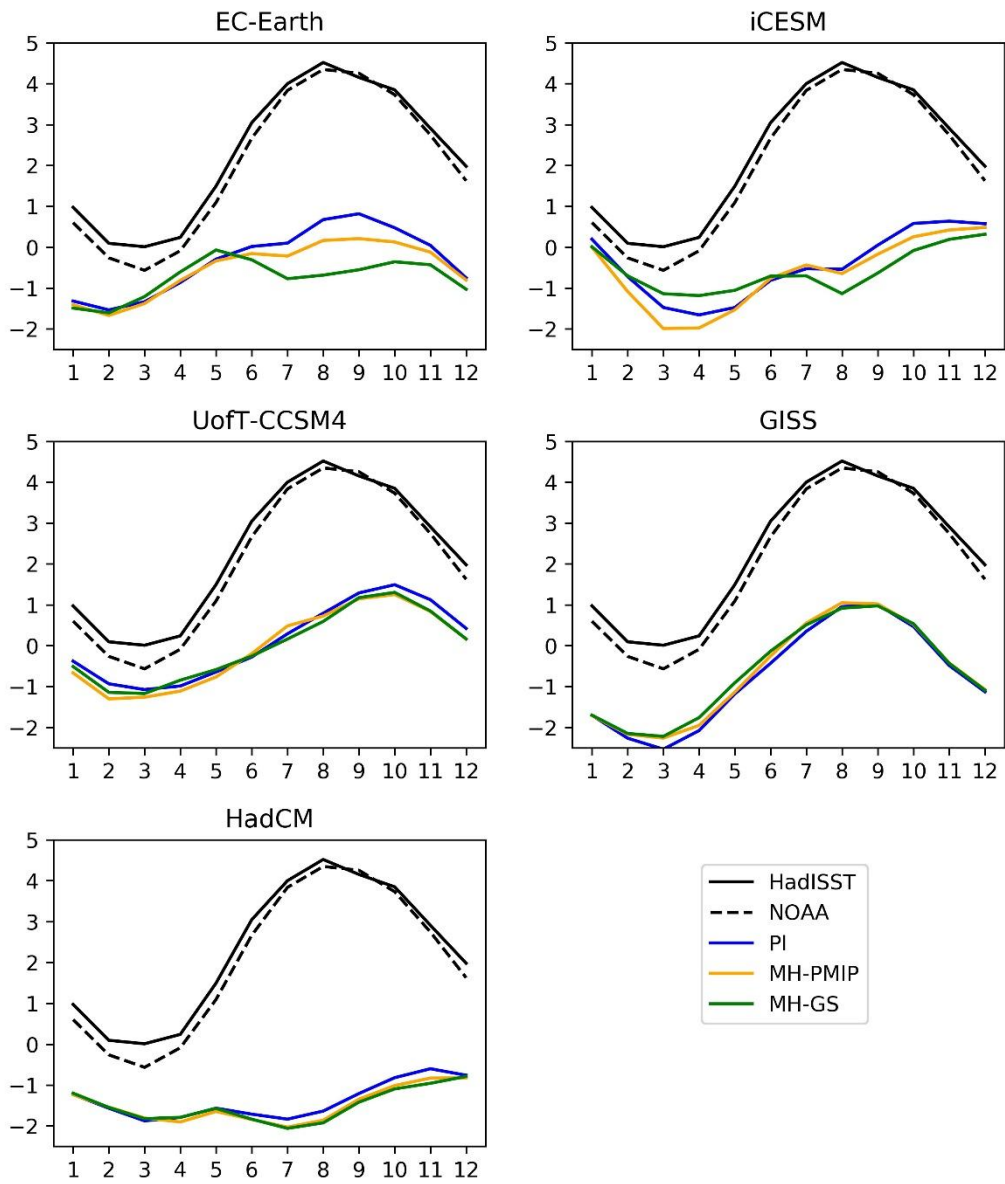
Figure B 7 Comparison of west-to-east SST gradients for the equatorial Atlantic. The SST gradient is computed as the difference between the mean SST over West Equatorial Atlantic (40-30 °W, 3 °S – 3 °N) and the East Equatorial Atlantic (0-8 °E, 10-3 °S).

Figure B 8 Changes to interannual SST variability for the tropical Atlantic (3S – 3N).
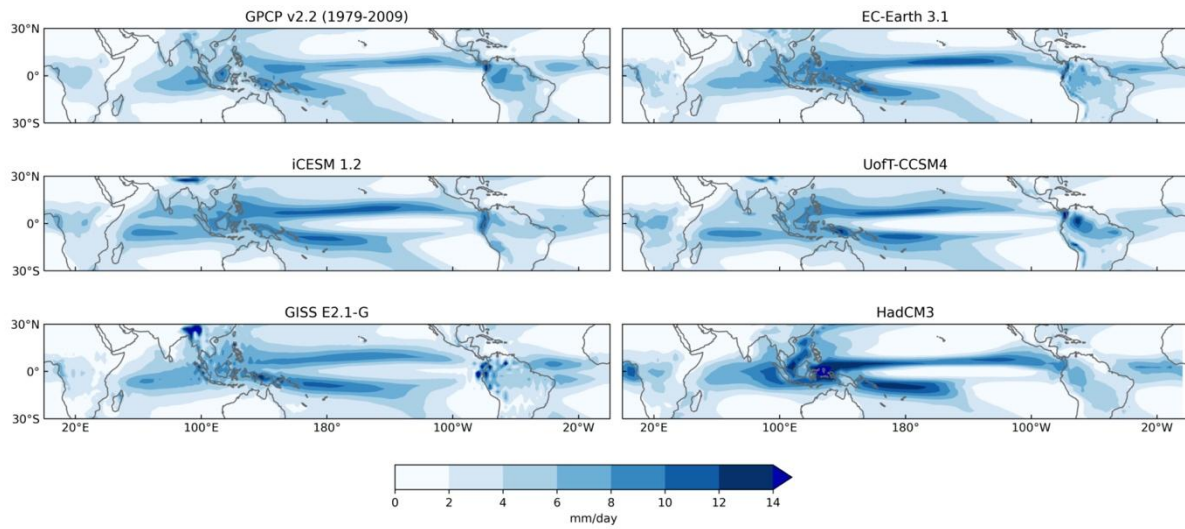
Figure B 9 Comparison of mean annual precipitation shown by model PI simulations, with observational datasets.
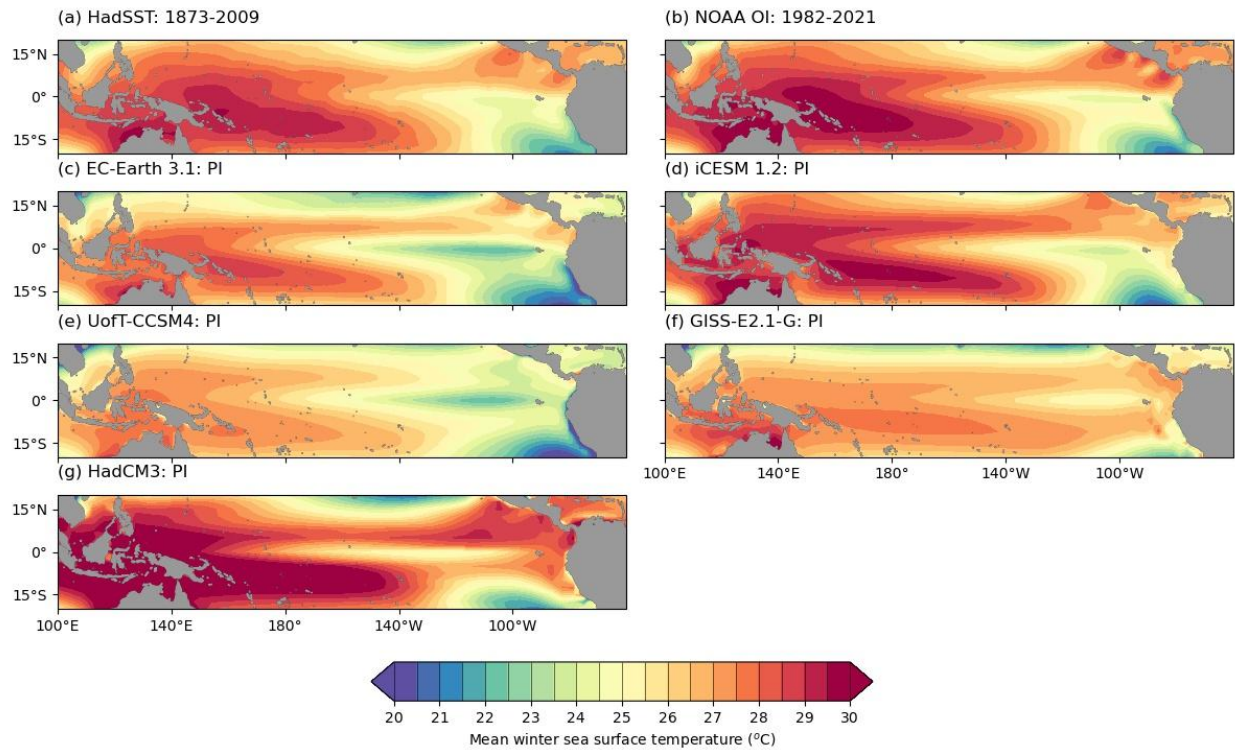
Figure B 10 Comparison of boreal winter (DJF) sea surface temperatures shown by (a-b) observations and (c-g) model simulations for the PI.

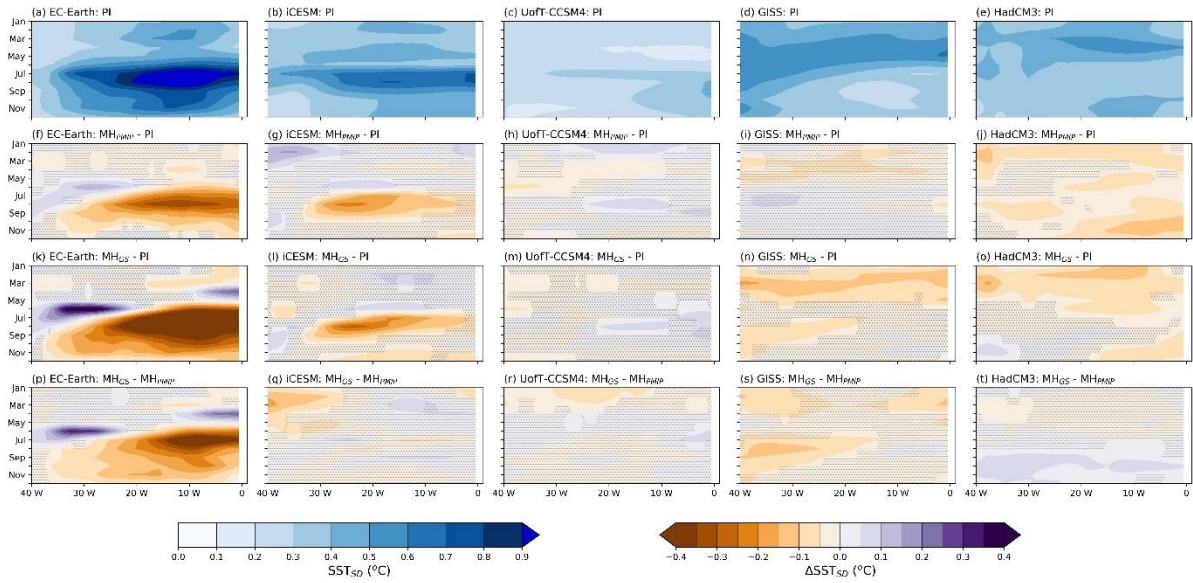|	EC-Earth 3.1	iCESM 1.2	UofT-CCSM4	GISS-E2.1-G	HadCM3
Model name	EC-Earth	Community Earth System Model	Community Climate System Model	Goddard Institute for Space Studies Model	Hadley Centre coupled model version 3
Modelling center	European Consortium	National Center for Atmospheric Research (NCAR)	NCAR model (CCSM4) modified at: University of Toronto	NASA GISS	UK Met Office
Atmospheric component	Integrated Forecast System	Community Atmosphere Model v5.3 (iCAM5)	Community Atmosphere Model v4 (CAM4)	Goddard Institute for Space Studies Model E2.1	HadAM3
Atmospheric grid	1.125 x 1.125 (62)	1.9 x 2.5 (30)	1 x 1 (26)	2 x 2.5 (40)	2.5 x 3.75 (19)
Oceanic component	Nucleus for European Modelling of the Ocean v2 (NEMO2)	Parallel Ocean Program v2.0 (POP2)	Parallel Ocean Program v2.0 (POP2)	GISS Ocean Model v1	HadCM3BL
Oceanic grid	1 x 1 (46)	1 x 1 (60)	1 x 1 (60)	1 x 1.25 (40)	1.25 x 1.25 (20)

Simulation protocols for MH simulations	CMIP5 / PMIP3	CMIP6 / PMIP4	CMIP6 / PMIP4	CMIP6 / PMIP4	CMIP6 / PMIP4
Feedbacks additionally incorporated in the MH_{GS} simulation	Vegetation, dust	Vegetation, dust, soil	Vegetation, soil, lakes	Vegetation	Vegetation
PI-to-MH albedo change over the Sahara	0.3 to 0.15	0.3 to 0.15	0.3 to 0.16	0.3 to 0.19	
Reference for simulations	Pausata et al. (2016)	Tabor et al. (2020)	Chandan and Peltier (2020)	Tiwari et al. (2023)	This paper
Total length per simulation (years)	300	350	500-1250		700
Length used for analysis (years)	200	100	100	100	200

Table B 1 Model details. Numbers in parentheses indicate number of vertical levels in the atmospheric or oceanic grid.

(a) TNI	EC-Earth	iCESM	UofT-CCSM4	GISS	HadCM3
PI	4.08	2.86	2.68	1.15	0.68
MH$_{PMIP}$	4.17	2.46	2.74	1.29	0.22
MH$_{GS}$	4.2	2.41	2.74	1.47	0.11

(b) WPG	EC-Earth	iCESM	UofT-CCSM4	GISS	HadCM3
PI	1.26	1.42	1.29	0.02	2.15
MH$_{PMIP}$	1.55	1.56	1.3	0.03	2.59
MH$_{GS}$	1.82	1.9	1.4	0	2.66

(c) EPG	EC-Earth	iCESM	UofT-CCSM4	GISS	HadCM3
PI	3.63	3.6	3.2	1.52	1.59
MH$_{PMIP}$	3.55	3.33	3.46	1.88	1.44
MH$_{GS}$	3.48	3.34	3.39	2.05	1.4

(d) ESOI	EC-Earth	iCESM	UofT-CCSM4	GISS	HadCM3
PI	1.66	2.1	3.3	-0.3	2.47
MH$_{PMIP}$	1.99	2.33	3.57	-0.06	3.07

MH$_{GS}$	2.4	2.69	4.07	0.12	3.41

Table B 2 Mean state indicators for the PI, MH$_{PMIP}$ and MH$_{GS}$ simulations: (a) Trans Niño Index (TNI), (b) West Pacific SST Gradient (WPG), (c) East Pacific SST Gradient (EPG) and (d) Equatorial Southern Oscillation Index (ESOI). All values were calculated over boreal winter (DJF).

Table B 3 List of proxy records cited in this study.

	Reference	Location	Archive
1	Moy et al. (2002)	2.77 °S, 79.23 °W	Lake sediments
2	McGregor and Gagan (2004)	3.41 °S, 143.61 °E	Corals
3	Conroy et al. (2008)	0.8 °S, 89.3 °W	Lake sediments
4	Leduc et al. (2009)	8 °N, 84 °W	Marine sediments
5	Marchitto et al. (2010)	25.2 °N, 112.7 °W	Marine sediments
6	Koutavas and Joanides (2012)	1.22 °S, 89.68 °W	Marine sediments
7	Sadekov et al. (2013)	1.6 °S, 90.42 °W	Marine sediments
8	Chen et al. (2016)	4 °N, 114 °E	Speleothem
9	White et al. (2018)	0 °N, 156 °W	Marine sediments
10	Barr et al. (2019)	27.5 °S, 153.46 °E	Lake sediments
11	Grothe et al. (2019)	2 °N, 157 °W	Corals

12	Cobb et al. (2013)	2 °N, 157 °W 4 °N, 160 °W	Corals
13	Carré et al. (2014)	7 archaeological sites on the SW Peruvian coast, between 11.7 - 18.1 °S	Mollusc middens
14	Driscoll et al. (2014)	6.5 °S, 147.5 °E	Clams
15	Duprey et al. (2012)	15.35 °S, 167.18 °E	Corals and clams
16	Thompson et al. (2017)	0.2 °S, 90.7 °W	Lake sediments
17	Tudhope et al. (2001)	6 °S, 148 °E	Corals
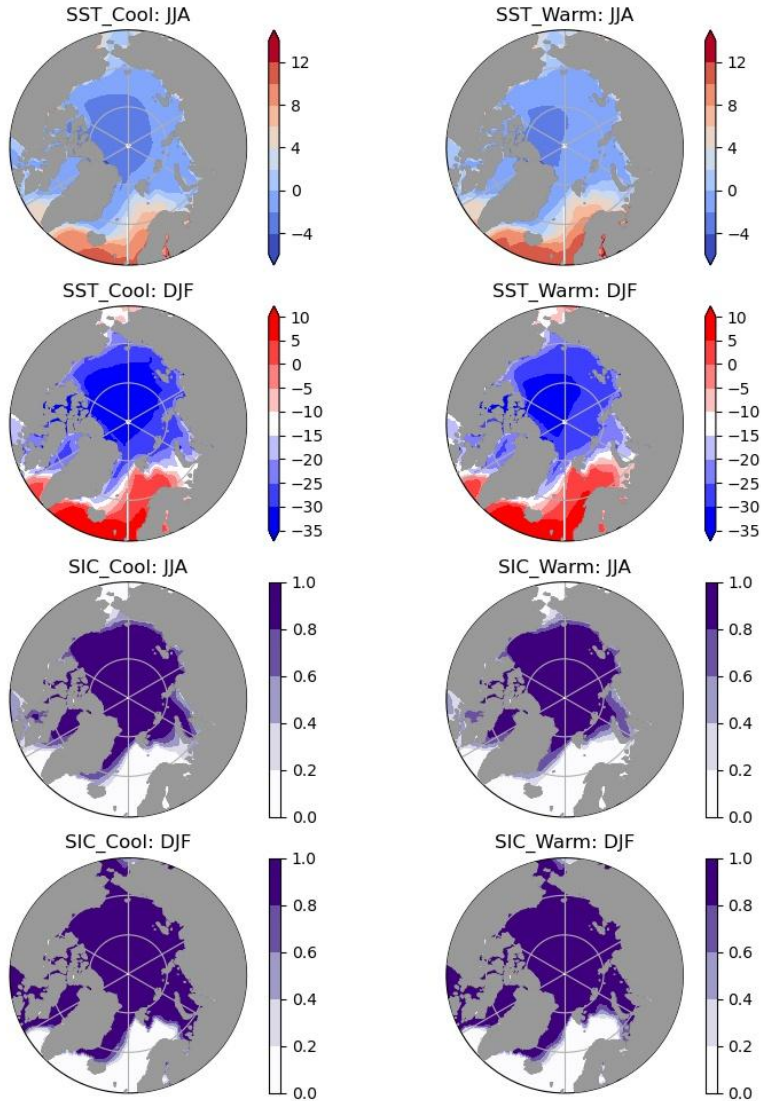
Figure C 1 Sea Surface Temperature (SST) and Sea Ice Concentration (SIC) boundary conditions for "Warm Arctic" and "Cool Arctic" experiments conducted with GEM 4.8.12; derived from outputs from EC-Earth 3.1 simulations for the mid-Holocene (details in Methods). For SST, different color maps are used to highlight the different temperature ranges for summer (JJA) and winter (DJF).
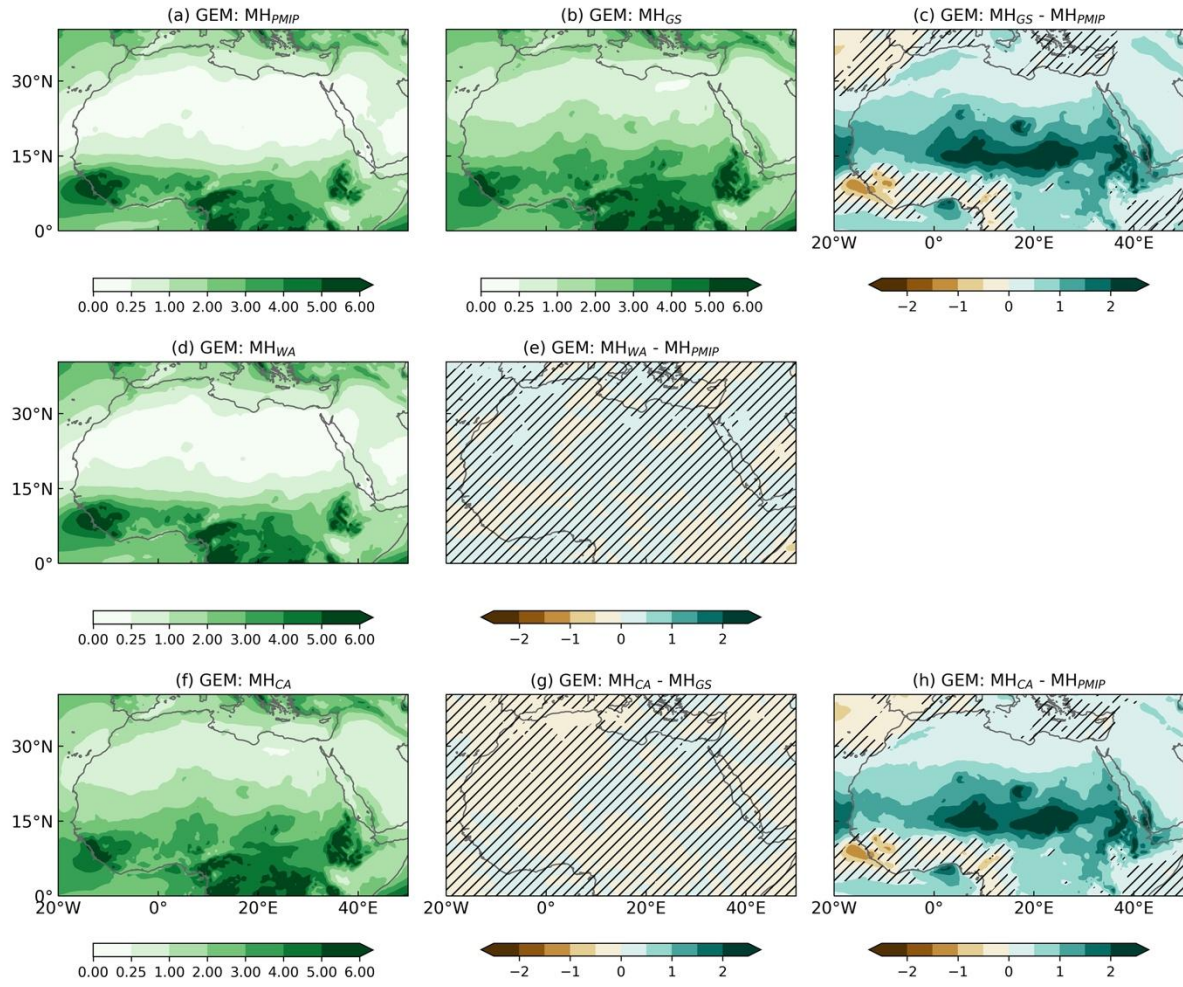
Figure C 2 Precipitation changes over northern Africa. Mean annual precipitation anomalies (in mm/day) for various GEM experiments, relative to the MH$_{PMIP}$ or MH$_{GS}$ experiment. Hatching indicates regions where anomalies were not significant at the 95% confidence level, according to Student's *t* test.
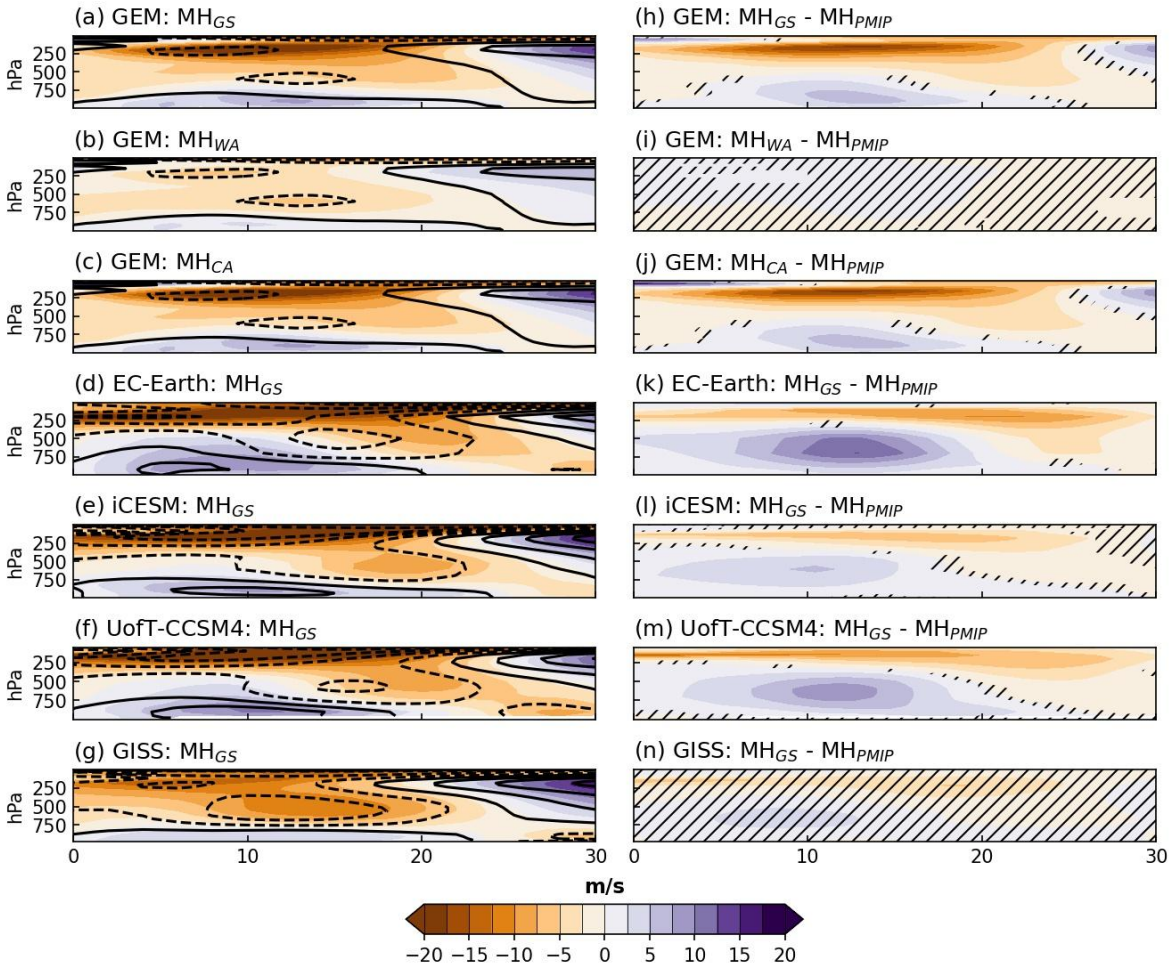
Figure C 3 Zonal wind strength (in m/s) for tropical northern Africa ($0° - 30°$ N) at $0°$ E for JJAS. Positive values indicate eastward (westerly) winds. (a-f) Colors show zonal wind strength in MH_{GS} experiments. Contours show zonal wind strength in MH_{PMIP} experiments. Contour spacing is 5m/s, dashed contours show negative values. (g-l) Colors show zonal wind strength anomalies in MH_{GS} experiments relative to the MH_{PMIP} experiments. Hatches indicate values statistically insignificant at the 95% confidence level, calculated using the Student's t test.

RÉFÉRENCES

Adkins, J., deMenocal, P., & Eshel, G. (2006). The "African humid period" and the record of marine upwelling from excess 230Th in Ocean Drilling Program Hole 658C. *Paleoceanography*, *21*(4), 1–14. https://doi.org/10.1029/2005PA001200

Adler, R. F., Huffman, G. J., Chang, A., Ferraro, R., Xie, P. P., Janowiak, J., et al. (2003). The version-2 global precipitation climatology project (GPCP) monthly precipitation analysis (1979-present). *Journal of Hydrometeorology*, *4*(6). https://doi.org/10.1175/1525-7541(2003)004<1147:TVGPCP>2.0.CO;2

Ait Brahim, Y., Wassenburg, J. A., Sha, L., Cruz, F. W., Deininger, M., Sifeddine, A., et al. (2019). North Atlantic Ice-Rafting, Ocean and Atmospheric Circulation During the Holocene: Insights From Western Mediterranean Speleothems. *Geophysical Research Letters*, *46*(13), 7614–7623. https://doi.org/10.1029/2019GL082405

Almazroui, M., Ashfaq, M., Islam, M. N., Rashid, I. U., Kamil, S., Abid, M. A., et al. (2021). Assessment of CMIP6 Performance and Projected Temperature and Precipitation Changes Over South America. *Earth Systems and Environment*, *5*(2), 155–183. https://doi.org/10.1007/s41748-021-00233-6

An, S. Il, & Choi, J. (2014). Mid-Holocene tropical Pacific climate state, annual cycle, and ENSO in PMIP2 and PMIP3. *Climate Dynamics*, *43*(3–4), 957–970. https://doi.org/10.1007/s00382-013-1880-z

Andersson, C., Pausata, F. S. R., Jansen, E., Risebrobakken, B., & Telford, R. J. (2010). Holocene trends in the foraminifer record from the Norwegian Sea and the North Atlantic Ocean. *Climate of the Past*, *6*(2), 179–193. https://doi.org/10.5194/cp-6-179-2010

Armitage, S J, Drake, N. A., Stokes, S., El-Hawat, A., Salem, M. J., White, K., et al. (2007). Multiple phases of North African humidity recorded in lacustrine sediments from the Fazzan Basin, Libyan Sahara. *Quaternary Geochronology*, *2*, 181–186. https://doi.org/10.1016/j.quageo.2006.05.019

Armitage, Simon J., Bristow, C. S., & Drake, N. A. (2015). West African monsoon dynamics inferred from abrupt fluctuations of Lake Mega-Chad. *Proceedings of the National Academy of Sciences of the United States of America*, *112*(28), 8543–8548. https://doi.org/10.1073/PNAS.1417655112/-/DCSUPPLEMENTAL

Armstrong, E., Tallavaara, M., Hopcroft, P. O., & Valdes, P. J. (2023). North African humid periods over the past 800,000 years. *Nature Communications*, *14*(1). https://doi.org/10.1038/s41467-023-41219-4

Baker, P. A., Rigsby, C. A., Seltzer, G. O., Fritz, S. C., Lowenstein, T. K., Bacher, N. P., & Veliz, C. (2001). Tropical climate changes at millennial and orbital timescales on the Bolivian Altiplano. *Nature 2001 409:6821*, *409*(6821), 698–701. https://doi.org/10.1038/35055524

Barreto, E. A. de S. (2010, May 14). *RECONSTITUIÇÃO DA PLUVIOSIDADE DA CHAPADA DIAMANTINA (BA) DURANTE O QUATERNÁRIO TARDIO ATRAVÉS DE REGISTROS ISOTÓPICOS (O E C) EM ESTALAGMITES Eline*. *Repositório USP*. Universidade de São Paulo, São Paulo. https://doi.org/10.11606/D.44.2010.TDE-24052010-183923

Bartlein, P. J., Harrison, S. P., Brewer, S., Connor, S., Davis, B. A. S., Gajewski, K., et al. (2011). Pollen-based continental climate reconstructions at 6 and 21 ka: A global synthesis. *Climate Dynamics*, *37*(3), 775–802. https://doi.org/10.1007/s00382-010-0904-1

Bigelow, N. H., Brubaker, L. B., Edwards, M. E., Harrison, S. P., Prentice, I. C., Anderson, P. M., et al. (2003). Climate change and Arctic ecosystems: 1. Vegetation changes north of 55°N between the last glacial maximum, mid-Holocene, and present. *Journal of Geophysical Research: Atmospheres*, *108*(19). https://doi.org/10.1029/2002jd002558

Binney, H., Edwards, M., Macias-Fauria, M., Lozhkin, A., Anderson, P., Kaplan, J. O., et al. (2017). Vegetation of Eurasia from the last glacial maximum to present: Key biogeographic patterns. *Quaternary Science Reviews*, *157*, 80–97. https://doi.org/10.1016/j.quascirev.2016.11.022

Braconnot, P, Joussaume, S., Marti, O., & De Noblet, N. (1999). Synergistic feedbacks from ocean and vegetation on the African monsoon response to mid-Holocene insolation. *Geophysical Research Letters*, *26*(16), 2481–2484. https://doi.org/10.1029/1999GL006047

Braconnot, P., Otto-Bliesner, B., Harrison, S., Joussaume, S., Peterchmitt, J. Y., Abe-Ouchi, A., et al. (2007). Results of PMIP2 coupled simulations of the Mid-Holocene and last glacial maximum - Part 2: Feedbacks with emphasis on the location of the ITCZ and mid- and high latitudes heat budget. *Climate of the Past*, *3*(2), 279–296. https://doi.org/10.5194/cp-3-279-2007

Braconnot, Pascale, Harrison, S. P., Kageyama, M., Bartlein, P. J., Masson-Delmotte, V., Abe-Ouchi, A., et al. (2012). Evaluation of climate models using palaeoclimatic data. *Nature Climate Change*, *2*(6), 417–424. https://doi.org/10.1038/nclimate1456

Braconnot, Pascale, Zhu, D., Marti, O., & Servonnat, J. (2019). Strengths and challenges for transient Mid- to Late Holocene simulations with dynamical vegetation. *Climate of the Past*, *15*(3), 997–1024. https://doi.org/10.5194/cp-15-997-2019

Brady, E., Stevenson, S., Bailey, D., Liu, Z., Noone, D., Nusbaumer, J., et al. (2019). The Connected Isotopic Water Cycle in the Community Earth System Model Version 1. *Journal of Advances in Modeling Earth Systems*, *11*(8), 2547–2566. https://doi.org/10.1029/2019MS001663

Brierley, C., & Wainer, I. (2018). Inter-annual variability in the tropical Atlantic from the Last Glacial Maximum into future climate projections simulated by CMIP5/PMIP3. *Climate of the Past*, *14*(10), 1377–1390. https://doi.org/10.5194/cp-14-1377-2018

Brierley, C. M., Zhao, A., Harrison, S. P., Braconnot, P., Williams, C. J. R., Thornalley, D. J. R., et al. (2020a). Large-scale features and evaluation of the PMIP4-CMIP6 midHolocene simulations. *Climate of the Past*, *16*(5), 1847–1872. https://doi.org/10.5194/cp-16-1847-2020

Brierley, C. M., Zhao, A., Harrison, S. P., Braconnot, P., Williams, C. J. R., Thornalley, D. J. R., et al. (2020b). Large-scale features and evaluation of the PMIP4-CMIP6 midHolocene simulations. *Climate of the Past*, *16*(5), 1847–1872. https://doi.org/10.5194/cp-16-1847-2020

Brown, J. R., Brierley, C. M., An, S., Guarino, M., Stevenson, S., Williams, C. J. R., et al. (2020). Comparison of past and future simulations of ENSO in. *Climate of the Past*, (February), 1777–1805.

Calvo, E., Grimalt, J., & Jansen, E. (2002). High resolution U37K sea surface temperature reconstruction in the Norwegian Sea during the Holocene. *Quaternary Science Reviews*, *21*(12–13), 1385–1394. https://doi.org/10.1016/S0277-3791(01)00096-8

Carrington, D. P., Gallimore, R. G., & Kutzbach, J. E. (2001). Climate sensitivity to wetlands and wetland vegetation in mid-Holocene North Africa. *Climate Dynamics 2001 17:2*, *17*(2), 151–157. https://doi.org/10.1007/S003820000099

Cartapanis, O., Jonkers, L., Moffa-Sanchez, P., Jaccard, S. L., & de Vernal, A. (2022). Complex spatio-temporal structure of the Holocene Thermal Maximum. *Nature Communications*, *13*(1). https://doi.org/10.1038/s41467-022-33362-1

Causse, C., Ghaleb, B., Chkir, N., Zouari, K., Ouezdou, H. Ben, & Mamou, A. (2003). Humidity changes in southern Tunisia during the Late Pleistocene inferred from U-Th dating of mollusc shells. *Applied Geochemistry*. https://doi.org/10.1016/S0883-2927(03)00043-X

Chandan, D., & Peltier, W. R. (2020). African Humid Period Precipitation Sustained by Robust Vegetation, Soil, and Lake Feedbacks. *Geophysical Research Letters*, *47*(21), 1–12. https://doi.org/10.1029/2020GL088728

Charney, J., Stone, P. H., & Quirk, W. J. (1975). Drought in the Sahara: A biogeophysical feedback mechanism. *Science*, *187*(4175), 434–435. https://doi.org/10.1126/science.187.4175.434

Cheddadi, R., Carré, M., Nourelbait, M., François, L., Rhoujjati, A., Manay, R., et al. (2021). Early Holocene greening of the Sahara requires Mediterranean winter rainfall. *Proceedings of the National Academy of Sciences of the United States of America*, *118*(23). https://doi.org/10.1073/pnas.2024898118

Chen, T. C., Weng, S. P., & Schubert, S. (1999). Maintenance of austral summertime upper-tropospheric circulation over tropical South America: The Bolivian high-Nordeste low system. *Journal of the Atmospheric Sciences*, *56*(13), 2081–2100. https://doi.org/10.1175/1520-0469(1999)056<2081:MOASUT>2.0.CO;2

Clement, A. C., Seager, R., & Cane, M. A. (2000). Suppression of El Niño during the mid-Holocene by changes in the Earth's orbit. *Paleoceanography*, *15*(6), 731–737. https://doi.org/10.1029/1999PA000466

Cobb, K. M., Westphal, N., Sayani, H. R., Watson, J. T., Lorenzo, E. Di, Cheng, H., et al. (2013). Highly Variable El-Niño-Southern Oscillation Throughout the Holocene. *Science*, *339*(January), 67–70.

Cohen, J., Screen, J. A., Furtado, J. C., Barlow, M., Whittleston, D., Coumou, D., et al. (2014). Recent Arctic amplification and extreme mid-latitude weather. *Nature Geoscience*, *7*(9), 627–637. https://doi.org/10.1038/ngeo2234

Collins, J. A., Prange, M., Caley, T., Gimeno, L., Beckmann, B., Mulitza, S., et al. (2017). Rapid termination of the African Humid Period triggered by northern high-latitude cooling. *Nature Communications*, *8*(1). https://doi.org/10.1038/s41467-017-01454-y

Conrad, G., & Lappartient, J. R. (1991). The appearance of Cardium fauna and foraminifers in the great lakes of the early quaternary period in the Algerian central Sahara desert. *Journal of African Earth Sciences (and the Middle East)*, *12*(1–2), 375–382. https://doi.org/10.1016/0899-5362(91)90086-E

Cook, K. H., Hsieh, J.-S., & Hagos, S. M. (2004). The Africa-South America intercontinental teleconnection. *Journal of Climate*, *17*(14), 2851–2865. https://doi.org/10.1175/1520-0442(2004)017<2851:TAAIT>2.0.CO;2

Crocker, A. J., Naafs, B. D. A., Westerhold, T., James, R. H., Cooper, M. J., Röhl, U., et al. (2022a). Astronomically controlled aridity in the Sahara since at least 11 million years ago. *Nature Geoscience*, *15*(8), 671–676. https://doi.org/10.1038/s41561-022-00990-7

Crocker, A. J., Naafs, B. D. A., Westerhold, T., James, R. H., Cooper, M. J., Röhl, U., et al. (2022b). Astronomically controlled aridity in the Sahara since at least 11 million years ago. *Nature Geoscience*, *15*(8), 671–676. https://doi.org/10.1038/s41561-022-00990-7

Cruz, F. W., Burns, S. J., Karmann, I., Sharp, W. D., Vuille, M., Cardoso, A. O., et al. (2005). Insolation-driven changes in atmospheric circulation over the past 116,000 years in subtropical Brazil. *Nature 2005 434:7029*, *434*(7029), 63–66. https://doi.org/10.1038/nature03365

Cruz, F. W., Vuille, M., Burns, S. J., Wang, X., Cheng, H., Werner, M., et al. (2009). Orbitally driven east-west antiphasing of South American precipitation. *Nature Geoscience*, *2*(3), 210–214. https://doi.org/10.1038/ngeo444

D'Agostino, R., Brown, J. R., Moise, A., Nguyen, H., Silva Dias, P. L., & Jungclaus, J. (2020). Contrasting southern hemisphere monsoon response: MidHolocene orbital forcing versus future greenhouse gas-induced global warming. *Journal of Climate*, *33*(22), 9595–9613. https://doi.org/10.1175/JCLI-D-19-0672.1

Dallmeyer, A., Claussen, M., Lorenz, S. J., & Shanahan, T. (2020). The end of the African humid period as seen by a transient comprehensive Earth system model simulation of the last 8000 years. *Climate of the Past*, *16*(1), 117–140. https://doi.org/10.5194/cp-16-117-2020

Dallmeyer, A., Claussen, M., Lorenz, S., Sigl, M., Toohey, M., & Herzschuh, U. (2021). Holocene vegetation transitions and their climatic drivers in MPI-ESM1.2. *Climate of the Past Discussions*, 1–55. https://doi.org/10.5194/cp-2021-51

Dallmeyer, A., Poska, A., Marquer, L., Seim, A., & Gaillard, M. J. (2023). The challenge of comparing pollen-based quantitative vegetation reconstructions with outputs from vegetation models - a European perspective. *Climate of the Past*, *19*(7), 1531–1557. https://doi.org/10.5194/CP-19-1531-2023

Dandoy, S., Pausata, F. S. R., Camargo, S. J., Laprise, R., Winger, K., & Emanuel, K. (2021). Atlantic hurricane response to Saharan greening and reduced dust emissions during the mid-Holocene. *Climate of the Past*, *17*(2), 675–701. https://doi.org/10.5194/cp-17-675-2021

Davies, F. J., Renssen, H., Blaschek, M., & Muschitiello, F. (2015). The impact of sahara desertification on arctic cooling during the holocene. *Climate of the Past*, *11*(3), 571–586. https://doi.org/10.5194/cp-11-571-2015

deMenocal, P., Ortiz, J., Guilderson, T., Adkins, J., Sarnthein, M., Baker, L., & Yarusinsky, M. (2000). Abrupt onset and termination of the African Humid Period: rapid climate responses to gradual insolation forcing. *Quaternary Science Reviews*.

DeMenocal, P., Ortiz, J., Guilderson, T., & Sarnthein, M. (2000). Coherent high- and low-latitude climate variability during the holocene warm period. *Science*, *288*(5474), 2198–2202. https://doi.org/10.1126/science.288.5474.2198

Dias, C. G., & Reboita, M. S. (2021). Assessment of CMIP6 Simulations over Tropical South America. *Revista Brasileira de Geografia Física*, *14*(3), 1282–1295. https://doi.org/10.26848/RBGF.V14.3.P1282-1295

Drake, N. A., Breeze, P., & Parker, A. (2013). Palaeoclimate in the Saharan and Arabian Deserts during the Middle Palaeolithic and the potential for hominin dispersals. *Quaternary International*, *300*, 48–61. https://doi.org/10.1016/j.quaint.2012.12.018

Dupont, L. M., Jahns, S., Marret, F., & Ning, S. (2000). Vegetation change in equatorial West Africa: Time-slices for the last 150 ka. *Palaeogeography, Palaeoclimatology, Palaeoecology*, *155*(1–2), 95–122. https://doi.org/10.1016/S0031-0182(99)00095-4

Emile-Geay, J., Cobb, K. M., Carre, M., Braconnot, P., Leloup, J., Zhou, Y., et al. (2016). Links between tropical Pacific seasonal, interannual and orbital variability during the Holocene. *Nature Geoscience*, *9*(2), 168–173. https://doi.org/10.1038/ngeo2608

England, J. H., Lakeman, T. R., Lemmen, D. S., Bednarski, J. M., Stewart, T. G., & Evans, D. J. A. (2008). A millennial-scale record of Arctic Ocean sea ice variability and the demise of the Ellesmere Island ice shelves. *Geophysical Research Letters*, *35*(19), 2–6. https://doi.org/10.1029/2008GL034470

Falardeau, J., de Vernal, A., & Spielhagen, R. F. (2018). Paleoceanography of northeastern Fram Strait since the last glacial maximum: Palynological evidence of large amplitude changes. *Quaternary Science Reviews*, *195*, 133–152. https://doi.org/10.1016/j.quascirev.2018.06.030

Francis, J. A., & Vavrus, S. J. (2012). Evidence linking Arctic amplification to extreme weather in mid-latitudes. *Geophysical Research Letters*, *39*(6), 1–6. https://doi.org/10.1029/2012GL051000

Fréchette, B., & De Vernal, A. (2009). Relationship between holocene climate variations over Southern Greenland and Eastern Baffin Island and synoptic circulation pattern. *Climate of the Past*, *5*(3), 347–359. https://doi.org/10.5194/cp-5-347-2009

Gaetani, M., Pohl, B., Douville, H., & Fontaine, B. (2011). West African Monsoon influence on the summer Euro-Atlantic circulation. *Geophysical Research Letters*, *38*(9), 38–42. https://doi.org/10.1029/2011GL047150

Gaetani, M., Messori, G., Pausata, F. S. R., Tiwari, S., & Alvarez, M. C. (2024). Mid-Holocene climate at mid-latitudes : assessing the impact of the Saharan greening, (February), 1–37. Retrieved from https://egusphere.copernicus.org/preprints/2024/egusphere-2024-272/

Gandu, A. W., & Silva Dias, P. L. (1998). Impact of tropical heat sources on the South American tropospheric upper circulation and subsidence. *Journal of Geophysical Research: Atmospheres*, *103*(D6), 6001–6015. https://doi.org/10.1029/97JD03114

Garreaud, R. D., Vuille, M., Compagnucci, R., & Marengo, J. (2009). Present-day South American climate. *Palaeogeography, Palaeoclimatology, Palaeoecology*, *281*(3–4), 180–195. https://doi.org/10.1016/j.palaeo.2007.10.032

Gasse, F. (2000). Hydrological changes in the African tropics since the Last Glacial Maximum. *Quaternary Science Reviews*, *19*(1–5), 189–211. https://doi.org/10.1016/S0277-3791(99)00061-X

Gasse, F. (2002). Diatom-inferred salinity and carbonate oxygen isotopes in Holocene waterbodies of the western Sahara and Sahel (Africa). *Quaternary Science Reviews*, *21*(7), 737–767. https://doi.org/10.1016/S0277-3791(01)00125-1

Gibb, O. T., Steinhauer, S., Fréchette, B., de Vernal, A., & Hillaire-Marcel, C. (2015). Diachronous evolution of sea surface conditions in the labrador sea and baffin bay since the last deglaciation. *Holocene*, *25*(12), 1882–1897. https://doi.org/10.1177/0959683615591352

Girard, C., Plante, A., Desgagné, M., Mctaggart-Cowan, R., Côté, J., Charron, M., et al. (2014). Staggered vertical discretization of the canadian environmental multiscale (GEM) model using a coordinate of

the log-hydrostatic-pressure type. *Monthly Weather Review*, *142*(3), 1183–1196. https://doi.org/10.1175/MWR-D-13-00255.1

Gorenstein, I., Prado, L. F., Bianchini, P. R., Wainer, I., Griffiths, M. L., Pausata, F. S. R., & Yokoyama, E. (2022). A fully calibrated and updated mid-Holocene climate reconstruction for Eastern South America. *Quaternary Science Reviews*, *292*, 107646. https://doi.org/10.1016/j.quascirev.2022.107646

Griffiths, M. L., Johnson, K. R., Pausata, F. S. R., White, J. C., Henderson, G. M., Wood, C. T., et al. (2020). End of Green Sahara amplified mid- to late Holocene megadroughts in mainland Southeast Asia. *Nature Communications*, *11*(1), 1–12. https://doi.org/10.1038/s41467-020-17927-6

Grimm, A. M., Pal, J. S., & Giorgi, F. (2007). Connection between spring conditions and peak summer monsoon rainfall in South America: Role of soil moisture, surface temperature, and topography in eastern Brazil. *Journal of Climate*, *20*(24), 5929–5945. https://doi.org/10.1175/2007JCLI1684.1

Grothe, P. R., Cobb, K. M., Liguori, G., Di Lorenzo, E., Capotondi, A., Lu, Y., et al. (2020). Enhanced El Niño–Southern Oscillation Variability in Recent Decades. *Geophysical Research Letters*, *47*(7), 1–8. https://doi.org/10.1029/2019GL083906

Hargreaves, J. C., Annan, J. D., Ohgaito, R., Paul, A., & Abe-Ouchi, A. (2013). Skill and reliability of climate model ensembles at the last glacial maximum and mid-holocene. *Climate of the Past*, *9*(2), 811–823. https://doi.org/10.5194/CP-9-811-2013

Harrison, S. P., Kutzbach, J. E., Liu, Z., Bartlein, P. J., Otto-Bliesner, B., Muhs, D., et al. (2003). Mid-Holocene climates of the Americas: A dynamical response to changed seasonality. *Climate Dynamics*, *20*(7–8), 663–688. https://doi.org/10.1007/S00382-002-0300-6

Haug, G. H., Hughen, K. A., Sigman, D. M., Peterson, L. C., & Röhl, U. (2001). Southward migration of the intertropical convergence zone through the holocene. *Science*, *293*(5533), 1304–1308. https://doi.org/10.1126/SCIENCE.1059725/SUPPL_FILE/1059725S1_THUMB.GIF

Hazeleger, W., Severijns, C., Semmler, T., Ştefănescu, S., Yang, S., Wang, X., et al. (2010). EC-Earth: A seamless Earth-system prediction approach in action. *Bulletin of the American Meteorological Society*, *91*(10), 1357–1363. https://doi.org/10.1175/2010BAMS2877.1

Hély, C., Lézine, A. M., Ballouche, A., Cour, P., Duzer, D., Guinet, P., et al. (2014). Holocene changes in African vegetation: Tradeoff between climate and water availability. *Climate of the Past*, *10*(2), 681–686. https://doi.org/10.5194/cp-10-681-2014

Hoelzmann, P., Jolly, D., Harrison, S. P., Laarif, F., Bonnefille, R., & Pachur, H. J. (1998). Mid-Holocene land-surface conditions in northern Africa and the Arabian peninsula: A data set for the analysis of biogeophysical feedbacks in the climate system. *Global Biogeochemical Cycles*, *12*(1), 35–51. https://doi.org/10.1029/97GB02733

Hopcroft, P. O., & Valdes, P. J. (2021). Paleoclimate-conditioning reveals a North Africa land-atmosphere tipping point. *Proceedings of the National Academy of Sciences of the United States of America*, *118*(45), 1–7. https://doi.org/10.1073/pnas.2108783118

Huo, Y., Peltier, W. R., & Chandan, D. (2021). Mid-Holocene monsoons in South and Southeast Asia: Dynamically downscaled simulations and the influence of the Green Sahara. *Climate of the Past*, *17*(4), 1645–1664. https://doi.org/10.5194/cp-17-1645-2021

Ingrosso, R., & Pausata, F. S. R. (2024). Contrasting consequences of the Great Green Wall: Easing aridity while increasing heat extremes. *One Earth*, *7*(3), 455–472. https://doi.org/10.1016/j.oneear.2024.01.017

Jaouadi, S., Lebreton, V., Bout-Roumazeilles, V., Siani, G., Lakhdar, R., Boussoffara, R., et al. (2016). Environmental changes, climate and anthropogenic impact in south-east Tunisia during the last 8 kyr. *Clim. Past*, *12*, 1339–1359. https://doi.org/10.5194/cp-12-1339-2016

Jimenez-Moreno, G., Scott Anderson, R., Ramos-Roman, M. J., Camuera, J., Manuel Mesa-Fernandez, J., García-Alix, A., et al. (2020). The Holocene Cedrus pollen record from Sierra Nevada (S Spain), a proxy for climate change in N Africa. https://doi.org/10.1016/j.quascirev.2020.106468

Kageyama, M., Braconnot, P., Harrison, S. P., Haywood, A. M., Jungclaus, J. H., Otto-Bliesner, B. L., et al. (2018). The PMIP4 contribution to CMIP6 - Part 1: Overview and over-arching analysis plan. *Geoscientific Model Development*, *11*(3), 1033–1057. https://doi.org/10.5194/gmd-11-1033-2018

Kandiano, E. S., & Bauch, H. A. (2002). Implications of planktic foraminiferal size fractions for the glacial-interglacial paleoceanography of the polar North Atlantic. *Journal of Foraminiferal Research*, *32*(3), 245–251. https://doi.org/10.2113/32.3.245

Kaufman, D., McKay, N., Routson, C., Erb, M., Davis, B., Heiri, O., et al. (2020). A global database of Holocene paleotemperature records. *Scientific Data*, *7*(1), 1–34. https://doi.org/10.1038/s41597-020-0445-3

Kaufman, D. S., & Broadman, E. (2023, February 16). Revisiting the Holocene global temperature conundrum. *Nature*. https://doi.org/10.1038/s41586-022-05536-w

Kelley, M., Schmidt, G. A., Nazarenko, L. S., Bauer, S. E., Ruedy, R., Russell, G. L., et al. (2020). GISS-E2.1: Configurations and Climatology. *Journal of Advances in Modeling Earth Systems*, *12*(8). https://doi.org/10.1029/2019MS002025

Kim, J. E., Laguë, M. M., Pennypacker, S., Dawson, E., & Swann, A. L. S. (2020). Evaporative Resistance is of Equal Importance as Surface Albedo in High-Latitude Surface Temperatures Due to Cloud Feedbacks. *Geophysical Research Letters*, *47*(4), 1–10. https://doi.org/10.1029/2019GL085663

Kröpelin, S., Verschuren, D., Lézine, A. M., Eggermont, H., Cocquyt, C., Francus, P., et al. (2008). Climate-driven ecosystem succession in the Sahara: The past 6000 years. *Science*, *320*(5877), 765–768. https://doi.org/10.1126/science.1154913

Kutzbach, J. E., Guan, J., He, F., Cohen, A. S., Orland, I. J., & Chen, G. (2020). African climate response to orbital and glacial forcing in 140,000-y simulation with implications for early modern human environments. *Proceedings of the National Academy of Sciences of the United States of America*, *117*(5), 2255–2264. https://doi.org/10.1073/pnas.1917673117

Lafore, J. P., Flamant, C., Guichard, F., Parker, D. J., Bouniol, D., Fink, A. H., et al. (2011). Progress in understanding of weather systems in West Africa. *Atmospheric Science Letters*, *12*(1), 7–12. https://doi.org/10.1002/asl.335

Larocca, L. J., & Axford, Y. (2022). Arctic glaciers and ice caps through the Holocene:a circumpolar synthesis of lake-based reconstructions. *Climate of the Past*, *18*(3), 579–606. https://doi.org/10.5194/cp-18-579-2022

Larrasoaña, J. C., Roberts, A. P., & Rohling, E. J. (2013). Dynamics of Green Sahara Periods and Their Role in Hominin Evolution. *PLoS ONE*, *8*(10). https://doi.org/10.1371/journal.pone.0076514

Larsen, D. J., Miller, G. H., Geirsdóttir, Á., & Ólafsdóttir, S. (2012). Non-linear Holocene climate evolution in the North Atlantic: A high-resolution, multi-proxy record of glacier activity and environmental change from Hvítárvatn, central Iceland. *Quaternary Science Reviews*, *39*, 14–25. https://doi.org/10.1016/j.quascirev.2012.02.006

Lavaysse, C., Flamant, C., Janicot, S., Parker, D. J., Lafore, J. P., Sultan, B., & Pelon, J. (2009). Seasonal evolution of the West African heat low: A climatological perspective. *Climate Dynamics*, *33*(2–3), 313–330. https://doi.org/10.1007/s00382-009-0553-4

Lenters, J. D., & Cook, K. H. (1997). On the origin of the Bolivian high and related circulation features of the South American climate. *Journal of the Atmospheric Sciences*, *54*(5), 656–677. https://doi.org/10.1175/1520-0469(1997)054<0656:otootb>2.0.co;2

Levis, S., Bonan, G. B., & Bonfils, C. (2004). Soil feedback drives the mid-Holocene North African monsoon northward in fully coupled CCSM2 simulations with a dynamic vegetation model. *Climate Dynamics*, *23*(7–8), 791–802. https://doi.org/10.1007/s00382-004-0477-y

Lézine, A. M., Duplessy, J. C., & Cazet, J. P. (2005). West African monsoon variability during the last deglaciation and the Holocene: Evidence from fresh water algae, pollen and isotope data from core KW31, Gulf of Guinea. *Palaeogeography, Palaeoclimatology, Palaeoecology*, *219*(3–4), 225–237. https://doi.org/10.1016/j.palaeo.2004.12.027

Lézine, A. M., Hély, C., Grenier, C., Braconnot, P., & Krinner, G. (2011). Sahara and Sahel vulnerability to climate changes, lessons from Holocene hydrological data. *Quaternary Science Reviews*, *30*(21–22), 3001–3012. https://doi.org/10.1016/j.quascirev.2011.07.006

Liu, X., & Battisti, D. S. (2015). The influence of orbital forcing of tropical insolation on the climate and isotopic composition of precipitation in South America. *Journal of Climate*, *28*(12), 4841–4862. https://doi.org/10.1175/JCLI-D-14-00639.1

Liu, Z., Kutzbach, J., & Wu, L. (2000). Modeling climate shift of El Nino variability in the Holocene. *Geophysical Research Letters*, *27*(15), 2265–2268. https://doi.org/10.1029/2000GL011452

Liu, Zhengyu, Zhu, J., Rosenthal, Y., Zhang, X., Otto-Bliesner, B. L., Timmermann, A., et al. (2014). The Holocene temperature conundrum. *Proceedings of the National Academy of Sciences of the United States of America*, *111*(34). https://doi.org/10.1073/pnas.1407229111

Marengo, J. A., Liebmann, B., Grimm, A. M., Misra, V., Silva Dias, P. L., Cavalcanti, I. F. A., et al. (2012). Recent developments on the South American monsoon system. *International Journal of Climatology*, *32*(1), 1–21. https://doi.org/10.1002/joc.2254

Marret, F., Kim, S. Y., & Scourse, J. (2013). A 30,000yr record of land-ocean interaction in the eastern Gulf of Guinea. *Quaternary Research (United States)*, *80*(1), 1–8. https://doi.org/10.1016/j.yqres.2013.04.003

McGee, D., deMenocal, P. B., Winckler, G., Stuut, J. B. W., & Bradtmiller, L. I. (2013). The magnitude, timing and abruptness of changes in North African dust deposition over the last 20,000 yr. *Earth and Planetary Science Letters*, *371–372*, 163–176. https://doi.org/10.1016/j.epsl.2013.03.054

McGregor, H. V., & Gagan, M. K. (2004). Western Pacific coral δ18O records of anomalous Holocene variability in the El Niño-Southern Oscillation. *Geophysical Research Letters*, *31*(11), 1–4. https://doi.org/10.1029/2004GL019972

McKay, N. P., Kaufman, D. S., Routson, C. C., Erb, M. P., & Zander, P. D. (2018). The Onset and Rate of Holocene Neoglacial Cooling in the Arctic. *Geophysical Research Letters*, *45*(22), 12,487-12,496. https://doi.org/10.1029/2018GL079773

McTaggart-Cowan, R., Vaillancourt, P. A., Zadra, A., Chamberland, S., Charron, M., Corvec, S., et al. (2019). Modernization of Atmospheric Physics Parameterization in Canadian NWP. *Journal of Advances in Modeling Earth Systems*, *11*(11), 3593–3635. https://doi.org/10.1029/2019MS001781

Menviel, L., Govin, A., Avenas, A., Meissner, K. J., Grant, K. M., & Tzedakis, P. C. (2021). Drivers of the evolution and amplitude of African Humid Periods. *Communications Earth & Environment*, *2*(1). https://doi.org/10.1038/s43247-021-00309-1

Moura, A. D., & Shukla, J. (1981). On the Dynamics of Droughts in Northeast Brazil: Observations, Theory and Numerical Experiments with a General Circulation Model. *Journal of the Atmospheric Sciences*. Retrieved from https://www.ptonline.com/articles/how-to-get-better-mfi-results

Muschitiello, F., Zhang, Q., Sundqvist, H. S., Davies, F. J., & Renssen, H. (2015). Arctic climate response to the termination of the African Humid Period. *Quaternary Science Reviews*, *125*, 91–97. https://doi.org/10.1016/j.quascirev.2015.08.012

Nicholson, S. E. (2009). A revised picture of the structure of the "monsoon" and land ITCZ over West Africa. *Climate Dynamics*, *32*(7–8), 1155–1171. https://doi.org/10.1007/s00382-008-0514-3

Nicholson, S. E. (2013). The West African Sahel: A Review of Recent Studies on the Rainfall Regime and Its Interannual Variability. *ISRN Meteorology*, *2013*, 1–32. https://doi.org/10.1155/2013/453521

Novello, V. F., Cruz, F. W., Vuille, M., Stríkis, N. M., Edwards, R. L., Cheng, H., et al. (2017). A high-resolution history of the South American Monsoon from Last Glacial Maximum to the Holocene. *Scientific Reports*, *7*(February), 1–8. https://doi.org/10.1038/srep44267

O'Ishi, R., & Abe-Ouchi, A. (2011). Polar amplification in the mid-Holocene derived from dynamical vegetation change with a GCM. *Geophysical Research Letters*, *38*(14). https://doi.org/10.1029/2011GL048001

Okumura, Y., & Xie, S. P. (2004). Interaction of the Atlantic equatorial cold tongue and the African monsoon. *Journal of Climate*, *17*(18), 3589–3602. https://doi.org/10.1175/1520-0442(2004)017<3589:IOTAEC>2.0.CO;2

O'Neill, B. C., Tebaldi, C., Van Vuuren, D. P., Eyring, V., Friedlingstein, P., Hurtt, G., et al. (2016). The Scenario Model Intercomparison Project (ScenarioMIP) for CMIP6. *Geoscientific Model Development*, *9*(9), 3461–3482. https://doi.org/10.5194/gmd-9-3461-2016

Orrison, R., Vuille, M., Smerdon, J. E., Apaestegui, J., Azevedo, V., Campos, J. L. P. S., et al. (2022). South American Summer Monsoon variability over the last millennium in paleoclimate records and isotope-enabled climate models. *Climate of the Past*, *18*(9), 2045–2062. https://doi.org/10.5194/cp-18-2045-2022

Otterman, J. (1974). Baring high-albedo soils by overgrazing: A hypothesized desertification mechanism. *Science*. https://doi.org/10.1126/science.186.4163.531

Otto-Bliesner, B., Braconnot, P., Harrison, S., Lunt, D., Abe-Ouchi, A., Albani, S., et al. (2017). The PMIP4 contribution to CMIP6 – Part 2: Two Interglacials, Scientific Objective and Experimental Design for Holocene and Last Interglacial Simulations. *Geoscientific Model Development Discussions*, 1–36. https://doi.org/10.5194/gmd-2016-279

Otto-Bliesner, B. L., Brady, E. C., Shin, S. I., Liu, Z., & Shields, C. (2003). Modeling El Niño and its tropical teleconnections during the last glacial-interglacial cycle. *Geophysical Research Letters*, *30*(23), 2–5. https://doi.org/10.1029/2003GL018553

Pachur, H. J., & Rottinger, F. (1997). Evidence for a large extended paleolake in the Eastern Sahara as revealed by spaceborne radar lab images. *Remote Sensing of Environment*, *61*(3), 437–440. https://doi.org/10.1016/S0034-4257(96)00210-6

Palchan, D., & Torfstein, A. (2019). A drop in Sahara dust fluxes records the northern limits of the African Humid Period. *Nature Communications*, *10*(1). https://doi.org/10.1038/s41467-019-11701-z

Patton, H., Hubbard, A., Andreassen, K., Auriac, A., Whitehouse, P. L., Stroeven, A. P., et al. (2017). Deglaciation of the Eurasian ice sheet complex. *Quaternary Science Reviews*, *169*, 148–172. https://doi.org/10.1016/j.quascirev.2017.05.019

Pausata, F. S. R., Messori, G., & Zhang, Q. (2016). Impacts of dust reduction on the northward expansion of the African monsoon during the Green Sahara period. *Earth and Planetary Science Letters*, *434*, 298–307. https://doi.org/10.1016/j.epsl.2015.11.049

Pausata, F. S. R., Zhang, Q., Muschitiello, F., Lu, Z., Chafik, L., Niedermeyer, E. M., et al. (2017). Greening of the Sahara suppressed ENSO activity during the mid-Holocene. *Nature Communications*, *8*(May). https://doi.org/10.1038/ncomms16020

Pausata, F. S. R., Emanuel, K. A., Chiacchio, M., Diro, G. T., Zhang, Q., Sushama, L., et al. (2017). Tropical cyclone activity enhanced by Sahara greening and reduced dust emissions during the African Humid Period. *Proceedings of the National Academy of Sciences*, *114*(24), 6221–6226. https://doi.org/10.1073/pnas.1619111114

Pausata, F. S. R., Gaetani, M., Messori, G., Berg, A., Maia de Souza, D., Sage, R. F., & DeMenocal, P. B. (2020). The Greening of the Sahara: Past Changes and Future Implications. *One Earth*, *2*(3), 235–250. https://doi.org/10.1016/j.oneear.2020.03.002

Peltier, W. R., & Vettoretti, G. (2014). Dansgaard-Oeschger oscillations predicted in a comprehensive model of glacial climate: A "kicked" salt oscillator in the Atlantic. *Geophysical Research Letters*, *41*(20), 7306–7313. https://doi.org/10.1002/2014GL061413

Piao, J., Chen, W., Wang, L., Pausata, F. S. R., & Zhang, Q. (2020). Northward extension of the East Asian summer monsoon during the mid-Holocene. *Global and Planetary Change*, *184*(October 2019), 103046. https://doi.org/10.1016/j.gloplacha.2019.103046

Poan, D. E., Lafore, J. P., Roehrig, R., & Couvreux, F. (2015). Internal processes within the African Easterly Wave system. *Quarterly Journal of the Royal Meteorological Society*, *141*(689), 1121–1136. https://doi.org/10.1002/qj.2420

Poan, E. D., Gachon, P., Dueymes, G., Diaconescu, E., Laprise, R., & Seidou Sanda, I. (2016). West African monsoon intraseasonal activity and its daily precipitation indices in regional climate models: diagnostics and challenges. *Climate Dynamics*, *47*(9–10), 3113–3140. https://doi.org/10.1007/s00382-016-3016-8

Prado, L. F., Wainer, I., & Chiessi, C. M. (2013). Mid-Holocene PMIP3/CMIP5 model results: Intercomparison for the South American Monsoon System. *Holocene*, *23*(12), 1915–1920. https://doi.org/10.1177/0959683613505336

Pu, B., & Cook, K. H. (2012). Role of the west African westerly jet in sahel rainfall variations. *Journal of Climate*, *25*(8), 2880–2896. https://doi.org/10.1175/JCLI-D-11-00394.1

Quade, J., Dente, E., Armon, M., Dor, B., Morin, E., Adam, O., & Enzel, Y. (2018). Megalakes in the Sahara? A Review, *90*, 253–275. https://doi.org/10.1017/qua.2018.46

Rachmayani, R., Prange, M., & Schulz, M. (2015). North African vegetation-precipitation feedback in early and mid-Holocene climate simulations with CCSM3-DGVM. *Climate of the Past*, *11*(2), 175–185. https://doi.org/10.5194/CP-11-175-2015

Rohling, E. J., & Pälike, H. (2005). Centennial-scale climate cooling with a sudden cold event around 8,200 years ago. *Nature 2005 434:7036*, *434*(7036), 975–979. https://doi.org/10.1038/nature03421

Roubeix, V., & Chalié, F. (2019). New insights into the termination of the African Humid Period (5.5 ka BP) in central Ethiopia from detailed analysis of a diatom record. *Journal of Paleolimnology*, *61*(1), 99–110. https://doi.org/10.1007/s10933-018-0047-7

Routson, C. C., McKay, N. P., Kaufman, D. S., Erb, M. P., Goosse, H., Shuman, B. N., et al. (2019). Mid-latitude net precipitation decreased with Arctic warming during the Holocene. *Nature*, *568*(7750), 83–87. https://doi.org/10.1038/s41586-019-1060-3

Sha, L., Ait Brahim, Y., Wassenburg, J. A., Yin, J., Peros, M., Cruz, F. W., et al. (2019). How Far North Did the African Monsoon Fringe Expand During the African Humid Period? Insights From Southwest

Moroccan Speleothems. *Geophysical Research Letters*, *46*(23), 14093–14102. https://doi.org/10.1029/2019GL084879

Shanahan, T. M., Mckay, N. P., Hughen, K. A., Overpeck, J. T., Otto-Bliesner, B., Heil, C. W., et al. (2015). The time-transgressive termination of the African humid period. *Nature Geoscience*, *8*(2), 140–144. https://doi.org/10.1038/ngeo2329

Shi, X., Werner, M., Pausata, F. S. R., Yang, H., Liu, J., D'Agostino, R., et al. (2024). On the length and intensity of the West African summer monsoon during the last interglacial African humid period. *Quaternary Science Reviews*, *328*(January), 108542. https://doi.org/10.1016/j.quascirev.2024.108542

Shimizu, M. H., Sampaio, G., Venancio, I. M., & Maksic, J. (2020). Seasonal changes of the South American monsoon system during the Mid-Holocene in the CMIP5 simulations. *Climate Dynamics*, *54*(5–6), 2697–2712. https://doi.org/10.1007/s00382-020-05137-1

Silva Dias, P. L., Turcq, B., Silva Dias, M. A. F., Braconnot, P., & Jorgetti, T. (2009). Mid-Holocene Climate of Tropical South America: A Model-Data Approach (pp. 259–281). https://doi.org/10.1007/978-90-481-2672-9_11

Skonieczny, C., Paillou, P., Bory, A., Bayon, G., Biscara, L., Crosta, X., et al. (2015). African humid periods triggered the reactivation of a large river system in Western Sahara. *Nature Communications*, *6*, 6–11. https://doi.org/10.1038/ncomms9751

Sultan, B., & Janicot, S. (2003). The West African monsoon dynamics. Part II: The "preonset" and "onset" of the summer monsoon. *Journal of Climate*, *16*(21), 3407–3427. https://doi.org/10.1175/1520-0442(2003)016<3407:TWAMDP>2.0.CO;2

Sun, W., Wang, B., Zhang, Q., Pausata, F. S. R., Chen, D., Lu, G., et al. (2019). Northern Hemisphere Land Monsoon Precipitation Increased by the Green Sahara During Middle Holocene. *Geophysical Research Letters*, *46*(16), 9870–9879. https://doi.org/10.1029/2019GL082116

Swann, A. L., Fung, I. Y., Levis, S., Bonan, G. B., & Doney, S. C. (2010). Changes in arctic vegetation amplify high-latitude warming through the greenhouse effect. *Proceedings of the National Academy of Sciences of the United States of America*, *107*(4), 1295–1300. https://doi.org/10.1073/pnas.0913846107

Swann, A. L. S., Fung, I. Y., & Chiang, J. C. H. (2012). Mid-latitude afforestation shifts general circulation and tropical precipitation. *Proceedings of the National Academy of Sciences of the United States of America*, *109*(3), 712–716. https://doi.org/10.1073/pnas.1116706108

Swann, A. L. S., Fung, I. Y., Liu, Y., & Chiang, J. C. H. (2014). Remote vegetation feedbacks and the mid-Holocene green Sahara. *Journal of Climate*, *27*(13), 4857–4870. https://doi.org/10.1175/JCLI-D-13-00690.1

Tabel, J., Khater, C., Rhoujjati, A., Dezileau, L., Bouimetarhan, I., Carre, M., et al. (2016). Environmental changes over the past 25 000 years in the southern Middle Atlas, Morocco. *Journal of Quaternary Science*, *31*(2), 93–102. https://doi.org/10.1002/JQS.2841

Tabor, C., Otto-Bliesner, B., & Liu, Z. (2020a). Speleothems of South American and Asian Monsoons Influenced by a Green Sahara. *Geophysical Research Letters*, *47*(22), 1–11. https://doi.org/10.1029/2020GL089695

Tabor, C., Otto-Bliesner, B., & Liu, Z. (2020b). Speleothems of South American and Asian Monsoons Influenced by a Green Sahara. *Geophysical Research Letters*, *47*(22), 1–11. https://doi.org/10.1029/2020GL089695

Taylor, K. E., Stouffer, R. J., & Meehl, G. A. (2012). An overview of CMIP5 and the experiment design. *Bulletin of the American Meteorological Society*, *93*(4), 485–498. https://doi.org/10.1175/BAMS-D-11-00094.1

Thompson, A. J., Skinner, C. B., Poulsen, C. J., & Zhu, J. (2019). Modulation of Mid-Holocene African Rainfall by Dust Aerosol Direct and Indirect Effects. *Geophysical Research Letters*, *46*(7), 3917–3926. https://doi.org/10.1029/2018GL081225

Thompson, A. J., Tabor, C. R., Poulsen, C. J., & Skinner, C. B. (2021). Water isotopic constraints on the enhancement of the mid-Holocene West African monsoon. *Earth and Planetary Science Letters*, *554*. https://doi.org/10.1016/j.epsl.2020.116677

Thompson, A. J., Zhu, J., Poulsen, C. J., Tierney, J. E., & Skinner, C. B. (2022). Northern Hemisphere vegetation change drives a Holocene thermal maximum. *Science Advances*, *8*(15), eabj6535. https://doi.org/10.1126/sciadv.abj6535

Thorncroft, C. D., Nguyen, H., Zhang, C., & Peyrille, P. (2011). Annual cycle of the West African monsoon: Regional circulations and associated water vapour transport. *Quarterly Journal of the Royal Meteorological Society*, *137*(654), 129–147. https://doi.org/10.1002/qj.728

Tierney, J. E., Lewis, S. C., Cook, B. I., LeGrande, A. N., & Schmidt, G. A. (2011). Model, proxy and isotopic perspectives on the East African Humid Period. *Earth and Planetary Science Letters*, *307*(1–2), 103–112. https://doi.org/10.1016/j.epsl.2011.04.038

Tierney, J. E., deMenocal, P. B., & Zander, P. D. (2017). A climatic context for the out-of-Africa migration. *Geology*, *45*(11), 1023–1026. https://doi.org/10.1130/G39457.1

Tierney, J. E., Pausata, F. S. R., & De Menocal, P. B. (2017). Rainfall regimes of the Green Sahara. *Science Advances*, *3*(1), 1–9. https://doi.org/10.1126/sciadv.1601503

Tiwari, S., Ramos, R. D., Pausata, F. S. R., LeGrande, A. N., Griffiths, M. L., Beltrami, H., et al. (2023, June 28). On the Remote Impacts of Mid-Holocene Saharan Vegetation on South American Hydroclimate: A Modeling Intercomparison. *Geophysical Research Letters*. John Wiley and Sons Inc. https://doi.org/10.1029/2022GL101974

Ullman, D. J., Carlson, A. E., Hostetler, S. W., Clark, P. U., Cuzzone, J., Milne, G. A., et al. (2016). Final Laurentide ice-sheet deglaciation and Holocene climate-sea level change. *Quaternary Science Reviews*, *152*, 49–59. https://doi.org/10.1016/j.quascirev.2016.09.014

Utida, G., Cruz, F. W., Santos, R. V., Sawakuchi, A. O., Wang, H., Pessenda, L. C. R., et al. (2020). Climate changes in Northeastern Brazil from deglacial to Meghalayan periods and related environmental impacts. *Quaternary Science Reviews*, *250*. https://doi.org/10.1016/j.quascirev.2020.106655

Valdes, P. J. (2000). South American palaeoclimate model simulations: How reliable are the models? *Journal of Quaternary Science*, *15*(4), 357–368. https://doi.org/10.1002/1099-1417(200005)15:4<357::AID-JQS547>3.0.CO;2-8

Valdes, P. J., Armstrong, E., Badger, M. P. S., Bradshaw, C. D., Bragg, F., Crucifix, M., et al. (2017). The BRIDGE HadCM3 family of climate models: HadCM3@Bristol v1.0. *Geoscientific Model Development*, *10*(10), 3715–3743. https://doi.org/10.5194/gmd-10-3715-2017

De Vernal, A., Hillaire-Marcel, C., Rochon, A., Fréchette, B., Henry, M., Solignac, S., & Bonnet, S. (2013). Dinocyst-based reconstructions of sea ice cover concentration during the Holocene in the Arctic Ocean, the northern North Atlantic Ocean and its adjacent seas. *Quaternary Science Reviews*, *79*, 111–121. https://doi.org/10.1016/j.quascirev.2013.07.006

De Vernal, A., Hillaire-Marcel, C., Le Duc, C., Roberge, P., Brice, C., Matthiessen, J., et al. (2020). Natural variability of the Arctic Ocean sea ice during the present interglacial. *Proceedings of the National Academy of Sciences of the United States of America*, *117*(42), 26069–26075. https://doi.org/10.1073/pnas.2008996117

Wang, X., Edwards, R. L., Auler, A. S., Cheng, H., Kong, X., Wang, Y., et al. (2017). Hydroclimate changes across the Amazon lowlands over the past 45,000 years. *Nature*, *541*(7636), 204–207. https://doi.org/10.1038/nature20787

Watrin, J., Lézine, A. M., Hély, C., Cour, P., Ballouche, A., Duzer, D., et al. (2009). Plant migration and plant communities at the time of the "green Sahara." *Comptes Rendus - Geoscience*, *341*(8–9), 656–670. https://doi.org/10.1016/j.crte.2009.06.007

White, F. (1986). *La végétation de l'Afrique*.

Wittenberg, A. T. (2009). Are historical records sufficient to constrain ENSO simulations? *Geophysical Research Letters*, *36*(12). https://doi.org/10.1029/2009GL038710

Wittenberg, A. T., Rosati, A., Delworth, T. L., Vecchi, G. A., & Zeng, F. (2014). ENSO modulation: Is it decadally predictable? *Journal of Climate*, *27*(7), 2667–2681. https://doi.org/10.1175/JCLI-D-13-00577.1

Zhang, M., Liu, Y., Zhang, J., & Wen, Q. (2021). AMOC and climate responses to dust reduction and greening of the sahara during the mid-holocene. *Journal of Climate*, *34*(12), 4893–4912. https://doi.org/10.1175/JCLI-D-20-0628.1

Zhao, Y., Braconnot, P., Marti, O., Harrison, S. P., Hewitt, C., Kitoh, A., et al. (2005). A multi-model analysis of the role of the ocean on the African and Indian monsoon during the mid-Holocene. *Climate Dynamics*, *25*(7–8), 777–800. https://doi.org/10.1007/S00382-005-0075-7/METRICS

Zheng, W., Braconnot, P., Guilyardi, E., Merkel, U., & Yu, Y. (2008). ENSO at 6ka and 21ka from ocean-atmosphere coupled model simulations. *Climate Dynamics*, *30*(7–8), 745–762. https://doi.org/10.1007/s00382-007-0320-3

Zhu, J., Otto-Bliesner, B. L., Brady, E. C., Gettelman, A., Bacmeister, J. T., Neale, R. B., et al. (2022). LGM Paleoclimate Constraints Inform Cloud Parameterizations and Equilibrium Climate Sensitivity in CESM2. *Journal of Advances in Modeling Earth Systems*, *14*(4), e2021MS002776. https://doi.org/10.1029/2021MS002776